Exploring the environmental factors controlling iceberg season severity along the east coast of Canada

by Madhurima Chakraborty

A thesis submitted to the Faculty of Graduate Studies of the University of Manitoba in partial fulfillment of the requirements of the degree of

Master of Science

Department of Environment and Geography

University of Manitoba, Winnipeg

© Madhurima Chakraborty, Manitoba, Canada, 2025

Abstract

Mass loss from Greenland's marine-terminating glaciers occurs largely through solid discharge, that is, the calving of icebergs. Some of these icebergs reach the east coast of Canada and pose navigation hazards to offshore industries, especially during the peak iceberg season (February to August). Increasing marine activity heightens the need for accurate predictions of iceberg occurrence off the east Canadian coast. However, an abrupt increase in the iceberg count variability in recent decades has reduced the predictability of the season. Therefore, a thorough understanding of processes influencing the iceberg severity is essential to understand which process(es) dominate. Studies suggest multiple factors such as oceanic conditions along the Labrador region, upstream environment, as well as calving rates. However, the most significant governing factor is still a matter of debate. Moreover, scarcity of observational data outside the International Ice Patrol-monitored region obscures understanding of the roles played by potential upstream governing factors. Therefore, an improved model representation of the connections between the processes and iceberg severity is imperative. With this motivation, we evaluate NEMO-ICB (v3.6) outputs against observations and test the model's sensitivity to atmospheric forcing and simulation period. Majority of the seasons with higher iceberg severity found to coincide with concentrated sea ice and colder Labrador shelf waters. The model outputs identified another driver affecting the iceberg counts in the shipping lanes which has not yet been considered in the literature: Baffin Bay gyre strength, which is interlinked to the sea surface height gradient. The energy of Baffin Bay circulation controls the transport of the icebergs out of Baffin Bay into the northern Labrador coast, and in turn the downstream iceberg severity. The temporal evolution of the correlations among the iceberg presence and environmental factors suggests that the importance of the major drivers of the iceberg season severity varies over time with the environment's mean state. Despite potential biases from model simplifications, with the novel finding this study narrows down the environmental factors influencing iceberg occurrence along eastern Canada and improves understanding of the processes driving seasonal variability.

Dedicated

...to Baba

Acknowledgments

I am in short with words to express my gratitude to my supervisor and the primary member of my advisory committee Dr. Juliana M. Marson for her continuous support and rigorous guidance. I could not have completed this work without the constructive feedback and inputs I received from my respected committee members Dr. Paul G. Myers, and Dr. Jens Ehn.

I acknowledge the financial support of Natural Sciences and Engineering Research Council (NSERC). I appreciate the faculty of graduate studies of University of Manitoba for the award University of Manitoba Graduate Fellowship (UMGF), the International Graduate Student Entrance Scholarship (IGSES), the research completion scholarship, the Baryla award, and also for the travel grants. I am grateful to University of Alberta for covering part of my conference travel expenses. Last, but not the least, I am deeply indebted to the Clayton H. Riddell Faculty of Environment, Earth, and Resources for the D.G. and V.E. Memorial Barber Fellowship in Arctic Research.

I would take this opportunity to thank the NEMO group and DRAKKAR project for making the model packages available, and to the Digital Research Alliance of Canada for providing the high performing computational environment.

I am much obliged to the administrative and technical stuffs, and the librarians for helping me through the technical minutia all along. Celia Mellinger, Grace O'Hanlon, and Jason Northage hold special place in my heart.

I thank my peers, colleagues, and cohort members for their constant encouragement and support, especially during the hardest times.

Finally my deepest gratitude goes to my family, and my friend Keerthna Hariprakash for being my strongest backbone throughout this journey.

Contents

1 Introduction **19**
- 1.1 Background . . . 19
  - 1.1.1 Importance of icebergs . . . 19
  - 1.1.2 Greenland icebergs and their trajectories . . . 21
  - 1.1.3 Iceberg season in east coast of Canada . . . 23
  - 1.1.4 Prior studies about factors controlling I48N variability . . . 27
  - 1.1.5 Model representation of icebergs . . . 32
- 1.2 Problem . . . 33
- 1.3 Research goals . . . 33
- 1.4 Relevance . . . 34
- 1.5 Thesis structure . . . 35

2 Data and methodology **36**
- 2.1 Observational data . . . 36
- 2.2 Model outputs . . . 44
  - 2.2.1 Model description . . . 44
  - 2.2.2 Configuration . . . 50
- 2.3 Methodology . . . 53

3 Results and discussion **57**
- 3.1 Observational data analyses . . . 57
  - 3.1.1 Characterizing the observed iceberg season . . . 57
  - 3.1.2 Characterizing relationships between I48N and environmental conditions . . . 62
  - 3.1.3 Section synopsis . . . 80
- 3.2 Model output evaluation . . . 80
  - 3.2.1 Characteristics of modelled iceberg season . . . 81
  - 3.2.2 Seasonal distribution varying with sizes of the icebergs . . . 85

3.2.3 Evaluation of the relationships between I48N and environmental conditions . . . 91
3.2.4 Section synopsis . . . 97
3.3 I48N sensitivity to atmospheric forcing and initial iceberg field . . . 97
3.3.1 Model's response to initial iceberg field . . . 98
3.3.2 Characteristics of the modelled iceberg season . . . 98
3.3.3 Seasonal distribution varying with sizes of the icebergs . . . 104
3.3.4 Differences in environmental conditions . . . 104
3.3.5 Section synopsis . . . 132

4 Summary and conclusion **134**
4.1 Findings . . . 134
4.2 Limitations and biases . . . 137
4.3 Conclusion . . . 138
4.4 Supplementary figures . . . 147

List of Figures

1.1 Mean elevation rates for 2010-2017 for the Greenland Ice Sheets, derived from CryoSat-2 radar altimetry Regions of mass loss, concentrated around the southeast and western margins of the GrIS are shown in red. The solid black polygons show where CryoSat-2 switches between different modes, which introduced some artifacts in dh/dt near the boundary between them. JI = Jakobshavn Isbrae. Source of the picture: [Bamber et al., 2018a] 20
1.2 Map showing the main currents affecting Greenland icebergs drift: Transpolar Drift (TPD), East Greenland Current (EGC), East Greenland Coastal Current (EGCC), Irminger Current (IC), West Greenland Current (WGC), Baffin Island Current (BIC), and Labrador Current (LC). The orange circles represent average calving rates (2002–2010), in Gt/year, seeded to the iceberg model on the ANHA4 grid. Source of the picture: [Marson et al., 2018] 22
1.3 Domain of the study (15° West to 80° West, 45° North to 83° North). NF: Newfoundland, and BI: Baffin Island. The red curved line, magenta delineation, blue straight line, and maroon dashed line respectively stand for 48° North latitude line that joins the tip of Flemish cap, and St. John's, the contour of 550 meters depth, approximate position of Davis Strait, and approximate position of the cross-section where the sea surface height across Baffin Bay was computed. 24
1.4 The geographical distribution of the ship-iceberg collisions. 1 All waters, 2 North Atlantic, 3 Grand Banks, 4 Gulf of St. Lawrence and South Newfoundland Waters, 5 Strait of Belle Isle and Approaches, 6 Labrador Sea and Davis Strait, 7 Hudson Strait, 8 South Greenland Waters, 9 Baffin Bay Area, 10 Greenland Sea, 11 Alaskan Waters. Figure source: [Hill, 2005] 25

1.5 Iceberg counts (1963-1991) as function of the 15th April ice extent off South Labrador and Newfoundland, and linear regression lines in both the low and high ice extent regions and the boundaries of the high, low, and intermediate iceberg count categories. Source: [Marko et al., 1994]. 27
1.6 Reconnaissance region monitored by International Ice Patrol with collaboration with Canadian Ice Service. International Ice Patrol (IIP) approximate area of responsibility (AOR, white outlined area) around the Grand Banks of Newfoundland, Canada, in the North Atlantic Ocean, where icebergs threaten shipping lanes during the iceberg season. a. The median sea ice extent in September (at its yearly minimum, cyan dotted line) and b. March (at its yearly maximum, cyan solid line) for 1981 to 2010. c. The median mid-January (dotted magenta line), mid-May (dashed magenta line), and early-September (solid magenta line) iceberg limits for 1991 to 2020; prior to about 2010, IIP did not systematically monitor icebergs north of 52°N. d. 48°N (red dotted line); IIP considers this latitude as that south of which icebergs pose a significant threat to the shipping lanes, and records the daily, monthly, and yearly estimated number of icebergs which drift south of it. e. An example transatlantic shipping route (yellow dashed line) along a rhumb line between Southampton, United Kingdom (UK) and New York City, US. Source of figure: IIP report 2023. 31

2.1 Source of figure: International Ice Patrol annual report, 2018. . . . 38
2.2 A diagram of middle 50% method, where σ = standard deviation of the dataset. The dataset is scaled to a range from 0 to 100. 39
2.3 Transformation metrics used by International Ice Patrol to define the upper and the lower limits of severity classes of iceberg seasons during different reconnaissance periods. Source of figure: IIP annual report, 2018. 40
2.4 The iceberg counts normalized to the range of 0 to 100 for each reconnaissance period of IIP. 41
2.5 The six sectors of Greenland solid discharge defined for the following analyses. 43
2.6 Model representation of particles with icebergs of different size classes. (schematic courtesy: Dr. Juliana M. Marson) 47

2.7 (a): Tripolar grid of the model, (b): The locations of the variables diagnosed in the three dimensional Arakawa C grid of the model. . 50
2.8 Iceberg seasons averaged over six decades: (a) 1960-1969, (b) 1970-1979, (c) 1980-1989, (d) 1990-1999, (e) 2000-2009, and (f) 2010-2019. 52
2.9 Schematic of methodology: Median travel times taken by the icebergs to reach 48° North from calving sectors (2.5) were computed from the model outputs of **CFA**. Years with Light, Moderate, Heavy, and Extreme iceberg seasons are color-coded in green, yellow, orange, and red. Three randomly chosen consecutive years 1997, 1998, and 1999 were moderate, heavy, and light respectively (and 2000 was another heavy year). The median travel time of the icebergs from Northwest sector to 48° North is 469 days (approximately 15 months). So, the calving that happened in January, 1997 from Northwest sector contributes to the I48N in April, 1998. SW, NW, SE, and NE are sectors Southwest, Northwest, Southeast, and Northeast respectively. 55

3.1 The seasonality of iceberg counts observed by IIP to cross 48° N, averaged over the whole period (1900 to 2021) of IIP observation. . 58
3.2 The yearly total iceberg counts observed by IIP to cross 48° N in an iceberg year. The red curly bracket points out the time period when the interannual variability increased. 12 lightly (with a standard deviation of approximately 93.10 icebergs), 15 moderately (with a standard deviation of approximately 280.55 icebergs), 4 heavily (with a standard deviation of approximately 140.07 icebergs), and 8 extremely (with a standard deviation of approximately 290.03 icebergs) severe years were observed for the current reconnaissance period (1983 to date). Out of 38 years, 15 fell in the middle 50% of the I48N distribution, while 12 years belonged the range below that, 4 belonged to the range of 10% above it, and finally 8 years fell into the range above 85% of the distribution. (For middle 50% method, refer to explanation in chapter 2, and figure 2.2). 59

3.3 The monthly I48N distribution across different severity classes during the three IIP reconnaissance periods. The pink, purple, dark blue, and dark green lines indicate the monthly average of iceberg counts south of 48° N over the light, moderate, heavy, and extreme iceberg severity years of the corresponding periods. The shaded areas with same colors represent the monthly ranges of the iceberg counts (i.e. the difference between the highest count of icebergs and the lowest count of icebergs in each month). 60
3.4 The observed iceberg count crossing 48° N latitude line is shown for (a) light, (b) moderate, (c) heavy, and (d) extreme iceberg seasons on the east coast of Canada. Each color in a subplot stands for a particular year that belongs to the corresponding severity class. There were 12 lightly (with a standard deviation of approximately 93.10 icebergs), 15 moderately (with a standard deviation of approximately 280.55 icebergs), 4 heavily (with a standard deviation of approximately 140.07 icebergs), and 8 extremely (with a standard deviation of approximately 290.03 icebergs) severe years observed for the current reconnaissance period until 2021. That is out of 38 years, 15 fell in the middle 50% of the I48N distribution, while 12 years belonged the range below that, 4 belonged to the 10% above it, and finally 8 years fell into the range above 85% of the distribution. 61
3.5 Anomaly of yearly (October to September) total number of icebergs crossing 48° N (blue bar) with (a) the anomaly in SST (in °C, red line), and (b) the anomaly in temperature (in °C, red line) averaged over the upper 100 meters of ocean over the Labrador shelf mask (region shown in figure 1.3). 63
3.6 Observed spring depth-averaged (0-100 meters) ocean temperature anomaly over the Labrador shelf mask across different iceberg seasons. Headers Light, Moderate, Heavy, and Extreme show the average difference between depth-averaged spring temperature over light, moderate, heavy, and extreme iceberg years respectively and mean spring (April to June) temperature, averaged over the years 1994 to 2021. 65
3.7 Anomaly of yearly (October to September) total number of icebergs crossing 48° N, averaged over the time period 1995 to 2021 (blue bar) with the anomaly in area over Labrador shelf mask covered with sea ice during the winter months (January to March) in the years 1995 to 2021). 66

3.8 Observed winter sea ice concentration anomaly over Labrador shelf mask across severity classes. Light, Moderate, Heavy, and Extreme show the anomaly of sea ice concentration ($\geq 15\%$) over light, moderate, heavy, and extreme iceberg years, respectively, with respect to the average (1995-2021) sea ice concentration from January to March sea ice concentration, averaged over the years 1995 to 2021. . 67
3.9 The timeseries of the observed yearly total iceberg counts (blue bars) with the observed total area of Baffin Bay covered with high concentration sea ice ($\geq 90\%$) during the winter months (January to March). 69
3.10 The observed winter sea ice concentration anomalies (computed from averaged winter high concentration sea ice, i.e. $\geq 90\%$) is shown for (a) light, (b) moderate, (c) heavy, and (d) extreme iceberg seasons on the East Canadian coast. 71
3.11 Observed anomaly of yearly (October to September) total number of icebergs crossing 48° N, averaged over the time period 1900 to 2021 (blue bar) with the anomaly in solid discharge (in kg/year, red line) from (a) the northwest and (b) the north sectors of Greenland. 73
3.12 The statistical distribution of yearly total solid discharges from six calving sectors (refer to figure 2.5) of Greenland. The boxplots distribution of solid discharge from the sectors Southeast, Northeast, North, Northwest, Central West, and Southwest are shown in the subfigures left top row, middle top row, right top row, left bottom row, middle bottom row, and right bottom row respectively 225, 727, 615, 469, 600, and 216 days prior to the icebergs seasons categorized as light (first boxplot), moderate (second boxplot), heavy (third boxplot), and extreme (fourth boxplot). 75
3.13 The observed time evolution of the correlations between the environmental factors and I48N for Labrador shelf winter SST (sstWinterTS), Labrador shelf spring SST (sstSpringTS), 100 m depth averaged spring ocean temperature over Labrador shelf (T100mSpringTS), 100 m depth averaged winter ocean temperature over Labrador shelf (T100mWinterTS), winter sea ice area over Labrador shelf (LSsiaWinter), and Baffin Bay high concentration winter sea ice area (siaWinterTS). 77

3.14 Heat map showing the observed Pearson correlation values (along with p-values) between the environmental factors and I48N for Labrador shelf winter SST (sstWinterTS), Labrador shelf spring SST (sstSpringTS), 100 m depth averaged spring ocean temperature over Labrador shelf (T100mSpringTS), 100 m depth averaged winter ocean temperature over Labrador shelf (T100mWinterTS), winter sea ice area over Labrador shelf (LSsiaWinter), and Baffin Bay high concentration winter sea ice area (siaWinterTS). 78
3.15 The modelled (CFA) average seasonality of I48N averaged over the period (2004 to 2017) of the simulation with CGRF-forced atmosphere (**CFA**). 81
3.16 The modelled (CFA) yearly total **iceberg** counts crossing 48° N in an IIP-defined iceberg year. 82
3.17 The modelled (CFA) yearly total **particle** count crossing 48° N in an IIP-defined iceberg year. 82
3.18 The modelled (CFA) monthly iceberg counts distribution across different severity classes. 84
3.19 Average (2003-to-2017) seasonality of (a) icebergs from large (red), medium (orange) and small (yellow) size classes, (b) particles from large (red), medium (orange) and small (yellow) size classes. 86
3.20 Observed icebergs (blue bars) with modelled (CFA) particles from all size classes (orange bars). 87
3.21 The six latitude lines along the Labrador shelf, used to calculate the gradual reduction of the iceberg flux that enters the Labrador current. From the darkest to the lightest line the latitudes are from north to south: 58° N (darkest lines), 56° N, 54° N, 52° N, 50° N, and 48° N (lightest line). 88
3.22 Seasonality of count of (a) large size-class, (b) medium size-class, and (c) small size-class particles reaching 58° N (darkest lines), 56° N, 54° N, 52° N, 50° N, and 48° N (lightest line) latitude in the simulation CFA. 89
3.23 Anomaly of yearly (October to September) total number of icebergs crossing 48° N, averaged over the period of simulation (blue bar) with (a) the anomaly in SST (in °Celsius, red line), and (b) the anomaly in temperature (in °Celsius, red line) averaged over the upper 100 meters of ocean over Labrador shelf mask in the simulation CFA. 90

3.24 Anomaly of yearly (October to September) total number of icebergs crossing 48° N, averaged over the period of simulation (blue bar) with the anomaly in area over Labrador shelf covered with sea ice during the winter months (January to March) in the years 2003 to 2017) in the simulation CFA. 91
3.25 Spatial distribution of modelled (CFA) depth-integrated temperature anomaly (in °Celsius) on the Labrador shelf during the spring months (April to June) across the severity classes. In CFA, there was no heavy iceberg season, so, the third figure (CFA - Heavy (Spring) does not have any data. 92
3.26 Spatial distribution of modelled (CFA) sea ice concentration anomaly on the Labrador shelf over the winter months (January to March) across the severity classes. 93
3.27 Modelled (CFA) yearly total iceberg count (blue bar) and the area (in km^2) of Baffin Bay covered with sea ice with high concentration ($\geq 90\%$) in the winter months (January to March) in the simulation CFA. 95
3.28 Spatial distribution of modelled (CFA) sea ice with high concentration ($\geq 90\%$) across the severity classes. 96
3.29 The annual total iceberg mass in the ocean (expressed in kg/year) for the whole period of simulation in JFA (upper panel), and in CFA (lower panel). 99
3.30 Monthly average number of IIP-observed iceberg (blue bars) with modelled average (a) iceberg count (orange bars) at 48°N, in the simulation JFA. 100
3.31 Monthly average number of IIP-observed particle (orange bars) at 48°N, in the simulation JFA. 101
3.32 The modelled (JFA) yearly total iceberg counts for the years 2003 to 2017. 102
3.33 The modelled (JFA) yearly total particle counts for the years 2003 to 2017. There is only one extreme iceberg year in JFA, so only a single line representing seasonality of extreme years in the figure. . . 102
3.34 The modelled (JFA) seasonality averaged over the period (1994 to 2017). 103
3.35 Seasonality of count of (a) large size-class, (b) medium size-class, and (c) small size-class particles reaching 58° N (darkest lines), 56° N, 54° N, 52° N, 50° N, and 48° N (lightest line) latitude in the simulation JFA. 105

3.36 The SST in CFA subtracted from the SST in JFA averaged over (a) the winter months, (b) the spring months, (c) the summer months, and (d) the autumn months of the overlapping period of integration (2002 to 2017) over the whole domain of interest. 106
3.37 Anomaly of yearly (October to September) total number of icebergs crossing 48° N, with respect to the averaged over the period of simulation (blue bar) with (a) the anomaly in SST (in °C, red line), and (b) the anomaly in temperature (in °C, red line) averaged over the upper 100 meters of ocean over the Labrador shelf mask in the JFA simulation. 107
3.38 The modelled (JFA) time evolution of the correlations between the environmental factors and I48N for Labrador shelf winter SST (sstWinterTS), Labrador shelf spring SST (sstSpringTS), 100 m depth averaged spring ocean temperature over Labrador shelf (T100mSpringTS), 100 m depth averaged winter ocean temperature over Labrador shelf (T100mWinterTS), Winter sea ice area over Labrador shelf (LSsiaWinter), and Baffin Bay high concentration Winter sea ice area (siaWinterTS). 108
3.39 Heat map showing the modelled (JFA) Pearson correlation values (along with p-values) between the environmental factors and I48N for Labrador shelf winter SST (sstWinterTS), Labrador shelf spring SST (sstSpringTS), 100 m depth averaged spring ocean temperature over Labrador shelf (T100mSpringTS), 100 m depth averaged winter ocean temperature over Labrador shelf (T100mWinterTS), Winter sea ice area over Labrador shelf (LSsiaWinter), and Baffin Bay high concentration Winter sea ice area (siaWinterTS). 109
3.40 Spatial distribution of modelled (JFA) depth-integrated temperature anomaly (in °C) over the Labrador shelf over the spring months (April to June) across the severity classes. 110
3.41 Anomaly of yearly (October to September) total number of icebergs crossing 48° N, with respect to average over the period of simulation (blue bar) with the anomaly of sea ice area (in km^2) over the Labrador shelf during the winter months (January to March) in the years 1994 to 2017 in the simulation JFA. 112
3.42 Spatial distribution of modelled (JFA) sea ice concentration anomaly on the Labrador shelf mask over the winter months (January to March) across the severity classes. 113

3.43 Table 4.2 shows the absolute numbers for different sized particles (column 2 to 4), for all particles (column 5) for the period 2002-2017. 114
3.44 Table 4.2 shows the percentage numbers for different sized particles (column 2 to 4), for all particles (column 5) for the period 2002-2017. 115
3.45 Total mass (in kg) of large, medium, and small icebergs crossing the six latitudes (i.e. 58°, 56°, 54°, 52°, 50°, and 48° north) along the Labrador shelf in JFA (red line), and CFA (blue line) simulations. . 117
3.46 Histograms of mass distribution of large (left column), medium (middle column), and small (right column) particles at 58° N in the JFA (top row) and in the CFA (bottom row) simulations respectively. The blue solid lines and the red dashed lines represent the mean, and the median of the corresponding data. SD = standard deviation is shown in the corresponding subplot. 117
3.47 The SST in CFA subtracted from the SST in JFA averaged over (a) the winter months, (b) the spring months, (c) the summer months, and (d) the autumn months of the overlapping period of integration (2002 to 2017) over Baffin Bay. 119
3.48 Modelled (JFA) yearly total iceberg count (blue bar) and the area (in km^2) of Baffin Bay covered with sea ice with high concentration ($\geq$ 90%) in the winter months (January to March) in the simulation JFA. 120
3.49 Spatial distribution of anomalies in the modelled (JFA) sea ice with high concentration ($\geq$ 90%) across the severity classes. 121
3.50 Differences in number of particles crossing every grid point of the domain between CFA and JFA from 2002 to 2017. 123
3.51 The eastward component of wind stress in CFA were subtracted from the eastward component of wind stress in JFA. Those differences averaged over winter, spring months,summer months, and autumn months of the year 2002 to 2017 are shown in (a), (b), (c), and (d) respectively over the whole domain of interest. 124
3.52 The logarithm (power of 10) of rate of iceberg melt in JFA (top row), and in CFA (bottom row) for the seasons Winter, Spring, Summer, and Autumn, averaged over the period 2004-2017. 126
3.53 The eastward wind component values in CFA subtracted from the zonal wind component value in JFA averaged over (a) the winter months, (b) the spring months, (c) the summer months, and (d) the autumn months of the overlapping period of integration (2002 to 2017) over the Baffin Bay. 127

3.54 Upper panel: Spatial distribution of sea surface height averaged over (a) winter, (b) spring, (c) summer, and (d) autumn months in the simulation JFA. Lower panel: Spatial distribution of winter sea surface height averaged over (e) winter, (f) spring, (g) summer, and (h) autumn months in the simulation CFA. 128
3.55 Seasonal average of SSH in JFA (in the upper panel), and in CFA (in the lower panel) along the dashed red line across Baffin Bay shown in the map 1.3. 129
3.56 The eddy kinetic energy in CFA subtracted from the eddy kinetic energy in JFA averaged over (a) the winter months, (b) the spring months, (c) the summer months, and (d) the autumn months of the common period of integration (2002 to 2017) over the Baffin Bay. . 130

4.1 Iceberg seasons averaged over six decades: (a) 1960-1969, (b) 1970-1979, (c) 1980-1989, (d) 1990-1999, (e) 2000-2009, and (f) 2010-2019. Each blue bar represents the number of icebergs in the corresponding month, averaged over the decade. For example on an average 52 icebergs reached 48° N in the month of May, during the years 1960-1969. 147
4.2 Trajectories of particles reaching 48° N, that calved from central West sector of Greenland in the month of February in the CFA simulation. Each color represents the path of a particular particle. . 148
4.3 Distribution of times (in days) taken by particles in CFA from different Greenland calving sectors to reach 48° North latitude. SD = standard deviation, and CV = covariance of the corresponding data. SE = Southeast, NE = Northeast, N = North, NW = Northwest, CW = Central West, and SW = Southwest as shown in the figure 2.5. 149
4.4 The modelled (CFA) time evolution of the correlations between the environmental factors and I48N for Labrador shelf winter SST (sstWinterTS), Labrador shelf spring SST (sstSpringTS), 100 m depth averaged spring ocean temperature over Labrador shelf (T100mSpringTS), 100 m depth averaged winter ocean temperature over Labrador shelf (T100mWinterTS), Winter sea ice area over Labrador shelf (LSsiaWinter), and Baffin Bay high concentration Winter sea ice area (siaWinterTS). 150

4.5 Heat map showing the modelled (JFA) Pearson correlation values (along with p-values) between the environmental factors and I48N for Labrador shelf winter SST (sstWinterTS), Labrador shelf spring SST (sstSpringTS), 100 m depth averaged spring ocean temperature over Labrador shelf (T100mSpringTS), 100 m depth averaged winter ocean temperature over Labrador shelf (T100mWinterTS), Winter sea ice area over Labrador shelf (LSsiaWinter), and Baffin Bay high concentration Winter sea ice area (siaWinterTS). 150
4.6 The spatial distribution of seasonal average of high concentration ($\geq$ 90%) sea ice in Baffin Bay in JFA (top row), and in CFA (bottom row), in Winter (first column), Spring (second column), Summer (third column), and Autumn (last column) months respectively. . . 151
4.7 Percentage of particles counts in (a) JFA, and (b) CFA simulation calved from the sectors of Greenland. SE = Southeast, NE = Northeast, N = North, NW = Northwest, CW = Central West, and SW = Southwest as shown in the figure 2.5. 16%, 1%, 13%, 39%, 25%, and 5% of I48N in the simulation JFA were originated from SE, NE, N, NW, CW, and SW sectors of Greenland respectively. 9%, 1%, 12%, 52%, 21%, and 4% of I48N in the simulation CFA were originated from SE, NE, N, NW, CW, and SW sectors of Greenland respectively. 152
4.8 Number of particles crossing each grid cell in the CFA simulation over the period 2002 to 2017. 153
4.9 Number of particles crossing each grid cell in the JFA simulation over the period 2002 to 2017. 154
4.10 Direction (shown with arrows) and magnitude (in m/s) of wind stress vectors over the domain of study in (a) JFA, and (b) CFA simulation. 155
4.11 Ocean meridional velocity (in m/s) across Davis Strait in CFA. Northward direction is positive (red). Ocean depth shown in the Y-axis, and longitude in X-axis. 156
4.12 Ocean meridional velocity (in m/s) across Davis Strait in JFA. Northward direction is positive (red). Ocean depth shown in the Y-axis, and longitude in X-axis. 157
4.13 Frequency distribution of (a) I48N observed by IIP for the years 1983-2021, (b) I48N in the simulation JFA, (c) I48N in the simulation CFA. 158

4.14 Origin of modelled icebergs in the years 2002 to 2015. The intensity of colors, at each grid point, indicates the percentage of particles that came from (a) north, (b) northeast, (c) southeast, (d) southwest, and (e) northwest. Figure source: [Marson et al., 2018] 159

List of Tables

2.1 Definition of severity classes of iceberg season. I48Nobs = observed value of I48N for that season, $\overline{I48N}$ = mean of the normalized observed I48N over the whole period of observation, σ_{I48N} = standard deviation of the normalized observed I48N over the whole period of observation 40
2.2 Definition of severity classes of iceberg season based on iceberg counts South of 48°N. 41
2.3 Iceberg size calving distribution in NEMO model. The mass scaling factor (column 5) is an integer that stands for the number of icebergs in one particle (refer to figure 2.6). Calving rates are distributed according to the fractions listed in the last column. source: [Martin and Adcroft, 2010] 2010. 46

3.1 Definition of severity classes for outputs of the simulations CFA (second column), and JFA (third column). 85

List of Acronyms

ANHA4: Arctic and Northern Hemispheric Atlantic, 1/4°
BIC: Baffin Island Current
CGRF: Canadian Meteorological Center's Global deterministic prediction system ReForecast
CIS: Canadian Ice Service
CMS: Copernicus Marine Service
EGC: East Greenland Current
GCM: General Circulation Model
GIC: Glaciers and Ice Cap
GrIS: Greenland Ice Sheet
I48N: Icebergs below 48° North
IC: Irminger Current
IIP: International Ice Patrol
JRA55-DO: Japanese 55-year Atmospheric Reanalysis
LAKI: Limit of All Known Ice
LC: Labrador Current
LIM: Louvian-la-Neuve Sea Ice Model
LOS: Length Of Season
LSST: Labrador Shelf Surface Temperature
MOC: Meridional Overturning Circulation
NAO: North Atlantic Oscillation
NAOI: North Atlantic Oscillation Index
NEMO: Nucleus for European Modelling of the Ocean
NEW: Newfoundland
NRC-PERD: National Research Council - Program of Energy Research and Development
NSIDC: National Snow and Ice Data Center
NSSI: Normalized Season Severity Index
SLR: Sea Level Rise
SMB: Surface Mass Balance
SSH: Sea Surface Height
SST: Sea Surface Temperature
USCG: U.S. Coast Guard
WGC: West Greenland Current

Chapter 1

Introduction

1.1 Background

Due to the recent warming of Arctic, mass loss from Greenland Ice Sheet (GrIS) through the outlets of tidewater glaciers has amplified four times since the beginning of this century [Straneo and Heimbach, 2013]. Figure 1.1 shows the spatial distribution of time rate of change in scaled height (dh/dt) of the marine terminating glaciers for Greenland. The mass loss is significant in the glaciers on the west coast of Greenland. More than half (almost 60%) of this mass loss takes place in the form of solid discharge [Bamber et al., 2018a], which is mainly comprised of icebergs calving.

1.1.1 Importance of icebergs

By International Ice Patrol's definition (Iceberg formation, IIP) icebergs are large pieces ($\geq$ 15 meters in length) of land ice floating in water, calved from marine terminating glaciers or ice shelves. While icebergs from Antarctic glacial terminus can be huge (some times even $\geq$ 3200 meters), most of the icebergs of Greenland origin have lengths between 15 meters to 350 meters, and can have different shapes and width:length ratios. The largest iceberg observed in the Northern hemisphere to date was approximately 12 km long at the time of sighting (Iceberg formation document, IIP), and was estimated to have calved with a length of about 22 km. Due to frictional interaction with surrounding warmer ocean water, the submerged portion of icebergs release meltwater from their bottom, and side walls [Bigg et al., 1997]. As land ice is formed from snowfall, icebergs contain freshwater, and hence distribute it along their paths in

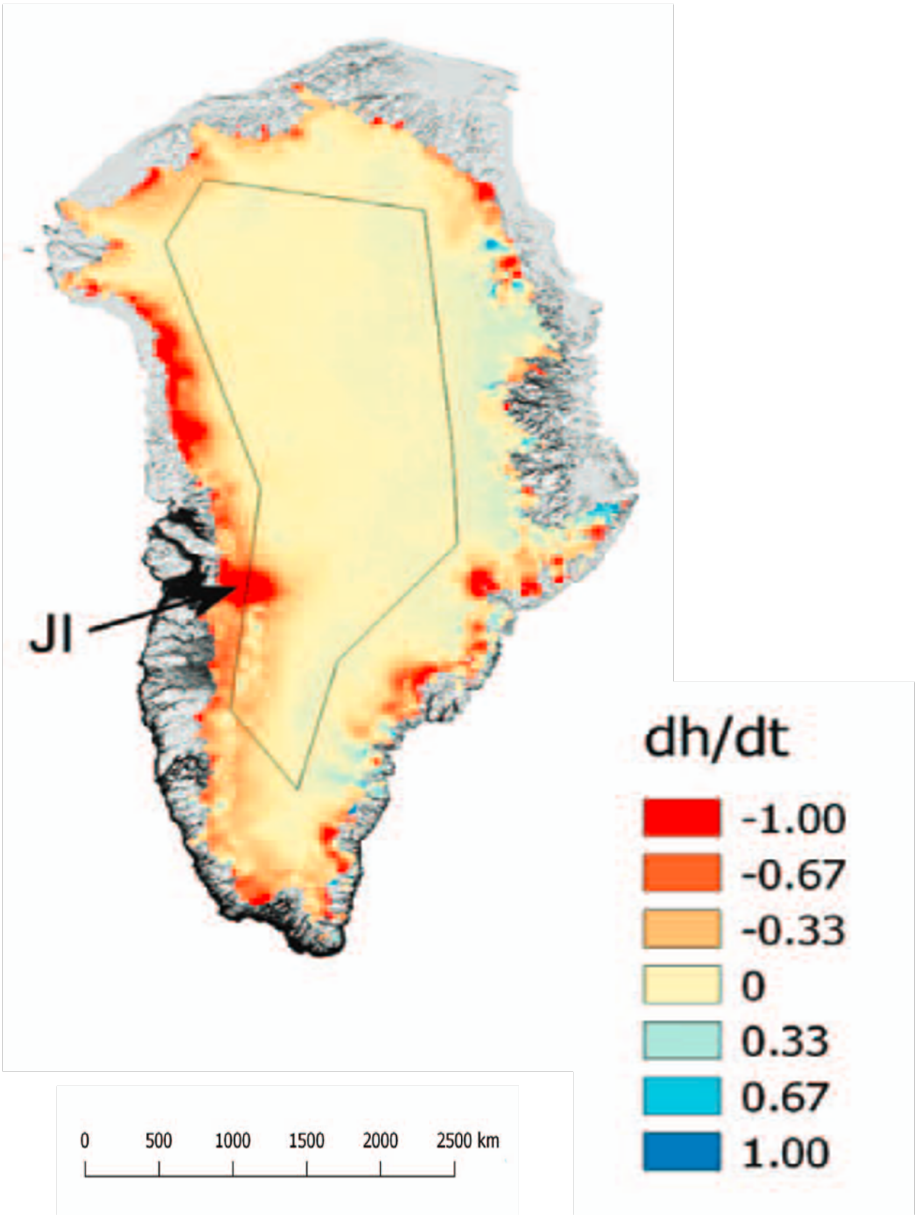

Figure 1.1: Mean elevation rates for 2010-2017 for the Greenland Ice Sheets, derived from CryoSat-2 radar altimetry Regions of mass loss, concentrated around the south-east and western margins of the GrIS are shown in red. The solid black polygons show where CryoSat-2 switches between different modes, which introduced some artifacts in dh/dt near the boundary between them. JI = Jakobshavn Isbrae. Source of the picture: [Bamber et al., 2018a]

the ocean (Martin and Adcroft, 2010). As this released meltwater is more buoyant than the surrounding saline ocean water, it plumes up to the ocean surface. This encourages vertical mixing between layers of stratified ocean [Stephenson et al., 2011]. When a lot of meltwater accumulates around the iceberg at the surface layer of the ocean, it stabilizes the water column by maintaining the stratification [Helly et al., 2011]. Icebergs may carry macro and micro-nutrients [Krause et al., 2024] into the open oceans, far away from their coastal origins. Icebergs bring iron, that enhances phytoplankton growth in areas where there is an iron limitation. This, in turn, alters the air-sea carbon flux [Cenedese and Straneo, 2023]. Therefore, for micronutrient-depleted oceans, which is found mostly in southern hemisphere, icebergs influences the carbon cycle through fertilizing the ocean water with bio-essential elements for the primary productivity. As the meltwater from icebergs is fresher that the saline ocean water around the iceberg, it is more buoyant compared to the ocean water in the vicinity of the icebergs. A model study in [Marson et al., 2021] showed that the meltwater released at the ocean surface from the iceberg can stabilize the water column by inhibiting the convective mixing. This can potentially impact the Meridional Overturning Circulation (MOC). All the above mentioned importance make icebergs a subject worth exploring.

1.1.2 Greenland icebergs and their trajectories

The orange solid circles in figure 1.2 (sourced from [Marson et al., 2018]) show the calving rates at major Greenland glaciers in Gigaton/year from [Bamber et al., 2018a]. Nearly 12,000 to 40,000 icebergs are calved from the tidewater glaciers around the Greenland coast [Tang et al., 2004] every year, up to 50% of which either melt or stay stuck in the fjords [Enderlin et al., 2016]. The icebergs that make their way to the ocean are driven by a combination of forces: the Coriolis force, the pressure gradient force generated by the ocean surface elevation, wave radiation force (a function of the roughness of the sea), and the drag forces from the media (air, ocean water, and sea ice) that the icebergs encounter on their paths [Smith, 1993]. In the ocean, the time rate of change of an iceberg's mass depends on the melt which is a function of the sea state, the temperature and the velocity differences between the iceberg and the surrounding ocean ([Martin and Adcroft, 2010]). Icebergs calved from aforementioned locations follow ocean currents, and a very small percentage (1% according to Iceberg formation, IIP) of them reach the shipping lanes off Canada's east coast. Figure 1.2 also shows the main ocean currents that icebergs

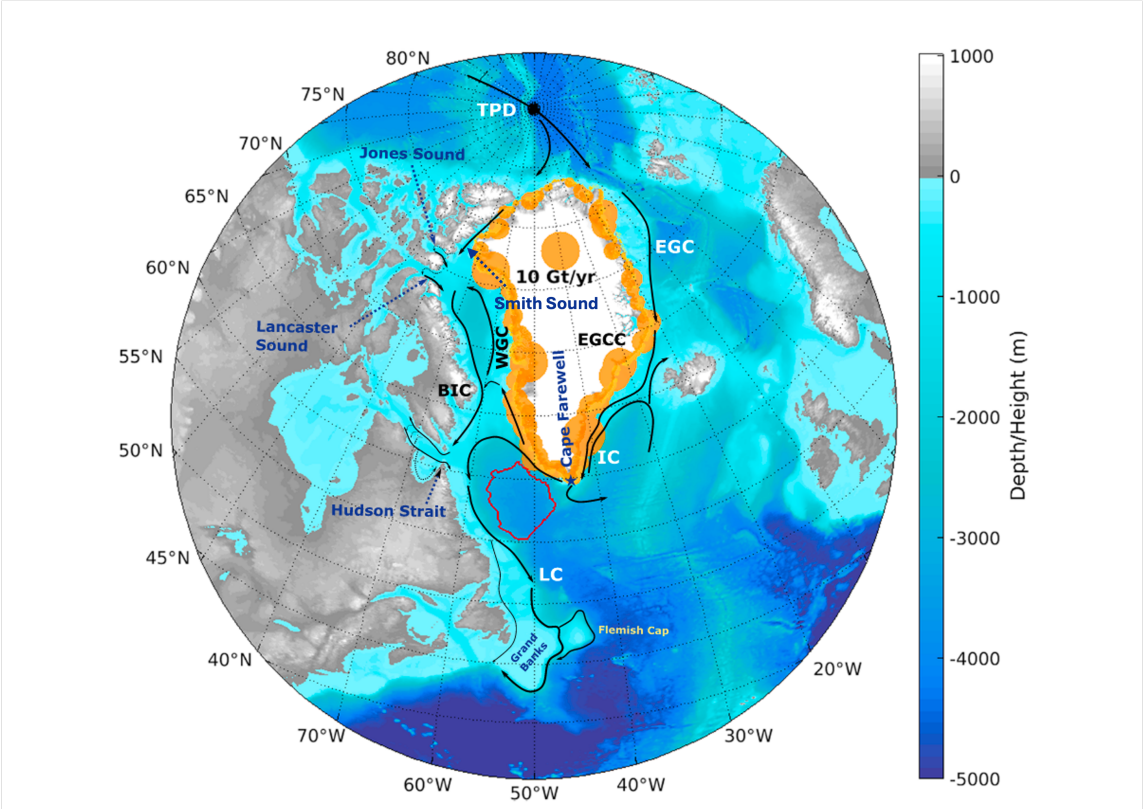

Figure 1.2: Map showing the main currents affecting Greenland icebergs drift: Transpolar Drift (TPD), East Greenland Current (EGC), East Greenland Coastal Current (EGCC), Irminger Current (IC), West Greenland Current (WGC), Baffin Island Current (BIC), and Labrador Current (LC). The orange circles represent average calving rates (2002–2010), in Gt/year, seeded to the iceberg model on the ANHA4 grid. Source of the picture: [Marson et al., 2018]

tend to follow (arrows). Icebergs from north and northeast Greenland drift south and then southwestward with the East Greenland Current (EGC). Along with some of them, icebergs calved from southeast Greenland follow the Irminger Current (IC) to the southern tip of Greenland. A branch of IC enters Baffin Bay as West Greenland Current (WGC). The WGC splits into two branches at Davis Strait (shown by the navy blue solid line in figure 1.3). One carries some of the icebergs of southwest Greenland origin across Davis Strait and southward in Labrador Sea. The other branch of WGC becomes the eastern boundary current and follow the west Greenland shelf break. Icebergs calved at the west Greenland shelf at central and northwest Greenland drift with this part of the northward current and travel to northern Baffin Bay. This current turns west and then southward near Nares Strait and become the Baffin Island Current (BIC). Most icebergs from west Greenland calving sites follow this western boundary current to move southward and then finally out of Baffin Bay. Near Hudson Strait, the BIC merges with the westward branch of the WGC, and the icebergs from both sides of Greenland start to follow Labrador Current (LC) and move southward along the east coast of Canada [Tang et al., 2004]. Icebergs travel along the shelf-break all the way to the very shallow region of Grand Banks (figure 1.2). The Newfoundland coast is popular for iceberg sighting, and so, was named as "iceberg alley".

1.1.3 Iceberg season in east coast of Canada

The 48° North latitude line (the red curved line in figure 1.3) approximately joins St. John's of Newfoundland and the northern tip of Flemish Cap, two geographical locations popular in the western part of North Atlantic for iceberg sighting and coastal fishery industries. This is an area where the busy shipping lanes of the Northern Atlantic converge, and therefore icebergs pose a collision threat. Since [Smith, E., 1993], this latitude was chosen to monitor the icebergs that reach this far south, where the iceberg count is used as an estimate of severity of the iceberg season [Trivers, G.,], [Rudnickas, Serumgard,] (refer to the link `https://doi.org/10.7265/z6e8-3027`). This parameter is commonly referred as **I48N** (that is **I**cebergs South of **48**° **N**orth). Figure 1.4 (sourced from [Hill, 2005]) shows the geographical locations of all the ship-iceberg collisions reported since 1600. The Grand Banks area (refer to figure 1.2) is the hotspot for the collisions. Besides, the petroleum industries' operations around this area often are hampered by the presence of the icebergs [Sudom et al., 2014]. this study further revealed that in most cases the vessels in this water encounter with

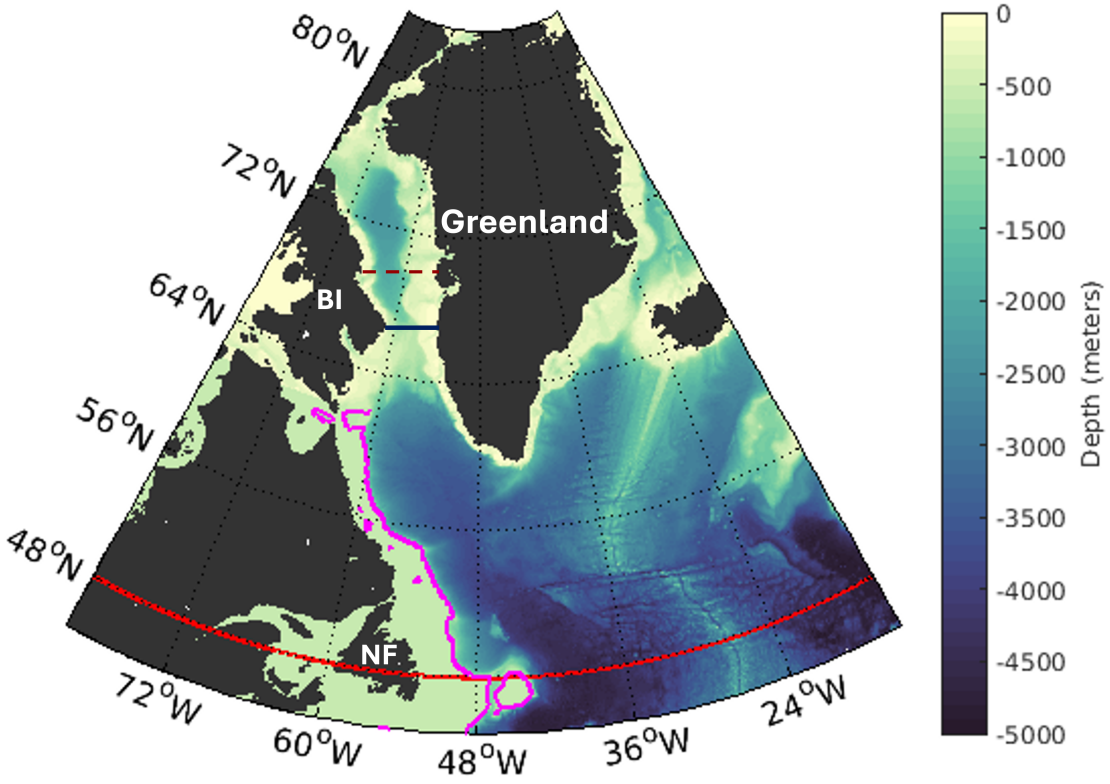

Figure 1.3: Domain of the study (15° West to 80° West, 45° North to 83° North). NF: Newfoundland, and BI: Baffin Island. The red curved line, magenta delineation, blue straight line, and maroon dashed line respectively stand for 48° North latitude line that joins the tip of Flemish cap, and St. John's, the contour of 550 meters depth, approximate position of Davis Strait, and approximate position of the cross-section where the sea surface height across Baffin Bay was computed.

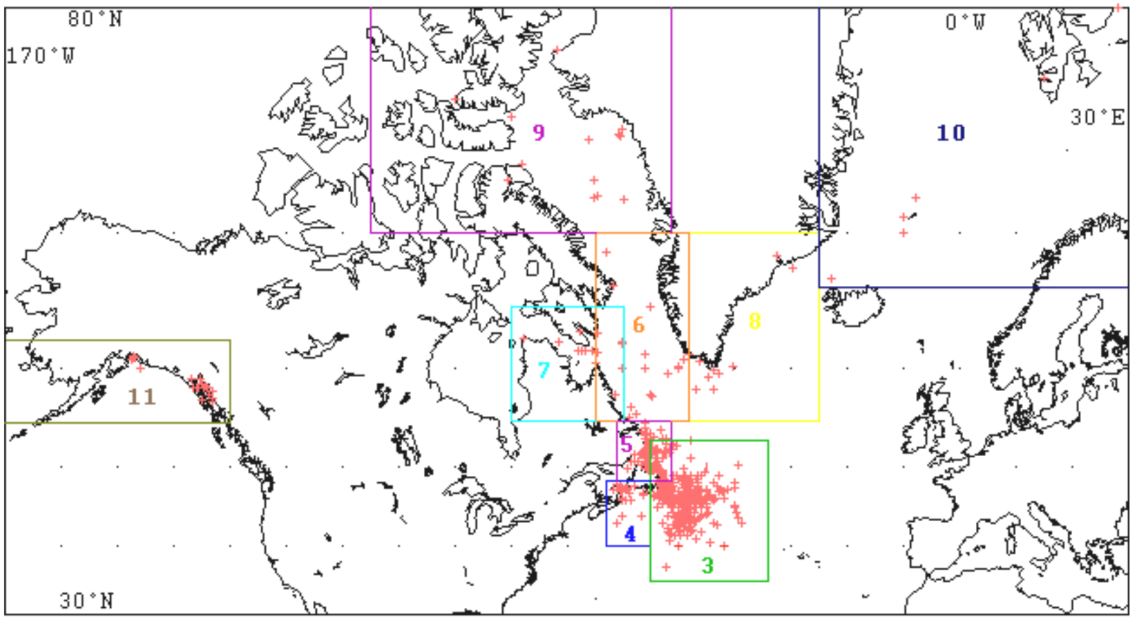

Figure 1.4: The geographical distribution of the ship-iceberg collisions. 1 All waters, 2 North Atlantic, 3 Grand Banks, 4 Gulf of St. Lawrence and South Newfoundland Waters, 5 Strait of Belle Isle and Approaches, 6 Labrador Sea and Davis Strait, 7 Hudson Strait, 8 South Greenland Waters, 9 Baffin Bay Area, 10 Greenland Sea, 11 Alaskan Waters. Figure source: [Hill, 2005]

small (15-60 meters) or medium (61-120 meters) icebegrs.
In the annual report of IIP [Rudnickas, Serumgard,] it was established that in recent decades the interannual variability of iceberg occurrences in the east coast of Canada increased abruptly. The yearly mean (averaged over the years 1950 to 2013) number of icebergs reaching 48° North latitude is 491 with a standard deviation of 567 [Sudom et al., 2014], that is, the range of uncertainty in the year-to-year variation in the severity of the iceberg season off the east coast of Canada is non-negligible. Moreover, in the backdrop of the recent unprecedented climate change, the Greenland Ice Sheet discharge has increased, giving rise to the likelihood of increased iceberg flux entering the east coast of Canada [Rignot et al., 2011]. At the same time, with an increasingly ice-free water, the offshore activities have peaked in recent times [Pizzolato et al., 2016]. The prediction for iceberg season off the east coast of Canada is thus desirable [Sudom et al., 2014]. Understanding the major environmental factors that govern the variation in the year-to-year variation is important if we want to predict it

using models. The primitive dynamic equations representing the major forces governing the drift of the icebergs in the ocean were established in [Smith, 1993]. [Marko et al., 1994] found a correlation between I48N and sea ice extent in Baffin Bay and the Labrador. using satellite data for sea ice, this study showed that spring sea ice condition in the Labrador Sea (represented by 15th April sea ice extent) shares a Pearson's correlation 0.72 with I48N, when averaged over 28 years (1963 to 1991). The observed annual iceberg count represented as a function of observed sea ice extent (in km^2) in the southern part of Labrador, Grand Banks was generally linear over all the iceberg season severity classes. However, the linear regression had a steeper slope (refer to figure 1.5) for the years with higher iceberg severity (when the number of icebergs reaching 48° N latitude in a year crossed 600 and reached up to above 2000), whereas, for years with lighter iceberg severity, the slope was lower. The authors further concluded that the spring Labrador sea ice extent, followed by the winter Davis Strait sea ice extent can be used as a predicting factor for the severity of the iceberg season. The authors attributed this strong correlation to the role played by the sea ice in keeping the icebergs from grounding (that is from being stuck in the shallow coast water) and hence melting down to a smaller sizes, and more importantly in reducing melting of icebergs that happens due to the roughness of the sea surface by dampening the ocean waves. The larger the spring sea ice extent in the Labrador, and in Davis Strait in winter, the longer the icebergs survive and the larger the number they reach southern latitudes, increasing the iceberg severity at 48°N. To simulate the trajectories of northern hemispheric icebergs, [Bigg et al., 1997] used an ocean model, in which icebergs were represented as Lagrangian particles, the drift of which is subject to ocean dynamics. The modelled ocean was seeded with icebergs of different size-classes near the sites with major contributing glaciers. The number of icebergs calved under any particular size class was a lognormal function of length of the iceberg, so that the very large icebergs ($\geq$ 500 meters) were calved in lesser numbers). Based on their analyses, the authors demonstrated that the iceberg trajectories are mostly determined by the perturbation term in the ocean advection. And as the ocean current components and the force generated from that are different over the domain of interest, the location of the calved icebergs have significant influence on the trajectories of icebergs. For example, the icebergs seeded near the southwestern calving spots in the used model drifted across Davis Strait and entered Labrador Sea directly, while those seeded near the central to Northwestern spots took the routes of the Baffin Bay anticyclonic gyre and entered Labrador Sea via BIC. This difference between the iceberg trajectories

introduce discernible effects in the arrival time of icebergs at Labrador Sea, as the oceanic conditions in Baffin Bay impact their longevity [Marko et al., 2014].

1.1.4 Prior studies about factors controlling I48N variability

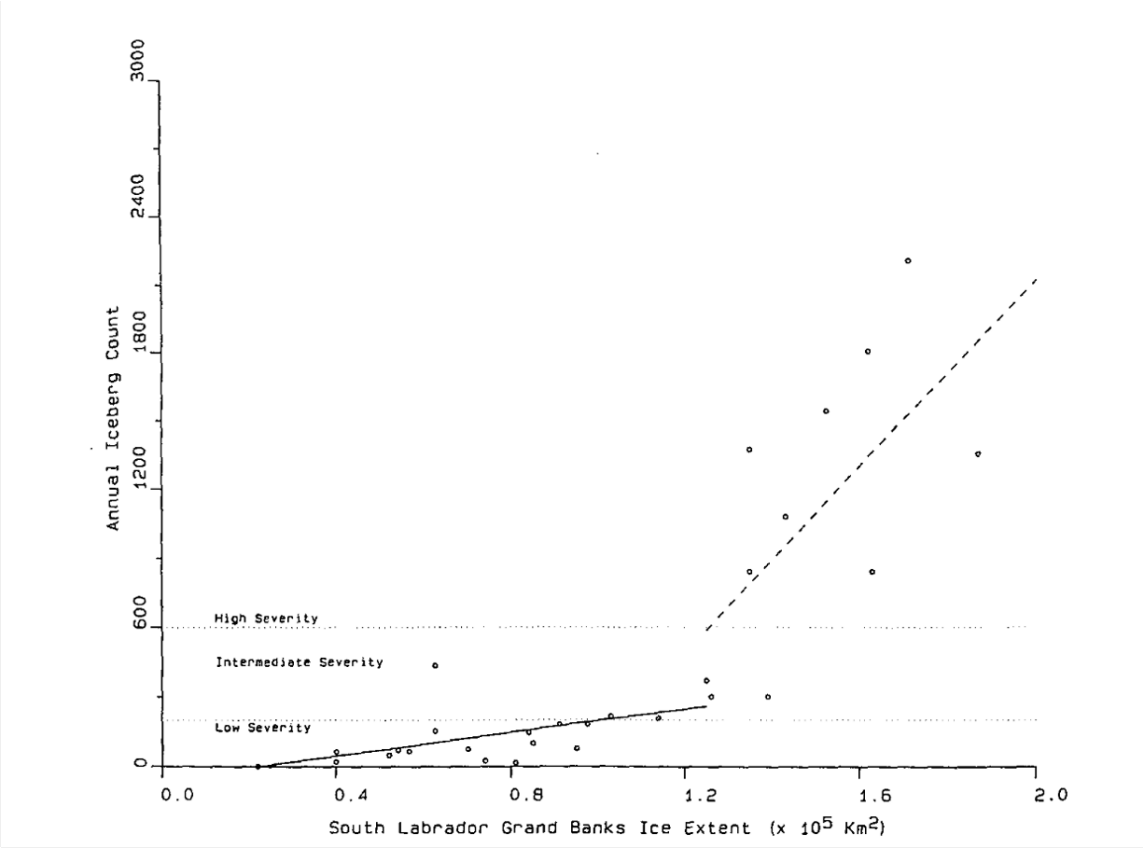

Figure 1.5: Iceberg counts (1963-1991) as function of the 15th April ice extent off South Labrador and Newfoundland, and linear regression lines in both the low and high ice extent regions and the boundaries of the high, low, and intermediate iceberg count categories. Source: [Marko et al., 1994].

[Marko et al., 2014] computed the correlation between the winter Davis Strait sea ice extent (with thickness more than 30 cm) and the severity of the iceberg season. A higher positive Pearson's correlation value indicate that a larger extent of sea ice in the area is interconnected with a heavier iceberg severity along the

east coast of Canada. The authors found that the correlation decreased from 0.642 for the period 1980-1997 to 0.110 for the period 1998-2014. On the other hand, the Pearson's correlation value between the spring sea ice extent in Labrador and the annual iceberg count crossing 48° North latitude increased from 0.352 for the period 1980-1997 to 0.456 for the period 1998-2014. The authors explained that the iceberg flux out of Baffin Bay has a direct connection with the sea ice along the Baffin Island coast, the larger the sea ice extent in the west side of Baffin Bay, the longer the icebergs stay trapped in it, slowing their deterioration. A larger sea ice extent in Davis Strait ensures the survival of the icebergs further south and also might cause some of the icebergs to reach 48° N in later months of the season. Thus, the upstream sea ice condition determines the dwelling time of the icebergs inside the Baffin Bay cyclonic circulation, and so, it could be a controlling factor for their time of arrival at the east coast of Canada. From the comparison between the changes in connections of I48N with the local (Labrador region) and remote (Davis Strait) sea ice conditions across the two periods, the authors concluded that the importance of the environmental factors governing I48N severity shifted downstream in more recent period compared to the end of last century. Furthermore, in a different study [Bigg et al., 2014] with an ocean model simulating Greenland icebergs, the authors found that the icebergs from Baffin Bay arriving approximately six month earlier compared to real-world scenario. The authors attributed this discrepancy to the model resolution that was not high enough to resolve the land-fasting of icebergs in coastal sea ice in Baffin Bay, which in turn failed to delay the modelled icebergs to reach 48°N on time.

In order to find a regional climate index for the Newfoundland and Labrador shelf, [Cyr and Galbraith, 2021] considered cross-correlations among ten different parameters over the Labrador shelf, including I48N, sea surface temperature, ocean bottom temperature, and sea ice extent. They found that the observed season severity of icebergs is reasonably correlated with observed ocean bottom temperature (-0.57) over the Labrador shelf, while its correlation with sea surface temperature was statistically insignificant. A further higher correlation between observed sea ice extent (0.66) and the iceberg season severity in Grand Banks region was found. is one of them, which establishes the interconnection (a Peterson correlation value of -0.76) between iceberg counts and the proposed climate index in Labrador sea as well.

In [Marson et al., 2024], a new parameterization that represents the sea ice forcing on iceberg drift was implemented in a model. (discussed later in details in this chapter). This update in the sea ice parameterization handled the modelled

icebergs' movement inside a sea ice covered Baffin Bay when the icebergs are embedded inside an extensive sea ice pack. Through a sensitivity study using model simulations, the authors established that the seasonality of I48N in terms of the position of the peak month of the season was more realistic in the model after the sea ice locking parameterization was implemented to represent the interaction between Greenland icebergs and the Baffin Bay sea ice.

[Bigg et al., 2014] initiated an auto-regressive model with Fourier-transformed I48N and found out that the interannual variability of the iceberg occurrence along Canada's east coast is not stochastic in nature. In that study, to investigate correlations between oceanic conditions along the iceberg trajectories and I48N they used an ocean model, and concluded that the wind-driven upper ocean dynamics, heat and freshwater exchange between atmosphere and ocean, and the melting of icebergs combined do not suffice to explain the variation in the iceberg season severity. To test the dependence of the iceberg season severity on the calving fluxes from Greenland glaciers, [Bigg et al., 2014] conducted a sensitivity study with two calving forcings: one with a constant calving flux over the years of simulations (that vary from region to region), another with a calving flux that is a function of I48N of the same (next) month for calving spots south (north) to 64° North, and the climatological mean discharge, along with a scale factor to mediate the underestimation of the I48N in the model. The authors found that the simulation with the varying calving distribution attains more realistic results in terms of representing solid discharge from west Greenland glaciers. Therefore, as a conclusion this article suggested that the yearly iceberg count in the north Atlantic shipping lanes is more likely to be a function of variation of Greenland calving flux.

[Wilton et al., 2015] implemented this hypothesis and used the number of icebergs crossing 48°N parallel as a first order proxy for the solid discharge from west Greenland in an ocean-iceberg coupled model. They spun up the ocean model for both the simulations (with different spatial resolutions) for 300 years until the major ocean circulations merged with the same in reality, and then spun up the model with icebergs in them for 10 years before using its output for the monthly iceberg counts crossing 48° N. While the I48N in the run with coarser resolution was mainly composed of icebergs from South Greenland sources, the majority of the icebergs reaching 48° N in the finer resolution model came from the glaciers on the west side of Greenland. This study also pointed out that the inclusion of a sea ice drag approximation in Baffin Bay might have influenced the transit of the icebergs inside Baffin Bay, and in turn impacted their time of entering the shipping lanes. While the authors expected a delaying effect, the sea

ice presence played a role to speed up the icebergs inside Baffin Bay in the experiment. The authors argued that the sea ice likely kept the icebergs away from the Baffin Island coast, and so they crossed Baffin Bay diagonally and reached the southern latitudes earlier causing an earlier peak in the iceberg season. This finding agrees with the finding of [Peterson et al., 2015], where the trajectory of an ice island was monitored with a tracking beacon. Because sea ice was blocking Nares Strait, the iceberg was unable to enter it, until a storm cleared its path.

[Hanna et al., 2013] showed that a negative North Atlantic Oscillation (NAO) Index would cause a warmer summer. This causes larger surface melting from the west Greenland ice sheet, altering the Surface Mass Balance (SMB) of the glaciers, in turn. [Zhao et al., 2016] tested the best fitting function for I48N with options of several combinations of input (exogenous) variables such as SMB of west Greenland glaciers, Labrador Sea Surface Temperature (LSST), NAO, and winter sea ice condition in Newfoundland (NEW) using a non-linear auto-regression model framework. In this study the authors found that I48N season matched best with SMB when lagged by 8 months. They argued that the reason behind this is that most of the modelled icebergs arriving at 48° N come from southwest Greenland sites, after traveling for approximately 8 months. Incorporating the icebergs' travel time to 48° N in a model, [Bigg et al., 2021] attempted to predict the season severity of two consecutive years, although succeeded only in one. The authors advocated that changes in Greenland glacial conditions determines the iceberg season fluctuation more than the environmental factors along the trajectories of icebergs do. To compare the contributions from atmospheric and oceanic forces on the iceberg trajectories, [Zeinali Torbati et al., 2020] deployed four tracking beacons in an ice island during the spring-summer season off the coast of Newfoundland, Labrador. To compute the influence of the different forces (Coriolis, pressure gradient, wind stress, ocean current, and sea ice drag) on the iceberg, this study computed the mass of the four fragments of that iceberg using a deterioration model combined with satellite imagery. In places where sea ice was present with medium to high concentration the drift of the iceberg fragments were found to be influenced by the sea ice drag. Everywhere else, the gradient in the ocean surface height found to dictate the movement of the iceberg.

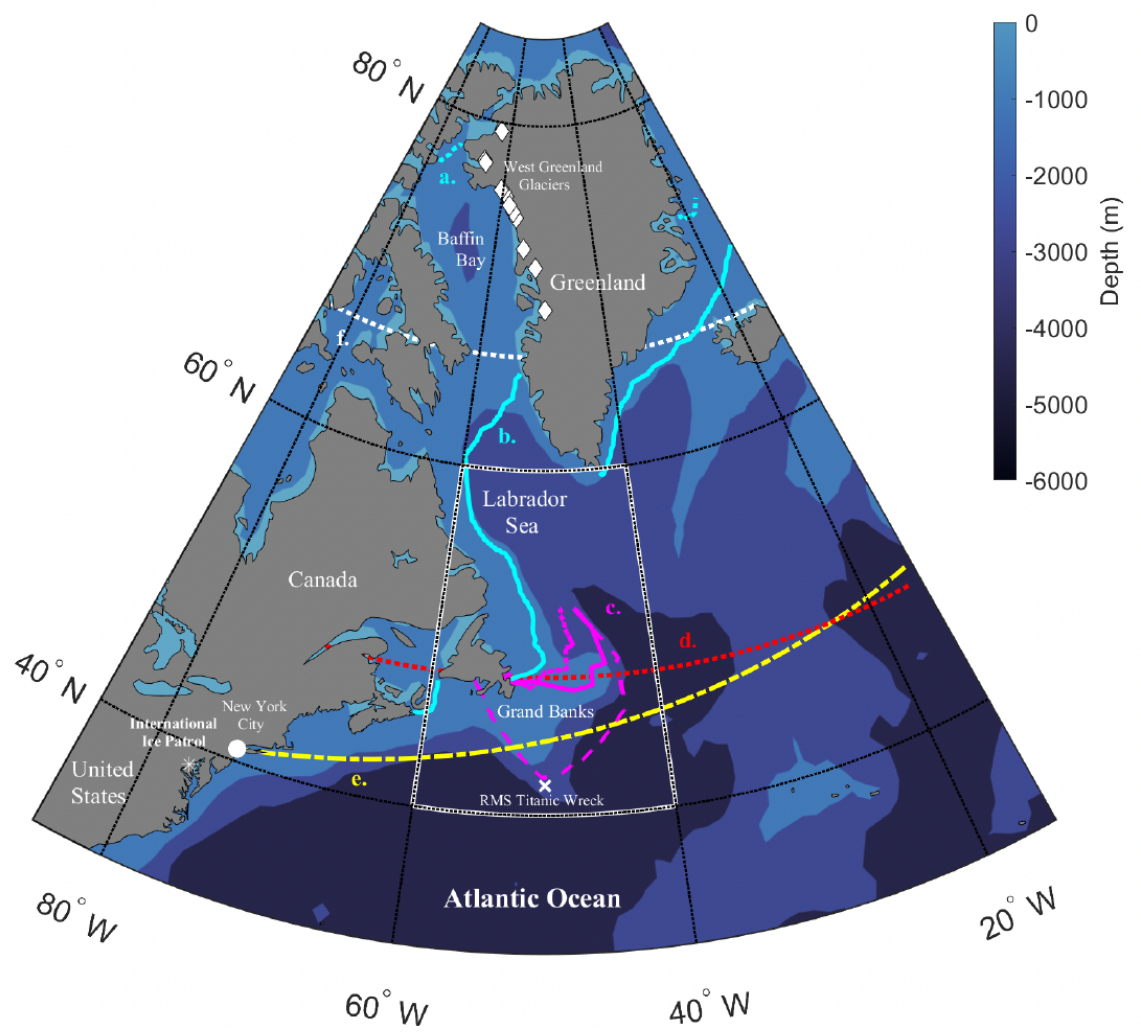

Figure 1.6: Reconnaissance region monitored by International Ice Patrol with collaboration with Canadian Ice Service. International Ice Patrol (IIP) approximate area of responsibility (AOR, white outlined area) around the Grand Banks of Newfoundland, Canada, in the North Atlantic Ocean, where icebergs threaten shipping lanes during the iceberg season. a. The median sea ice extent in September (at its yearly minimum, cyan dotted line) and b. March (at its yearly maximum, cyan solid line) for 1981 to 2010. c. The median mid-January (dotted magenta line), mid-May (dashed magenta line), and early-September (solid magenta line) iceberg limits for 1991 to 2020; prior to about 2010, IIP did not systematically monitor icebergs north of 52°N. d. 48°N (red dotted line); IIP considers this latitude as that south of which icebergs pose a significant threat to the shipping lanes, and records the daily, monthly, and yearly estimated number of icebergs which drift south of it. e. An example transatlantic shipping route (yellow dashed line) along a rhumb line between Southampton, United Kingdom (UK) and New York City, US. Source of figure: IIP report 2023.

1.1.5 Model representation of icebergs

A year after the infamous Titanic tragedy took place, IIP was founded to monitor the region where ships and offshore structures are prone to encounter icebergs in North Atlantic. However, it is not feasible to keep track of all the Greenland icebergs traveling south. In addition to that, due to unfavorable weather conditions and difficulties in data collection, the scarcity of upstream observations of iceberg trajectories outside of the reconnaissance region of IIP (the area delineated by the white outline in the figure 1.6) still prevails. So, in order to have deeper insights about their pathways, representation of icebergs in numerical models became useful. The hemisphere-wide model representation of the primitive drift equations along with thermodynamic equations representing the mass loss of icebergs in the ocean was implemented in [Bigg et al., 1997]. In that study, authors found that the modelled icebergs generally are subject to the balance between the atmospheric and oceanic flows. For example, icebergs released along Southwestern coast of Greenland drift across Davis Strait and follow the BIC southward. Similarly, icebergs from Southeast Greenland glaciers follow the EGC to enter Labrador current. Whereas the icebergs of northern Greenland origins drift into Arctic where ocean currents are weaker, and then started to drift eastward due to the air drag in that region. Furthermore, the authors proposed that including icebergs into ocean models, combined with the knowledge of the lithogenic debris and tracers can be used to validate the palaeoceanographic models for iceberg trajectories in Arctic and North Atlantic. This same model was used in [Gladstone et al., 2001] to represent the trajectories of Antarctic icebergs and the distribution of their meltwater in the Southern Ocean. In [Martin and Adcroft, 2010], an iceberg module built to interact with an ocean model was used to investigate the differences in freshwater distribution over the continental shelf in the Southern Ocean. In this study, the icebergs were clustered and released in the ocean as particles of ten different size categories. with a width:length ratio of 1:1.5. In later studies, this simple yet effective ways of iceberg representation was used in many ocean models to reduce complexity and computational cost. In [Marsh et al., 2015] the iceberg module ICB was introduced in the ocean model Nucleus for European Modelling of the Ocean (NEMO), which we used for the current study. Throughout the upcoming years, new parameterizations took the NEMO model representation of icebergs closer to the real world scenario. For example, [Merino et al., 2016] introduced the application of the ocean fields acting along the whole keel of an iceberg instead of just the surface ocean fields in NEMO-ICB. This was implemented for the northern hemispheric configuration of the same model by [Marson et al., 2018].

In this study, the authors found that icebergs drift along the shelf break under the vertically integrated sub-surface ocean fields which is an accurate representation of their trajectories. [Rackow et al., 2017] implemented a *sea ice locking* parameterization to study Antarctic icebergs. Apart from the sea ice drag term in the dynamic equation (details in next chapter), another effect of sea ice was introduced in the aforementioned study. The sea ice ridges (bigger than iceberg freeboard) above the ocean surface interact more with the wind. Therefore, when the sea ice cover is heavy, the icebergs trapped inside the sea ice pack move faster than their usual speed. Inclusion of this factor improved model representation of iceberg. The above-mentioned upgrade were tailored and implemented for Greenland icebergs traveling through Baffin Bay sea ice pack in [Marson et al., 2024].

1.2 Problem

In the previous subsection, we discussed some of the prior studies regarding the interannual variation of iceberg severity in the east coast of Canada. Clearly, the literature is not in agreement about the major determining factor behind the year-to-year fluctuation in iceberg season. The drift and deterioration models used by the IIP enable them to predict the season severity only by the middle of the season using sea ice predictions, and historical statistics of the distributions of monthly iceberg counts [Rudnickas, Serumgard,] (IIP annual report 2018). In addition, albeit the advancements detailed in the previous subsections improved the model depiction of icebergs, iceberg models are still far from realistically representing the severity of the iceberg season in the East Canadian coast, and therefore from predicting the upcoming seasons accurately. Therefore, to forecast an iceberg season, one must have deeper insights of the factors playing important roles behind the variation in iceberg fluxes entering the North Atlantic shipping lanes.

1.3 Research goals

To improve model representation of the icebergs in the Northern Hemisphere, it is necessary to find the factor(s) that govern the interannual variability of the iceberg season severity in the Grand Banks to ensure that these forcings are well represented in iceberg models. This formed the research question for this project:

What are the most important factors that determine the severity of the iceberg seasons along the east coast of Canada?
And to address this question the three main objectives for the current research are:

1. Analyzing observed characteristics of the iceberg severity, and its correlations with potential environmental drivers.

2. Evaluating existing results from an iceberg model in terms of those potential governing factors, and the correlations with the same drivers.

3. Comparing the existing model's outcomes with the outcomes from another simulation forced with different atmospheric condition to investigate how an alteration in atmospheric data impacts the iceberg season characteristics.

1.4 Relevance

International Ice Patrol (IIP) asserted that the year-to-year variation of iceberg counts along the east coast of Canada has increased in an abrupt manner. As the ice-free season widens in the context of the recent Arctic warming, marine operations increase simultaneously. In this scenario, a lack in the observational data from north of the reconnaissance region of IIP, and an absence of desired accuracy in predictions of iceberg seasons in the Grand Banks call for further improvements in icebergs' representation in models. Prior studies suggested that regional ocean temperature, sea ice condition are correlated with the iceberg season severity. Others attributed the interannual variability of the iceberg counts in the Grand Banks region to the upstream ice conditions along the iceberg trajectories, the North Atlantic Oscillation Index (NAOI), also the calving rates from Greenland glaciers.
In this study we evaluated the interconnections between some of those potential environmental conditions and the yearly iceberg count along east Canadian coast, both using observations and numerical model experiments. Furthermore, to investigate the effect of iceberg field stabilization on the relationships between the governing factors and the iceberg severity, we initiated a longer model simulation with icebergs present in the model, in a second experiment. A different atmospheric forcing was used in this experiment in order to explore the impact of iceberg mass loss on the iceberg season severity in the Grand Banks. Through this modelling study, we found that factors other than those previously

suggested play a major role in the distribution of icebergs flux coming out of Baffin Bay, and therefore, downstream of it.

1.5 Thesis structure

This thesis is comprised of four chapters. Chapter 1 narrates the study area, the topic of the study, the gaps in the research, and an outline of the thesis goals. Chapter 2 delivers a thorough explanation of the methodology implemented in this study, and details about the observational datasets used. It also describes the configuration of the model used, and provides specific details of the two experiments. Chapter 3 presents the results and detailed discussion divided into three sections, that address the three research objectives described in the section *Research goals*. Finally, in Chapter 4, there is a summary of the research, followed by potential biases and conclusion of the study.

Chapter 2

Data and methodology

2.1 Observational data

To analyze relationships between I48N and environmental factors that Greenland icebergs are exposed to, and to evaluate the model, we used observational (or observation-based) datasets for iceberg sighting south of 48° N latitude, ocean temperature, sea ice concentration, and solid discharge from Greenland.

Iceberg sighting

Within a year of the Titanic tragedy (1912), the IIP was established to monitor the waters from 40°N to 52°N (refer to figure 1.6) off the east coast of the United States of America and Canada. Along with hourly forecasts, the IIP provides iceberg sightings information collected by ships, airborne RADAR, and satellite as their reconnaissance technology improved with time. In 2006, they merged their operations with the Canadian Ice Service (CIS) in order to provide a larger coverage (40°N to 60°N). Among all the iceberg sighting datasets, **I48N** is the most widely used one. Based on the evolving technology used for iceberg sighting, the IIP divided the total time covered in their dataset into three reconnaissance periods: (i) 1900 to 1945: period of iceberg sighting reported by U.S. Coast Guard (USCG) Cutters and commercial vessels, (ii) 1946 to 1982: period when the IIP introduced visual monitoring (without RADAR) by aerial patrolling based on commercial vessels' reports, and (iii) 1983 to present: the modern era characterized by airborne RADAR observation, satellite observation, and by implementation of iceberg drift and deterioration models that provide predictions of icebergs' positions.

To quantify the severity of the iceberg seasons along the east coast of Canada, the IIP developed an index called Normalized Season Severity Index (in short NSSI) that consists of three metrics: (i) Limit of All Known Ice (LAKI = area south of 48° N that is enclosed by the Iceberg Limit), (ii) Length Of Season (LOS = the number of days icebergs are present south of 48° N), and (iii) South of 48° N latitude (I48N = the count of icebergs crossing 48° N latitude line over the season). All these metrics are normalized using equation 2.1 with their corresponding means of the associated reconnaissance period in order to be summed into the unitless index NSSI.

$$X^{'} = min^{'} + \frac{(X - min)(max^{'} - min^{'})}{(max - min)} (2.1)$$

Where,
$X^{'}$ = the normalized value of the corresponding metric
X = the observed value of the metric
$min^{'}$ = smallest values of metric during the corresponding reconnaissance period
$max^{'}$ = largest values of metric during the corresponding reconnaissance period
max = maximum value of the normalization scale = 100
min = minimum value of the normalization scale = 1
However, the metric I48N is most widely used, mainly for two reasons: (i) other metrics can confidently be dated back up to only 1975, whereas I48N dataset dates back to 1900, (ii) the NSSI can not be computed until the season ends (because of LOS). Therefore, to make the I48N dataset even more cognizable, the IIP defined four severity classes for each period, using the middle fifty percent regime derived from the normalized statistical measures associated with each reconnaissance period (IIP Annual report [Rudnickas, Serumgard,]), which we discuss in details in the next subsection.

Categorizing iceberg severity classes

Replacing (max - min) with 100 and $max^{'} - min^{'}$ with R_{period} in the equation 2.1, the normalized I48N could be computed from the absolute I48N value as follows:
$(X^{'} - min^{'})100 = (X - min)R_{period}$
$X - min = \frac{(X^{'} - min^{'})100}{R_{period}}$
$X = min + \frac{(X^{'} - min^{'})100}{R_{period}}$
That is for the iceberg count variable the first equation becomes:
$I48N^{'} = min^{'} + \frac{(I48N - min)R_{period}}{100}$

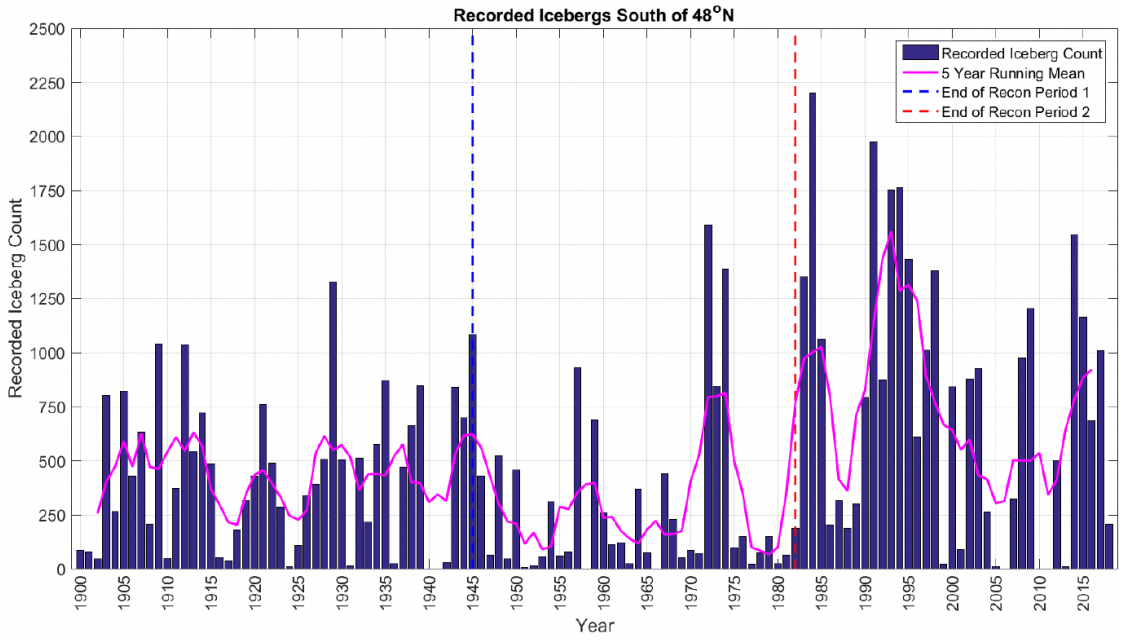

Figure B-1. Count of icebergs passing south of 48°N from 1900 to 2018. The magenta line represents a five-year centered running mean used for a low pass filter and the dashed lines demark the break-points in reconnaissance periods.

Figure 2.1: Source of figure: International Ice Patrol annual report, 2018.

and the last equation becomes:

$$I48N = min + \frac{(I48N^{'} - min^{'})100}{R_{period}}$$

Now, with an year's total I48N, the minimum annual total of the reconnaissance period (for all three reconnaissance periods the minimum is zero, so in the equation above $\text{min}^{'} = 0$), the minimum value of the normalization range (0 to 100) i.e. min = 0, and the range of iceberg counts of the considered period, one can compute the normalized iceberg counts for that year, i.e. $\text{I48N}^{'}$ from the first equation. We can try to elaborate it with the following example. In the year 1921 (from October 1920 to September 1921) approximately 750 (refer to the figure 2.1) icebergs crossed 48° North. The year 1921 belongs to the first reconnaissance period, the range of which is 1300 (min = 0, max = 1300). Therefore the normalized value of iceberg count is $\text{I48N}^{'} = 57.7$ from the first equation. Iceberg counts south of 48° North are normalized for all the years in the same way as described above. The figure 2.4 shows the timeseries for $\text{I48N}^{'}$. The IIP used the middle 50% method to divide the iceberg seasons into four severity classes (a

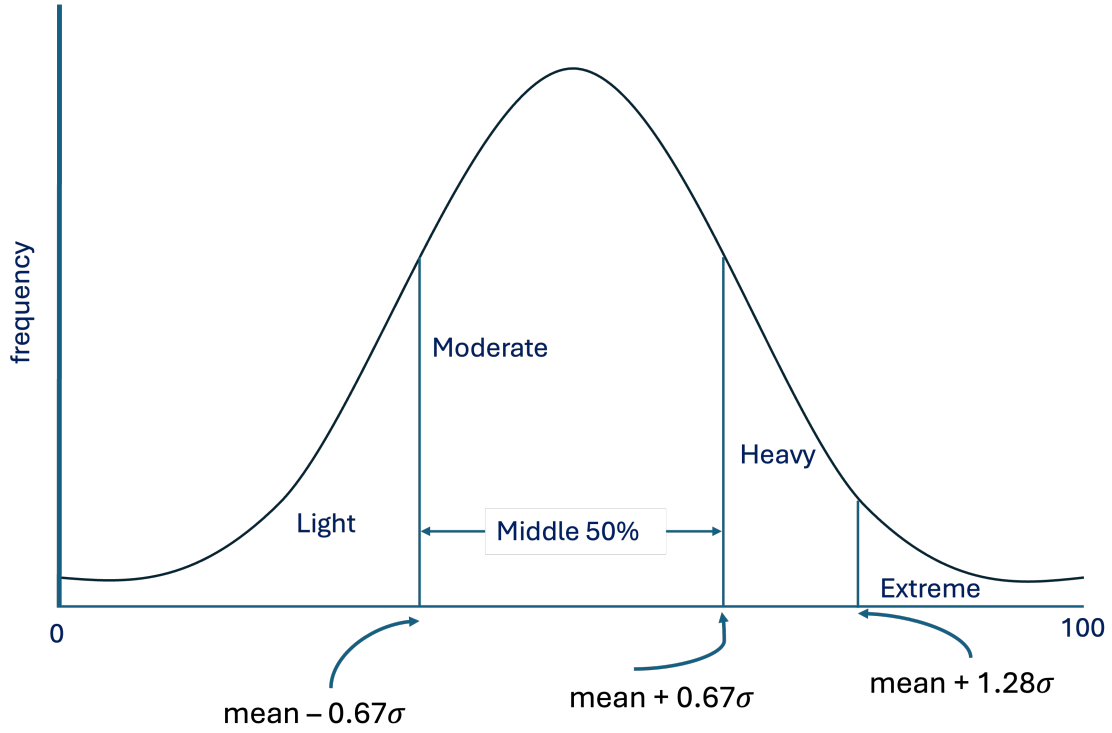

Figure 2.2: A diagram of middle 50% method, where σ = standard deviation of the dataset. The dataset is scaled to a range from 0 to 100.

schematic for frequency distribution of icebergs is illustrated in figure 2.2, and a table sourced from the IIP annual report is shown in figure 2.3). For each period, when the I48N value belongs to the middle 50%, the season is termed as "Moderate". When it belongs to the lower 25%, the season is termed as "Light". the higher 25% is further divided into two categories, first 15% is called "Heavy", and the upper 10% is "Extreme". Now to elaborate the same example of the year 1921, we see that the bar is red in the figure 2.4, which conforms with the value 57.7 falling in the "Heavy" category of the iceberg season in the east coast of Canada.

Table 2.1 shows the statistical elaboration of the middle fifty percent method used by the IIP to categorize the iceberg season severity:

- Moderate if the variable value falls between its $mean \pm 0.67$ standard deviation
- Light if the variable value falls between 0 and its $mean - 0.67$ standard

		Mean	0.67448σ	1.28σ	Median	Light Range	Moderate Range	Heavy Range	Extreme Range
1900-2018	Normalized Values	29.48	18.10	34.35	22.76	0 - <11.4	11.4 - <47.6	47.6 - 63.8	>63.8
Period 1	Severity Class Definition (# of Icebergs)					0 - 140	141 - 625	626 - 843	≥ 844
Period 2	Severity Class Definition (# of Icebergs)					0 - 166	167 - 747	746 - 1008	≥ 1009
Period 3	Severity Class Definition (# of Icebergs)					0 - 230	231 - 1036	1037 - 1398	≥ 1399

Table B-5. Statistical analysis of the normalized iceberg count from 1900 to 2018. The top row shows the statistics and threshold values associated with the normalized iceberg values calculated from Equation B-1 and using the 50% method. The Period 1, 2, 3 rows show the number of icebergs in each Reconnaissance Period that correspond with the statistical thresholds for the four severity classes.

Figure 2.3: Transformation metrics used by International Ice Patrol to define the upper and the lower limits of severity classes of iceberg seasons during different reconnaissance periods. Source of figure: IIP annual report, 2018.

deviation

- Heavy if the variable value falls between its $mean + 0.67$ SD and $mean + 1.28$ standard deviation
- Extreme if the variable value falls above its $mean + 1.28$ standard deviation

Table 2.1: Definition of severity classes of iceberg season. I48Nobs = observed value of I48N for that season, $\overline{I48N}$ = mean of the normalized observed I48N over the whole period of observation, σ_{I48N} = standard deviation of the normalized observed I48N over the whole period of observation

classes	ranges
light	$I48Nobs <= \overline{I48N} - 0.67\sigma_{I48N}$
moderate	$\overline{I48N} - 0.67\sigma_{I48N} < I48Nobs < \overline{I48N} + 0.67\sigma_{I48N}$
heavy	$\overline{I48N} + 0.67\sigma_I 48N <= I48Nobs < \overline{I48N} + 1.28\sigma_{I48N}$
extreme	$I48Nobs \geq \overline{I48N} + 1.28\sigma_{I48N}$

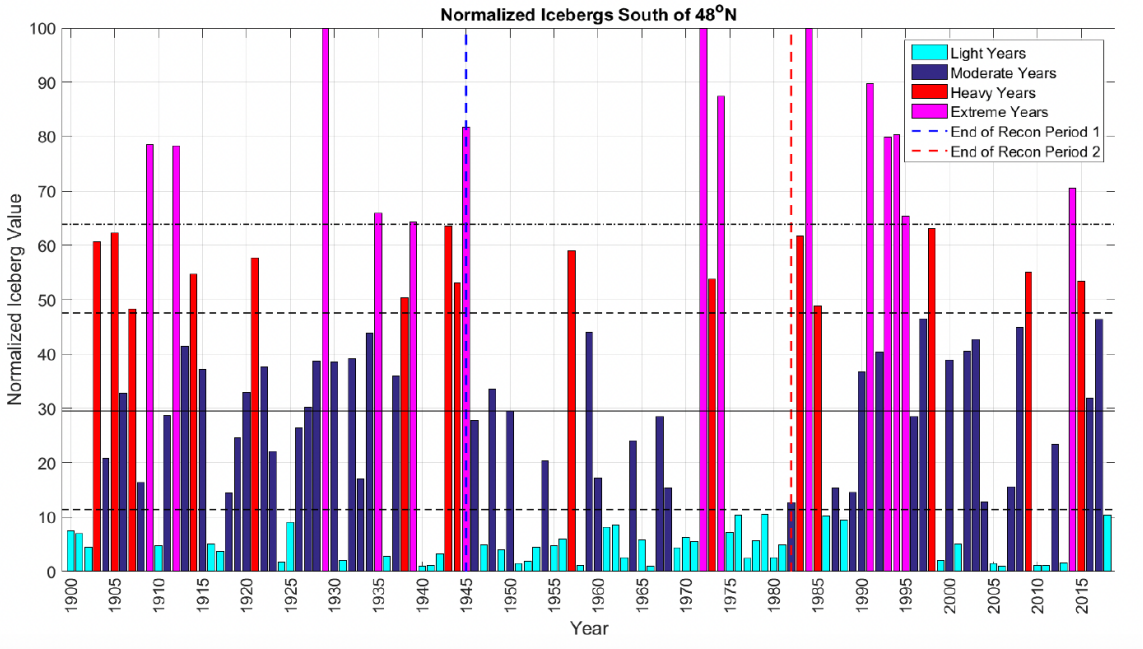

Figure 2.4: The iceberg counts normalized to the range of 0 to 100 for each reconnaissance period of IIP.

Using the method explained above, IIP-I48N dataset was divided into four severity classes with the ranges tabulated in the table 2.1. For this study, I48N was taken from that IIP I48N dataset available as a comma-separated value file that have counts of icebergs crossing 48° N latitude for all the months starting from October 1989. The IIP defines an iceberg season of a particular year as October of previous year to September of the corresponding year. As an example,

Table 2.2: Definition of severity classes of iceberg season based on iceberg counts South of 48°N.

Periods	Light	Moderate	Heavy	Extreme
1900-1945	0-140	141-625	626-843	$\geq$ 844
1946-1982	0-166	167-746	747-1008	$\geq$ 1009
1983-present	0-230	231-1036	1037-1398	$\geq$ 1399

if during the period from October 1994 to September 1995 more than 1399

icebergs traveling southward crossed 48° N latitude, the 1995 iceberg season is classified as an extreme season. IIP-I48N is the dataset we used to evaluate the model's representation of the season severity patterns. For this study, IIP I48N dataset as a comma-separated value file was used. It has counts of icebergs crossing 48° N latitude for all the months starting from October 1989. The IIP defines an iceberg season of a particular year as October of previous year to September of the corresponding year.

Ocean temperature

To determine the influence of the local ocean temperature on I48N, we used the three dimensional temperature field of the Multi Observation Global Ocean ARMOR3D dataset provided by the Copernicus Marine Service (CMS, https://doi.org/10.48670/moi-00052). ARMOR3D is comprised of near-real-time data reprocessed from in-situ and satellite observations. It has a spatial resolution of 0.25° x 0.25°, and 50 vertical levels, a monthly temporal resolution, and offers a temporal coverage of 30 years (January 1993 to December 2022).

Sea ice

To investigate how the iceberg season severity is impacted by the local and remote sea ice conditions that icebergs encounter en route to the Grand Banks, we used the sea ice concentration data (https://doi.org/10.5067/8GQ8LZQVL0VL) derived from the Scanning Multichannel Microwave Radiometer (SMMR on the Nimbus-7 satellite), the Special Sensor Microwave/Imager (SSM/I sensors onboard the Defense Meteorological Satellite Program's i.e. DMSP -F8, -F11, and -F13 satellites), and the Special Sensor Microwave Imager/Sounder (SSMIS boarding DMSP-F17 satellite). The product offers a spatial resolution of 25 km x 25 km, and a monthly temporal resolution between 1979 and 2023. It used filters to eliminate invalid data due to weather effects, such as storms and cloud coverage. Even though this product provides a well-defined ice margin, and a reasonably high value in the middle of the ice pack, it under-estimates the realtime concentration gradient at the edge of the ice due to drop in the emissivity of ice because of thinning [Ivanova et al., 2015] or melting [Kern et al., 2020].

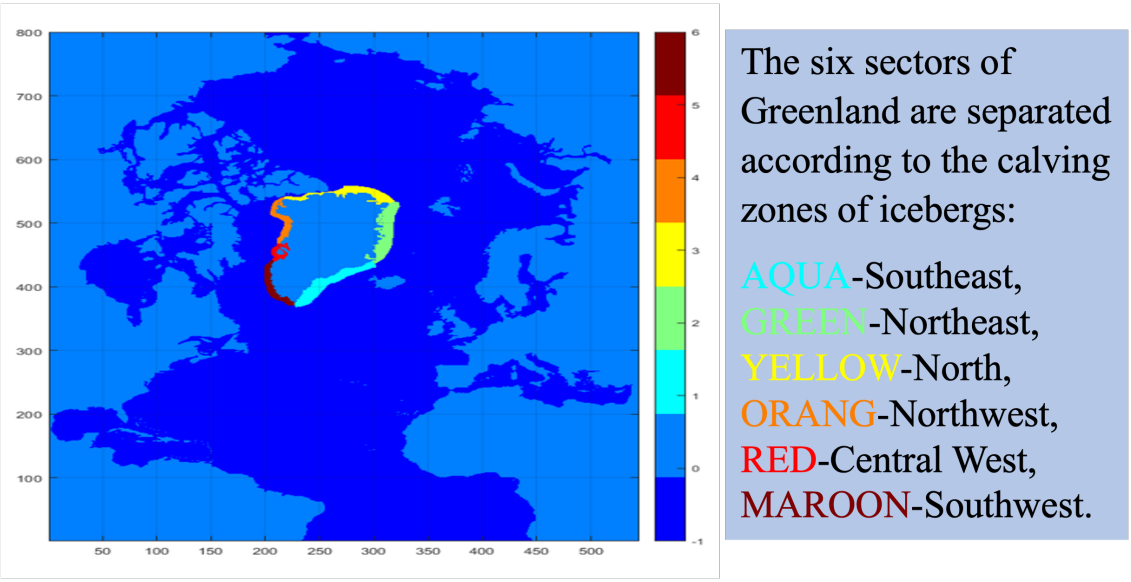

Figure 2.5: The six sectors of Greenland solid discharge defined for the following analyses.

Calving

To analyze the relationship between the Greenland calving rates and the I48N variation we utilized the [Bamber et al., 2018a] dataset which covers the period between 1958 and 2016 [Bamber et al., 2018b]. Solid discharge varies depending on the surface mass balance of the Greenland ice sheet, and is computed from the product of glacial ice velocity and ice thickness at the gate of marine terminating glacial outlets. For a prescribed value of ice density (918 kg/m^3), the volume flux (= the area of the gate multiplied by the velocity of the ice flow at the gate) representing the time rate of mass loss (dm/dt) through the glacier gates was computed as the temporal change in the ice thickness at the gate (a vertical rectangle frame across the terminal width) in [Bamber et al., 2018a]. The surface velocity is interpolated from a sub-annual to annual timeseries of high resolution (in space and time both) satellite observation, and the ice thickness is taken from ground-penetrating RADAR observations. The seasonal rate of calving at different outlets were reanalyzed from the sub-annual to annual satellite observation of surface velocity or were derived from the liquid runoff-solid discharge correlations in cases of years with no observation. Among the Greenland icebergs that populate the iceberg alley every year, most contributions

come from the calving along the northwest coast of Greenland, followed by termini in the Disko Bay region, and southwest and southeast coasts [Bigg et al., 2014]. Therefore, for more robust analysis, we divided the whole solid discharge from Greenland (the calving dataset from [Bamber et al., 2018a]) into six sectors, namely Southeast, Northeast, North, Northwest, Central West, and Southwest (refer to figure 2.5). We used contributions to modelled I48N from different sectors to understand the relative impacts of the environment factors in different portions of the iceberg trajectories in the model.

2.2 Model outputs

2.2.1 Model description

In this study, the general circulation model, Nucleus for European Modelling of the Ocean (NEMO, version 3.6, [Madec and Imbard, 1996]) is used. It is a deterministic hydrostatic ocean model coupled with the sea ice model Louvain-la-neuve Ice Model version 2 (LIM2, [Fichefet and Maqueda, 1997]; [Bouillon et al., 2009]). NEMO uses a finite difference scheme to solve the dynamic and thermodynamic equations at every grid point for each timestep, with the following assumptions:

1. Spherical Earth approximation: Earth's geopotential surface is assumed to be a sphere. That is, the Earth is assumed to be a perfect sphere with a single radius of 6371.229 km.

2. Thin-shell approximation: the ocean depth is considered to be negligible compared to Earth's radius

3. Turbulent closure hypothesis: turbulent fluxes, i.e., the departure from the mean in velocity fields, are downscaled to be depicted as functions of the ocean's mean velocities

4. Boussinesq hypothesis: density variations is used only to calculate their contributions to the buoyancy force, and is neglected otherwise. This hypothesis makes the model to ignore the small deviations in density (for example by disregarding the difference in viscosity between two adjacent layers of the fluid), while accounting for the big deviations in density which are critical (for example by retaining the effect of gravity through incorporating natural convection).

5. Hydrostatic hypothesis: the vertical component of the momentum conservation equation is reduced to a balance between the pressure gradient force and the buoyancy force. So, convective processes need to be parameterized as necessary.

6. Incompressibility assumption: the change in pressure has a negligible effect on the change in density of the ocean water. So the divergence of ocean velocities vector is set to zero for the equation. That is, the amount of the ocean fluid inside the control volume stays constant.

Sea ice component

This ocean component Océan Parallélisé (NEMO-OPA) is coupled with LIM2, a thermodynamic-dynamic sea ice model that represents sea ice as a slab of three layers (two of sea ice, one of snow at the top), each of same thickness. Albedo is represented as a function of sea state, snow and ice thickness, and cloud coverage. Brine pockets can capture shortwave radiation and store that as latent heat. Ocean water is parameterized to enter the snow if the snow-ice interface is immersed under the sea surface. For the dynamic part, the ice is simulated as an elastic-viscous-plastic (EVP) that interacts with the atmosphere and the ocean. Based on the fraction of the grid cell that is ice covered, NEMO-LIM computes all the air-sea fluxes.

ICB module

[Marsh et al., 2015] coupled an iceberg model with the eddy-permitting configuration of NEMO, and it has been a part of NEMO (called ICB module) since the version 3.6 was released. It provides a broad spectrum of iceberg diagnostics including daily position, current dimension, and environmental conditions surrounding the icebergs [Marsh et al., 2015]. All icebergs are represented as cuboids, with a length:width ratio of 1.5, and a temperature equal to -4° C. The ICB module distributes that mass accumulation into ten size classes according to the calving distribution presented in table 2.3 (source: [Martin and Adcroft, 2010]). For a visual representation, one can refer to the Figure 2.6. Icebergs' thicknesses vary form 40 meters to 250 meters. To keep it consistent with observed terminus thickness of glaciers at the calving fronts, the upper limit of thickness is 250 meters for six of the upper size classes. From [Bamber et al., 2018b] dataset, the monthly calving values at the discrete catchments at the marine terminating glacier gates are mapped to the model grid

Table 2.3: Iceberg size calving distribution in NEMO model. The mass scaling factor (column 5) is an integer that stands for the number of icebergs in one particle (refer to figure 2.6). Calving rates are distributed according to the fractions listed in the last column. source: [Martin and Adcroft, 2010] 2010.

Category	Length(m)	Thickness (m)	Mass(kg)	Mass scaling	Calving distribution
1	60	40	$8.8 * 10^7$	2000	0.24
2	100	67	$4.1 * 10^8$	200	0.12
3	200	133	$3.3 * 10^9$	50	0.15
4	350	175	$1.8 * 10^{10}$	20	0.18
5	500	250	$3.8 * 10^{10}$	10	0.12
6	700	250	$7.5 * 10^{10}$	5	0.07
7	900	250	$1.2 * 10^{11}$	2	0.03
8	1200	250	$2.2 * 10^{11}$	1	0.03
9	1600	250	$3.9 * 10^{11}$	1	0.03
10	2200	250	$7.4 * 10^{11}$	1	0.02

in the form of mass accumulation of land ice at the grid points closest to the corresponding marine termini. Each termini has ten bins associated with ten size classes. Once enough mass (corresponding elements from the fourth and the fifth columns multiplied) in the bin associated to a specific category is accumulated for it to be "full" (critical mass) the particle is spawned in the modelled ocean. Once calved, those particles containing a number of icebergs (determined by its category according to table 2.3) are treated as single Lagrangian parcels and are subject to the model physics, according to the equations presented next.

Primitive equations

The iceberg dynamic and thermodynamic equations have been developed since the 1970's ([Wolford et al., 1973], [Robe et al., 1980], [Mountain, 1980]). The set originally implemented in NEMO come from [Martin and Adcroft, 2010] (presented again by [Marsh et al., 2015]). Improvement in parameterizations were introduced and implemented in [Merino et al., 2016], [Rackow et al., 2017], [Marson et al., 2018], and [Marson et al., 2024]. The model solves the equations for each timestep (18 minutes in our configuration) for all the particles in the model domain.

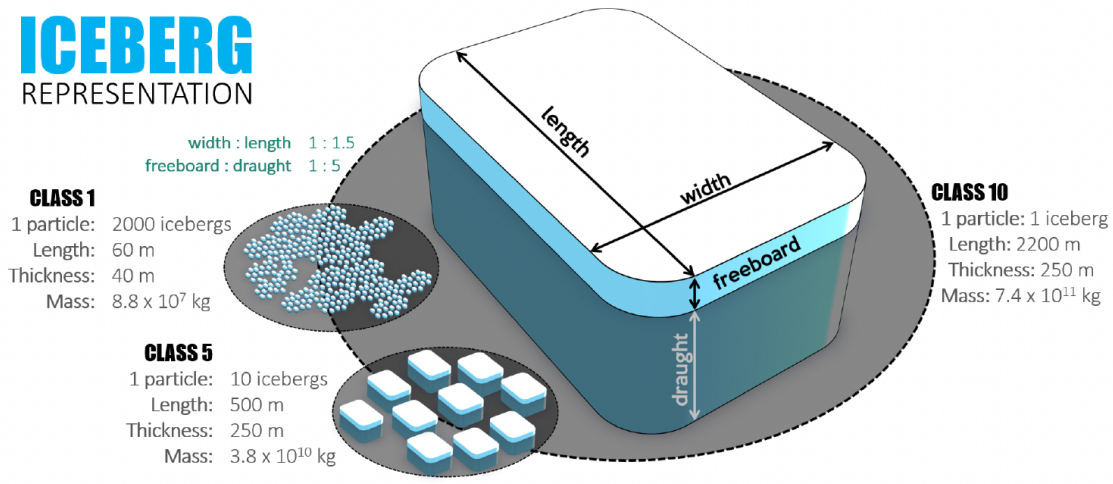

Figure 2.6: Model representation of particles with icebergs of different size classes. (schematic courtesy: Dr. Juliana M. Marson)

1. Drift of icebergs

Equation 2.2 explains the law of conservation of momentum, that portrays how the icebergs drift in the ocean:

$$M\frac{d\vec{v}}{dt} = \vec{F_p} + \vec{F_c} + \vec{F_r} + \vec{\tau_a} + \vec{\tau_o} + \vec{\tau_i} \tag{2.2}$$

Here M is the mass of the iceberg, and v is its velocity. In the right-hand side of the equation:
$\vec{F_p} = -Mg\vec{\nabla}\eta$
is the pressure gradient force, where η is the slope of the ocean surface
$\vec{F_c} = -M\vec{\Omega} \times \vec{v}$
is the coriolis force, where $\vec{\Omega}$ is the Earth's diurnal rotation vector
$\vec{F_r} = \rho_0\, C_r\, g\, a\, min(a, F)\, \frac{2LW}{L+W}\, \frac{\vec{v_a}}{|\vec{v_a}|}$
is the wave radiation force, where
ρ_0 is the density of the seawater,
C_r is a variable coefficient that dampens $\vec{F_r}$ acting on the icebergs when the iceberg length is smaller than a threshold (0.125 times the wavelength of the surface wave),
a is the wave amplitude (an empirical function of wind speed relative to the ocean current),

F is the freeboard of the iceberg,
L is the length of the iceberg,
W is the width of the iceberg,
$\vec{\tau_a} = \rho_a(0.5C_{av}WF + C_{ah}LW)\ |\vec{v_a} - \vec{v}|(\vec{v_a} - \vec{v})$
is the air drag
$\vec{\tau_o} = \rho_o(0.5C_{ov}W(D - T_i) + C_{oh}LW)\ |\vec{v_o} - \vec{v}|(\vec{v_o} - \vec{v})$
is the water drag
where
D is the draft of the iceberg, and
T_i is the thickness of sea ice.
$\vec{\tau_i} = \rho_i 0.5\, C_{iv}\, WT_i\ |\vec{v_i} - \vec{v}|(\vec{v_i} - \vec{v})$
is the ice drag
In the last three equations,
$\vec{\tau_x}$ represents the drag force for medium 'x',
ρ_x represents the density of the medium 'x',
C_{xv} represents the vertical drag coefficient of the medium 'x',
C_{xh} represents the horizontal drag coefficient of the medium 'x',
$\vec{v_x}$ represents the velocity of the medium 'x',
('x' being 'a', 'o', and 'i' for atmosphere, ocean, and sea ice respectively).

2. Disintegration of icebergs

The disintegration of icebergs is represented by equation 2.3 that portrays how icebergs melt in the ocean:

$$\rho\frac{d(LWT)}{dt} = \rho(-LWM_b - T(L + W)(M_e + M_v)) \tag{2.3}$$

for an iceberg with density ρ. Melting and erosion of icebergs are mainly controlled by four processes:

1. turbulent heat transfer at the bottom part of the icebergs (M_b),
2. buoyant heat convection along the side walls of the icebergs (M_v),
3. wave erosion at the sea surface (M_e), and
4. surface melt due to insolation at the freeboard part of the icebergs.

As the last one has a negligible order of magnitude in comparison with the first three, it is not taken into account in the mass balance equation. These processes are parameterized as follows:

$M_b = 0.58|\vec{v} - \vec{v_o}|^{0.8} \frac{\tilde{T_o} - \tilde{T}}{L^{0.2}}$ is the melt rate due to turbulent heat transfer
where
$\tilde{T_o}$ is the sea surface temperature, and
$\tilde{T}$ is the effective iceberg temperature (assumed to be $-4°$ C)
$M_v = 7.62 \times 10^{-3}\, \tilde{T_o} + 1.29 \times 10^{-3}\, \tilde{T_o}^2$ is the melt rate due to buoyant convective heat transfer
$M_e = 1/12\, S_s(1 + \cos(\pi {A_i}^3))(\tilde{T_o} + 2)$ is the melt rate due to wave erosion
where S_s is the sea state, empirically defined as
$S_s = 3/2\, |\vec{v_a} - \vec{v_o}|^{0.5} \; + \; 1/10\, |\vec{v_a} - \vec{v_o}|$
A_i is the sea ice area

Sea ice locking

In addition to the sea ice drag (the last term on the right hand side of equation 2.2), in this simulation we chose a more realistic sea ice forcing parameterization of namely Sea Ice Locking (SIL) parameterization, described by [Lichey and Hellmer, 2001] and modified by [Rackow et al., 2017]. The SIL parameterization was respectively, and introduced in NEMO by [Marson et al., 2024]. In this parameterization, when the sea ice has a high concentration ($\geq 90\%$), the iceberg is trapped in sea ice pack and moves as one solid block with the ice pack. With this parameterization activated, NEMO-ICB computes the sea ice strength as a function of the LIM2-calculated (a) concentration, (b) thickness of sea ice, at the iceberg's location. Four different regimes are established based on the sea ice concentrations (SIC) as follows:
(i) SIC $< 15\%$: For the first regime, the the sea ice drag force is set to zero in the equation 2.2, and the iceberg velocity would be the function of the other five forces acting on it.
(ii) $15\% \geq$ SIC $< 86\%$: sea ice drag is computed as originally coded (equation 2.2).
(iii) $86\% \geq$ SIC $< 90\%$: a sea ice locking co-efficient λ as a function of thickness and strength is established and the iceberg velocity is modified based on that as follows:
$\vec{V}_{icb} = (1 - \lambda) \cdot \vec{V}_{\sum F} + \lambda \cdot \vec{V}_{si}$, where $\vec{V}_{\sum F}$ = the primary iceberg velocity derived from equation 2.2, and $\vec{V}_{si}$ = the velocity of sea ice. That is, based on the value of the coefficient λ, the iceberg velocity is a weighted combination of the velocity derived from the forces in the momentum equation, and the sea ice velocity derived from LIM2 model.
(iv) SIC $> 90\%$: the velocity field resulted by the net force acting on the iceberg

parcel is set to zero, and the parcel moves as one with the sea ice pack. This latest parameterization ushered the representation of icebergs trajectories closer to observations in the northwest Atlantic (for more detail refer to [Marson et al., 2024]).

2.2.2 Configuration

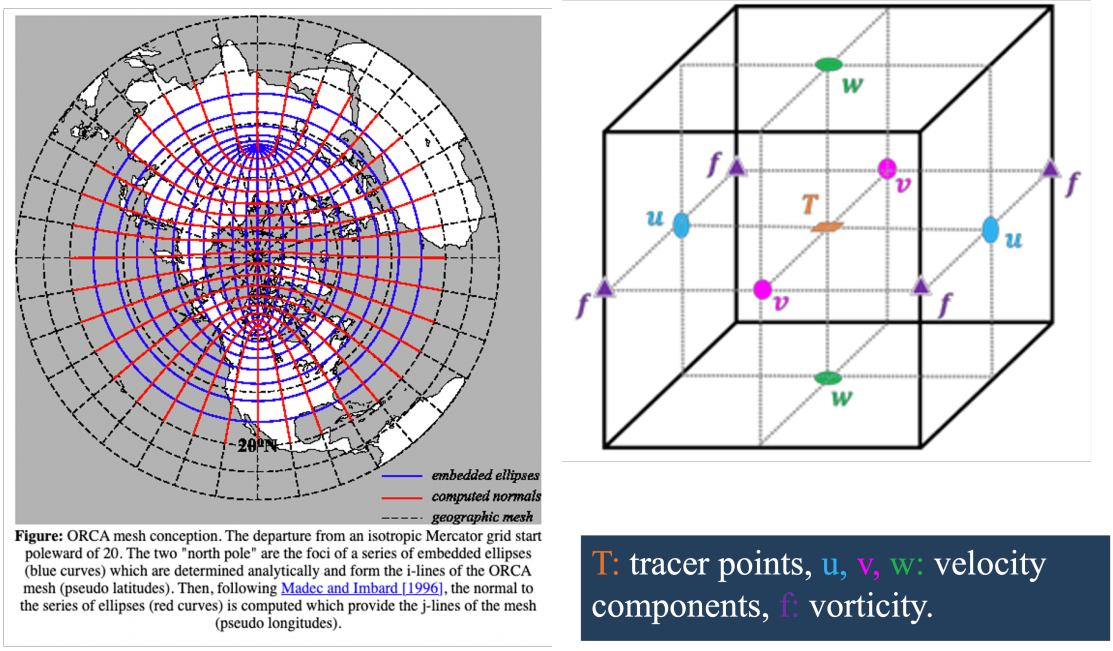

(a) Tripolar Grid of NEMO model (b) Arakawa C grid.

Figure 2.7: (a): Tripolar grid of the model, (b): The locations of the variables diagnosed in the three dimensional Arakawa C grid of the model.

As an ocean model, to avoid having singularity problems inside the computational domain at the north pole [Madec and Imbard, 1996], NEMO uses a tripolar mesh with two north poles on land masses (one on American continental plate, another one on Eurasian plate). These two North poles are foci of a family of ellipses that are considered as latitudes, and the family of curves perpendicular to these "pseudo latitudes" are considered as longitudes (refer to figure 2.7a). The grid type is an Arakawa C-grid (staggered), with a z-coordinate in the vertical direction. Scalar variables are computed at the center of the 3-D grid cells, whereas vector variables at the center of the cell faces (u-velocity and v-velocity

components are diagnosed at the center of the east face, and the center of the north face of a grid cell, respectively), and vorticity at the centers of each of the vertical edges of the cell (refer to figure 2.7(b)). For this work, we used the **A**rctic and **N**orthern **H**emispheric **A**tlantic configuration, in short, **ANHA** (details at https://canadian-nemo-ocean-modelling-forum-community-of-practice.readthedocs.io/en/latest/Institutions/UofA/Configurations/ANHA4/index.html), which is a part of the global ORCA025 mesh [Madec and Imbard, 1996]. The horizontal resolution of ANHA4 is a quarter of a degree (1/4°), which goes from approximately 10 kilometers in Baffin Bay to approximately 20 kilometers in Newfoundland, Labrador Sea area. ANHA4 has 50 levels in the vertical direction, open boundaries at 20°S and across the Bering Strait. Outputs are saved as 5-day averages. ANHA4 has been extensively used in several studies and validated ([Hu et al., 2019], [Pennelly and Myers, 2021], [Deschepper et al., 2023]).

Initial, boundary, and atmospheric conditions

To investigate the impact of different atmospheric conditions, we used two simulations in this study, one existing (from [Marson et al., 2024]) and one new. The atmosphere in the existing simulation was forced by **C**anadian Meteorological Centre's **G**lobal deterministic prediction system **R**e**F**orecasts (CGRF, [Smith et al., 2014]) that provides an hourly dataset for temperature at 2 meters above the surface, wind speed and specific humidity at 10 meters above the surface, incoming shortwave and longwave radiation fluxes, and total precipitation at a horizontal resolution of 1/4° (approximately 33 kilometers), and a vertical resolution of 50 levels. So, we called it **C**GRF **F**orced **A**tmosphere (or **CFA** for short). This simulation CFA started the integration in 2002. **CFA** used **G**lobal **O**cean physical **R**eanal**YS**is (GLORYS2v3, [Masina et al., 2017]) from Copernicus Marine Environment Monitoring Service (CMEMS) by Mercator Océan International for initial conditions. On the other hand, the atmosphere in the new simulation was forced with the **J**apanese **55**-year atmospheric **rea**nalysis (JRA55-do [Tsujino et al., 2018]) with a horizontal resolution of 0.5625°, and a temporal resolution of 3 hours. The temperature and wind speed are both provided at a height of 10 meters by this dataset. So we called it **J**RA-55DO **F**orced **A**tmosphere (or **JFA** for short). This simulation started the integration in 1993. For JFA, the GLORYS12v1 [Jean-Michel et al., 2021] was used for initial conditions. GLORYS12v1 assimilated daily altimetry products to provide hourly data (same as GLORYS2v3) with a finer horizontal resolution of 1/12°,

and 50 vertical levels. For the ANHA4 configuration, this dataset was regridded to the coarser resolution. For the boundary conditions, however, GLORYS2v3 was used for both JFA and CFA simulations at the open boundaries at Bering Strait, and 20° South. For liquid and solid discharges from Greenland, both simulations are forced with [Bamber et al., 2018b] (no solid discharge from Canadian Arctic Archipelago are offered by this dataset), and for river runoff, with HydroGFD [Stadnyk et al., 2021] dataset.

NEMO v3.6 ANHA4 Icebergs simulations	Parameterization	Period of integration	Sea Ice Model	Initial condition	Iceberg initiation	OBC	Atmospheric forcing	Runoff	Output frequency
CFA	ICB sea ice locking	1983-2017	LIM2	GLORYS2v3	No	GLORYS2v3	CGRF	Interannual monthly with Bamber 2018 Greenland with corresponding variables for liquid and solid	5-days
JFA	ICB sea ice locking	2002-2018	LIM2	GLORYS12v1	Yes	GLORYS2v3	JRA55-do	Interannual monthly with Bamber 2018 Greenland with corresponding variables for liquid and solid	5-days

Figure 2.8: Iceberg seasons averaged over six decades: (a) 1960-1969, (b) 1970-1979, (c) 1980-1989, (d) 1990-1999, (e) 2000-2009, and (f) 2010-2019.

Important notes:

(i)In the atmospheric forcing for the simulation JFA, there was no precipitation included. Therefore, the JFA simulation produced unrealistic ocean features driven by the setting of the atmospheric forcing. However, we still used this simulation as an experiment for how different ocean dynamics would alter iceberg occurrence along the east Canadian coast.

(ii) The atmospheric temperature variable was set at different altitudes in the two simulations (2 meters in CFA, and 10 meters in JFA). We need to keep this in mind while comparing the results, and not consider them as a twin experiments. Refer to figure 2.8 for a tabular representation of the two simulations.

Initial iceberg field

The simulation takes a few months to accumulate enough mass in the ten size class "bins" to calve the first particles, so there are fewer icebergs calved in the first years of the CFA simulation, as well as no icebergs in the ocean. This in turn can introduce bias to the seasonality and interannual variability of icebergs reaching 48° N. To address this issue, we initiated the JFA simulation with the final iceberg field from the simulation CFA, which already has the bins partially filled and provides an initial ocean already populated with icebergs.

2.3 Methodology

Factors that might impact iceberg season severity around 48° N

Factors that might dictate iceberg season severity at 48° N were divided into two main types: *local* and *remote*. For the final part of their journey, modelled icebergs drift along the Newfoundland Labrador shelf break (along the magenta line in figure 1.3) off the east coast of Canada and contribute to the season severity. So, in this work, we chose as local factors (environmental conditions along the Labrador coast) that can impact, (i) the sea surface temperature (SST), (ii) the ocean temperature averaged over first 100 meters depth, (iii) and sea ice area. Here, the Labrador shelf mask is defined by the region between 43°N and 61°N, within the first 550 m isobath (refer to the magenta contour in 1.3). The remote factors, in turn, refer to environmental conditions that affect the formation, drift, and deterioration of icebergs farther away from 48°N, such as (i) the sea ice area area for concentrations equal to or larger than 90% in Baffin Bay, and (ii) the calving at different sectors of Greenland (see figure 2.5).
Sea ice extent is defined as the area of a grid cell of the observed data multiplied with number of grid cells that contains sea ice with concentration higher than 0.15 (that is the total area covered by sea ice with concentrations greater than 15%). Whereas, sea ice area is defined as the sum of the sea ice concentration in a grid cell multiplied with the area of the grid cell. As calculating concentration×grid cell area would give us a more accurate value of sea ice condition compared to 1×grid cell area, we chose to analyze sea ice area distribution rather than sea ice extent distribution for both local and remote factors in this study. For Baffin Bay high concentration sea ice analyses, first we eliminated all the concentration values less than 90%. Then we computed the average sea ice of concentration equal or higher than 90% for all winter months over the 43 years (1979 to 2021). Then we grouped those anomalies according to different severity classes (light, moderate, heavy, and extreme). Finally, we averaged these anomalies over different severity classes.

Analyses performed

The time series of the anomalies of environmental conditions mentioned in section 3.1.1 and I48N were compared and assessed using the Pearson correlation

coefficient, as stated in equation 2.4

$$\rho(V, I) = \frac{1}{(N-1)} \sum_{i=1}^{N} (\frac{V_i - \mu_V}{\sigma_V})(\frac{I_i - \mu_I}{\sigma_I}) \tag{2.4}$$

where,
ρ = correlation coefficient of two variables
V = the variable representing local or remote condition
I = I48N data
N = number of observation points in both datasets
μ_V = mean value of the variable V
σ_V = standard deviation of the variable V
μ_I = mean value of I48N data
σ_I = standard deviation of the I48N data
with P-values by default set at < 0.05 for the correlation coefficient to be significant. To evaluate the influence of the observed calving rates on I48N severity, which is an event that lags the former one with a time-gap ranging from a few weeks to a few months, we extracted the typical travel-times taken by the icebergs at different sectors to reach 48° N latitude from the CFA simulation outputs, and established a paradigm for the calving rates to be attributed for a particular year's severity. A schematic for the process in shown in figure 2.9. Also, complete distributions of time that icebergs from different calving regions took in the model to reach 48 ° N latitude is shown in figure 4.3.
The m_map package (Pawlowicz, R., 2020. "M_Map: A mapping package for MATLAB", version 1.4m, [Computer software], available online at `www.eoas.ubc.ca/~rich/map.html`) was used to visualize the spatial distribution of analyzed environmental conditions. The Lambert projection was chosen to minimize the distortion within the region of interest, while preserving the angles between directions.
The yearly iceberg counts from both simulations were broken down using the middle 50% method (table 2.1) explained in section 2.1, into four severity classes (refer to table 3.1).
To simplify the analyses, we defined three size groups for icebergs: large, medium, and small. The icebergs of categories 8 to 10 from the table 2.3 belong to large size class, the icebergs of the categories 4 to 7 belong to medium size class, and finally the icebergs of the categories 1 to 3 belong to small size class.
As mentioned before, NEMO model diagnoses the u and v components of ocean velocity at the center of the side faces of a grid cube. We used these two variables to compute eddy kinetic energy (EKE) at the first layer of model (at 0.5 meters

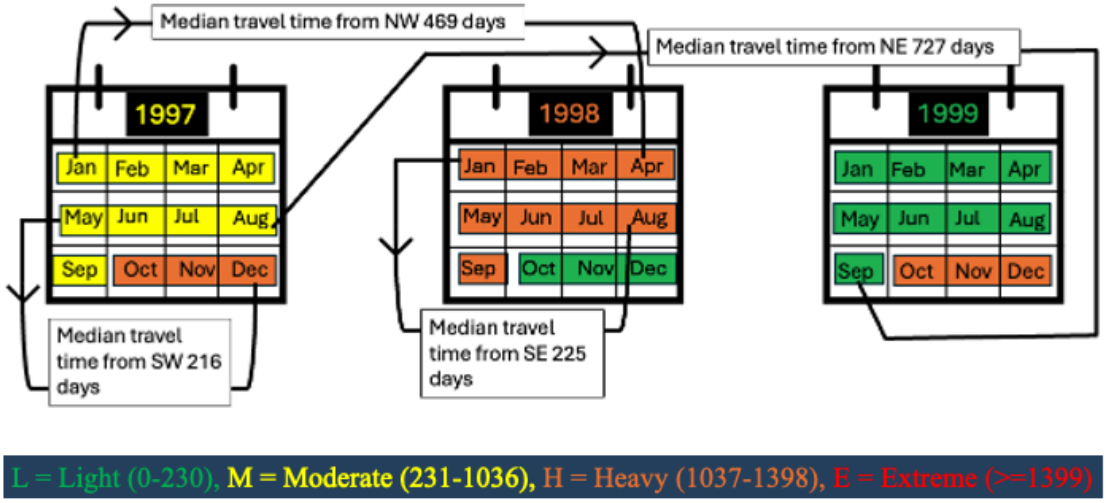

Figure 2.9: Schematic of methodology: Median travel times taken by the icebergs to reach 48° North from calving sectors (2.5) were computed from the model outputs of **CFA**. Years with Light, Moderate, Heavy, and Extreme iceberg seasons are color-coded in green, yellow, orange, and red. Three randomly chosen consecutive years 1997, 1998, and 1999 were moderate, heavy, and light respectively (and 2000 was another heavy year). The median travel time of the icebergs from Northwest sector to 48° North is 469 days (approximately 15 months). So, the calving that happened in January, 1997 from Northwest sector contributes to the I48N in April, 1998. SW, NW, SE, and NE are sectors Southwest, Northwest, Southeast, and Northeast respectively.

depth). To base all the analyses on the same ground, we re-gridded the u-velocity and the v-velocity values to the center of the grid, that is, at the T-grid point (refer to figure 2.7b) before calculating the perturbations to find the EKE.

Chapter 3

Results and discussion

3.1 Observational data analyses

In this section, we will analyze the I48N observed by IIP to establish its seasonal and interannual characteristics. Then, using the ocean temperature from ARMOR3D, sea ice condition from SMMR and SMM/I sensors, and estimated Greenland calving rates from [Bamber et al., 2018a], we will investigate the relationships between the environmental factors potentially determining the severity of the iceberg season along the east Canadian coast and the overall I48N variability.

3.1.1 Characterizing the observed iceberg season

Figure 3.1 shows the the seasonality of iceberg counts observed and recorded by the IIP, averaged over 121 years (from 1901 to 2021). On average (1901-2021) approximately 495 icebergs crossed 48° N latitude line per year. The iceberg season at the Grand Banks starts in February and ends in August. The peak of the season occurs during April in some years, and during May in others (refer to the figure 4.1). Figure 3.2 represents the interannual variation of I48N based on the definition of the IIP iceberg year (previous year's October to current year's September). During the whole period of IIP observations, the highest annual count of icebergs (2204) occurred in the year 1984 (which falls in the current reconnaissance period). The red curly bracket points out the recent decades where the interannual variability increased significantly (IIP annual report 2018, [Rudnickas, Serumgard,]). The standard deviation of I48N for the first 70 years period (1901 to 1970) was approximately 328.97 (variance = 1.082×10^5) with a

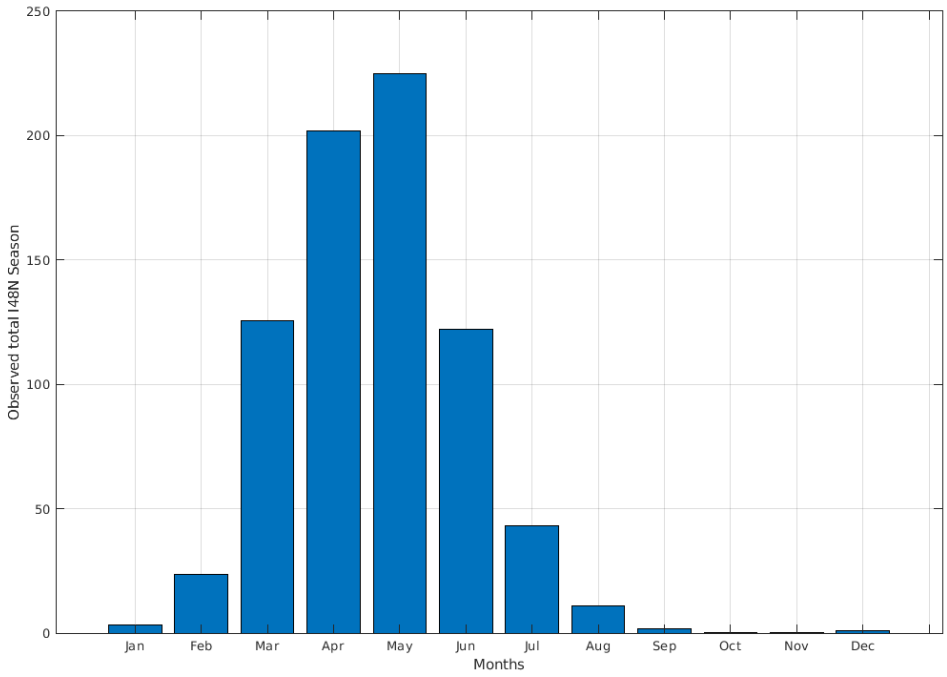

Figure 3.1: The seasonality of iceberg counts observed by IIP to cross 48° N, averaged over the whole period (1900 to 2021) of IIP observation.

range of 1321 (minimum of the period = 0, maximum of the period = 1321). Whereas, the standard deviation of I48N for the rest of the period (1971 to 2021, marked by the red bracket in figure 3.2) was approximately 631.42 (variance = 3.987×10^5) with a range of 2204 (minimum of the period = 0, maximum of the period = 2204). For the three IIP reconnaissance periods, the ranges of monthly iceberg counts for all four severity classes are shown in figure 3.3, along with the monthly means for each class. A non-negligible influx of icebergs in months outside of the defined season increases from the early reconnaissance period to the later ones. For example, the maximum number of icebergs crossing 48° N latitude in January increased from less than 20 to more than 100. In the middle row of figure 3.3, a peak in one month followed closely by another month is observed for all the severity classes (1946 to 1982). The bottom plot of figure 3.3 for the reconnaissance period 1983 to current time, however, shows larger overlapping among the monthly ranges of the iceberg fluxes across severity

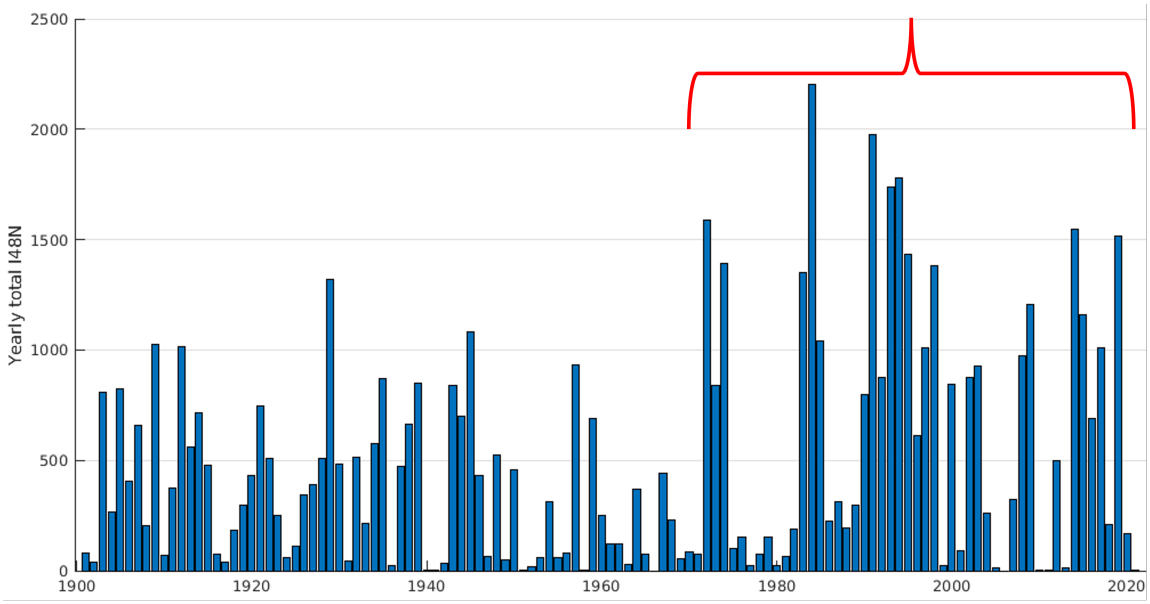

Figure 3.2: The yearly total iceberg counts observed by IIP to cross 48° N in an iceberg year. The red curly bracket points out the time period when the interannual variability increased. 12 lightly (with a standard deviation of approximately 93.10 icebergs), 15 moderately (with a standard deviation of approximately 280.55 icebergs), 4 heavily (with a standard deviation of approximately 140.07 icebergs), and 8 extremely (with a standard deviation of approximately 290.03 icebergs) severe years were observed for the current reconnaissance period (1983 to date). Out of 38 years, 15 fell in the middle 50% of the I48N distribution, while 12 years belonged the range below that, 4 belonged to the range of 10% above it, and finally 8 years fell into the range above 85% of the distribution. (For middle 50% method, refer to explanation in chapter 2, and figure 2.2).

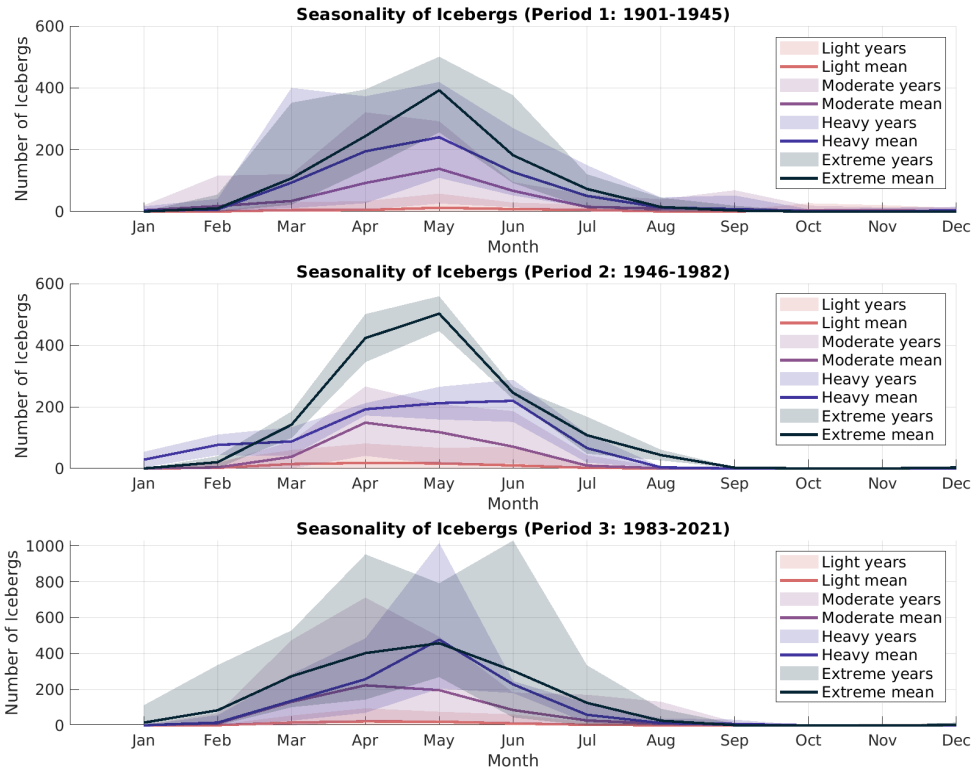

Figure 3.3: The monthly I48N distribution across different severity classes during the three IIP reconnaissance periods. The pink, purple, dark blue, and dark green lines indicate the monthly average of iceberg counts south of 48° N over the light, moderate, heavy, and extreme iceberg severity years of the corresponding periods. The shaded areas with same colors represent the monthly ranges of the iceberg counts (i.e. the difference between the highest count of icebergs and the lowest count of icebergs in each month).

classes. For example, in April I48N ranged from approximately 150-900 during extreme years, from approximately 50-500 during heavy years, and from 50 to 700 during moderate years etc. In the extreme severity class, we see icebergs crossing 48° N southward in larger number (more than 1000) in April and June, compared to the previous periods (500 to 600). This could indicate that the season has widened in the recent reconnaissance period. However, as these numbers are not normalized using the methods described in chapter 2, it could also be a result of

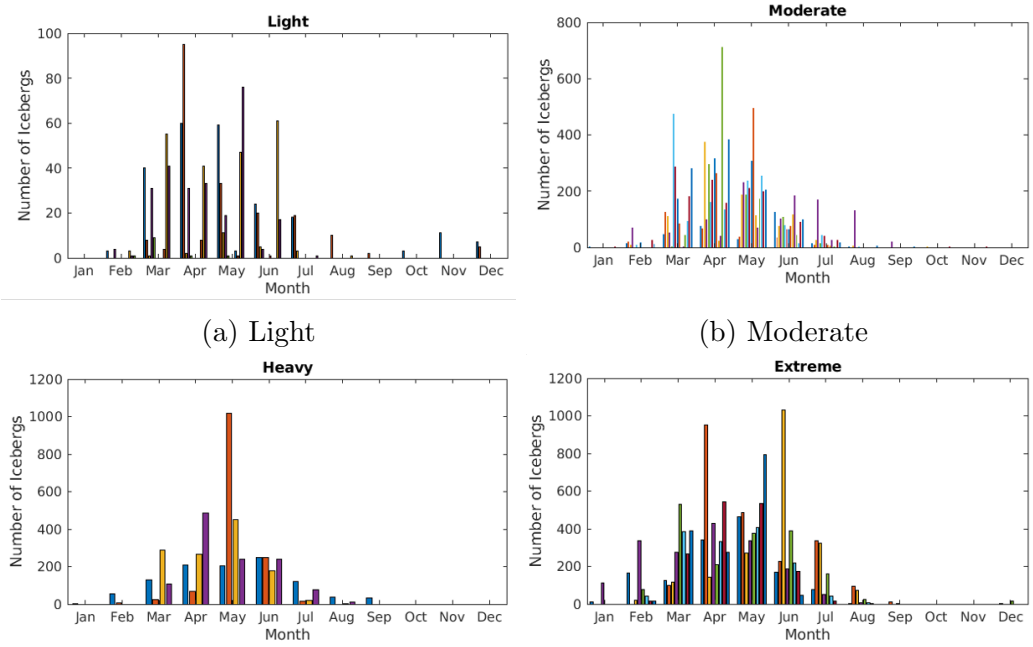

(a) Light (b) Moderate

(c) Heavy (d) Extreme

Figure 3.4: The observed iceberg count crossing 48° N latitude line is shown for (a) light, (b) moderate, (c) heavy, and (d) extreme iceberg seasons on the east coast of Canada. Each color in a subplot stands for a particular year that belongs to the corresponding severity class. There were 12 lightly (with a standard deviation of approximately 93.10 icebergs), 15 moderately (with a standard deviation of approximately 280.55 icebergs), 4 heavily (with a standard deviation of approximately 140.07 icebergs), and 8 extremely (with a standard deviation of approximately 290.03 icebergs) severe years observed for the current reconnaissance period until 2021. That is out of 38 years, 15 fell in the middle 50% of the I48N distribution, while 12 years belonged the range below that, 4 belonged to the 10% above it, and finally 8 years fell into the range above 85% of the distribution.

the advancement in the detection methods of IIP. The four subplots in figure 3.4 show all the years of the current IIP reconnaissance period (since 1983) into four severity categories. Each color in a subplot stands for a particular year that belongs to the corresponding severity class. There were 12 lightly (with a standard deviation of approximately 93.10 icebergs), 15 moderately (with a standard deviation of approximately 280.55 icebergs), 4 heavily (with a standard deviation of approximately 140.07 icebergs), and 8 extremely (with a standard

deviation of approximately 290.03 icebergs) severe years observed for the current reconnaissance period until 2021. That is out of 38 years, 15 fell in the middle 50% of the I48N distribution, while 12 years belonged the range below that, 4 belonged to the 10% above it, and finally 8 years fell into the range above 85% of the distribution. The iceberg count distributions for heavy seasons seem to agree with the general definition of iceberg season off the east coast of Canada the most (season starting in February, ending in August, peak in April or May, figure 3.4c). Extreme iceberg seasons (figure 3.4d) have a reasonably large number (100 to 300) of icebergs crossing 48° N outside of the typical peak months. This suggests that extreme iceberg seasons are caused by a higher number of icebergs crossing 48° N throughout the year rather than by a higher count in early spring. In other words, the difference between heavy and extreme years is not pronounced in the peak of the curve, but the area below it. Which, in turn, indicates that not only the ocean condition along Labrador coast during the months of spring, but also the upstream environmental conditions during the winter and autumn months prior to the season could play key roles in determining the severity of the season.

3.1.2 Characterizing relationships between I48N and environmental conditions

As described in chapter 1, former studies reported that the iceberg season in the east Canadian coast is influenced by local and remote oceanic and atmospheric conditions, as well as by glacial discharges. To investigate the influence of those factors on iceberg counts at the Grand Banks, we assessed their relationships in interannual time scales.

3.1.2.1. Local conditions

Ocean temperature on the Labrador coast

As the icebergs populate the Labrador coast mostly during spring months, we analyzed ARMOR-3D ocean temperature for April, May, and June over the Labrador shelf mask. Figure 3.5a shows that the observed SST anomaly time series over the Labrador shelf mask averaged over only spring months exhibits a rather statistically significant ($p = 1.1 \times 10^{-3}$) correlation ($r = -0.58$) with the I48N timeseries. This result suggests that a higher ocean surface temperature along their path melts the icebergs before they reach the Grand Banks region, whereas a cooler ocean surface helps them survive longer and travel further south. In other words, the warmer the Labrador coast, the lighter is the severity

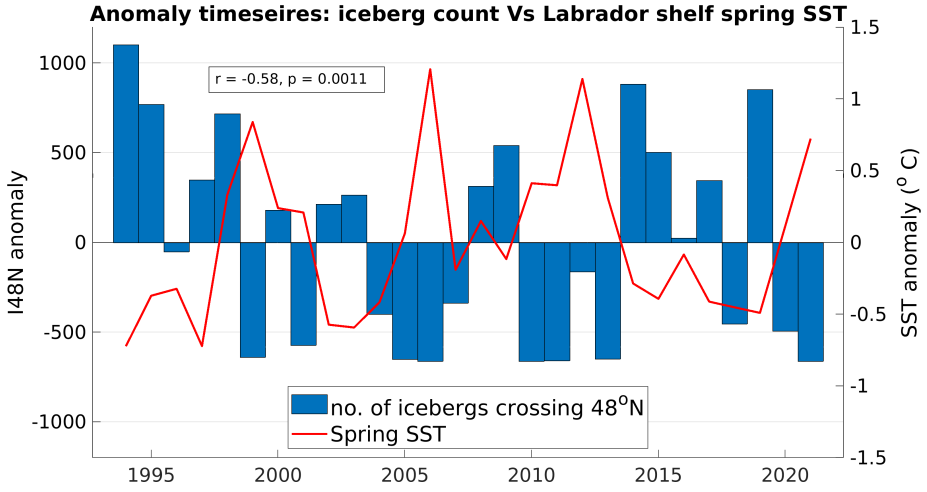

(a)

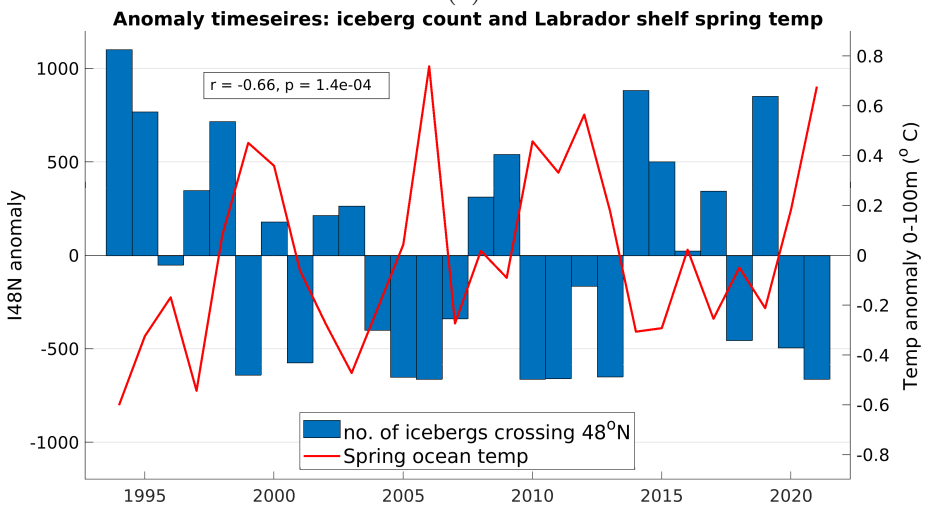

(b)

Figure 3.5: Anomaly of yearly (October to September) total number of icebergs crossing 48° N (blue bar) with (a) the anomaly in SST (in °C, red line), and (b) the anomaly in temperature (in °C, red line) averaged over the upper 100 meters of ocean over the Labrador shelf mask (region shown in figure 1.3).

of the observed iceberg season along the east coast of Canada. However, despite the significant correlation between I48N and SST, one should consider that icebergs are not only interacting with surface waters. [Cyr and Galbraith, 2021] found no significant (with p-value < 0.05) correlation between I48N and SST , while a significant correlation between I48N and the bottom temperature (from mooring arrays deployed in different sectors of the Labrador shelf) averaged over all the ice-free months. Moreover, [Kubat et al., 2005] found that an iceberg model provides more accurate drift prediction by using depth-integrated ocean field. In the model study [Marson et al., 2018] I48N seasonality representation showed improvement when the ocean variables were considered along the keel of the modelled icebergs. Therefore, we propose that the ocean temperature averaged over the draft length of the icebergs would provide a more accurate connection with the I48N. [Barker and Carrieres, 2004] showed that depth reached by icebergs along the east Canadian coast is approximately 40 m to 120 m. Therefore, we averaged the temperature of upper 100 m of the ocean along the Labrador shelf mask (for definition of Labrador shelf mask refer to 1.3) to analyze the correlations between observed I48N and the observed ocean temperature. Indeed, figure 3.5b shows that the temperature anomaly from surface to 100 m over the Labrador region in spring months taken from ARMOR-3D is even better correlated ($r = -0.66$, $p = 1.4 \times 10^{-4}$) with the I48N anomaly in comparison with spring SST anomaly from the same data source. During the periods of negative I48N anomalies (for example, 2010 to 2014, or 2018) the depth-integrated ocean temperature mirrors the light severity years better than the SST anomaly. Figure 3.6 represents the spatial distribution of the average deviation of the spring months temperature from the mean (1994 to 2021) spring months temperature averaged over the upper 100 m of ocean. We see a noticeable positive anomaly of 0.5 to 1.5 °C in lightly compared to heavily severe iceberg seasons especially along the northern part of Labrador coast. This reinforces the hypothesis that iceberg presence in this region is modulated by local ocean temperature conditions.

Sea ice condition on the Labrador coast

Figure 3.7 shows the timeseries of the anomalies of I48N and winter sea ice area over the Labrador shelf mask. The total sea ice covered area averaged over the winter months (1995 to 2021) has a high positive correlation value ($r = 0.78$, $p = 1.64 \times 10^{-6}$) with observed I48N anomaly. We see a prominent resemblance between the two anomalies especially during the light and the extreme iceberg

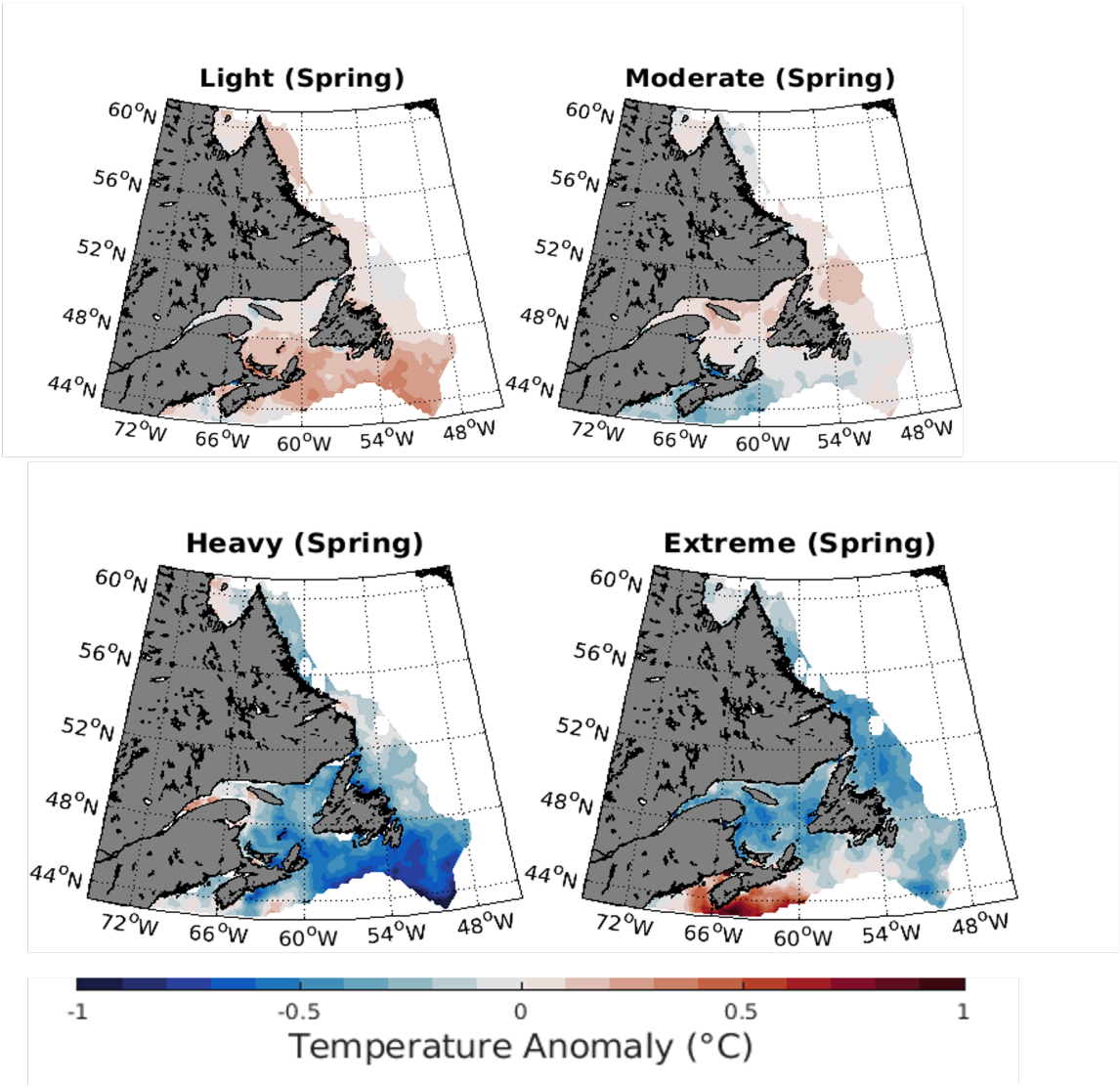

Figure 3.6: Observed spring depth-averaged (0-100 meters) ocean temperature anomaly over the Labrador shelf mask across different iceberg seasons. Headers Light, Moderate, Heavy, and Extreme show the average difference between depth-averaged spring temperature over light, moderate, heavy, and extreme iceberg years respectively and mean spring (April to June) temperature, averaged over the years 1994 to 2021.

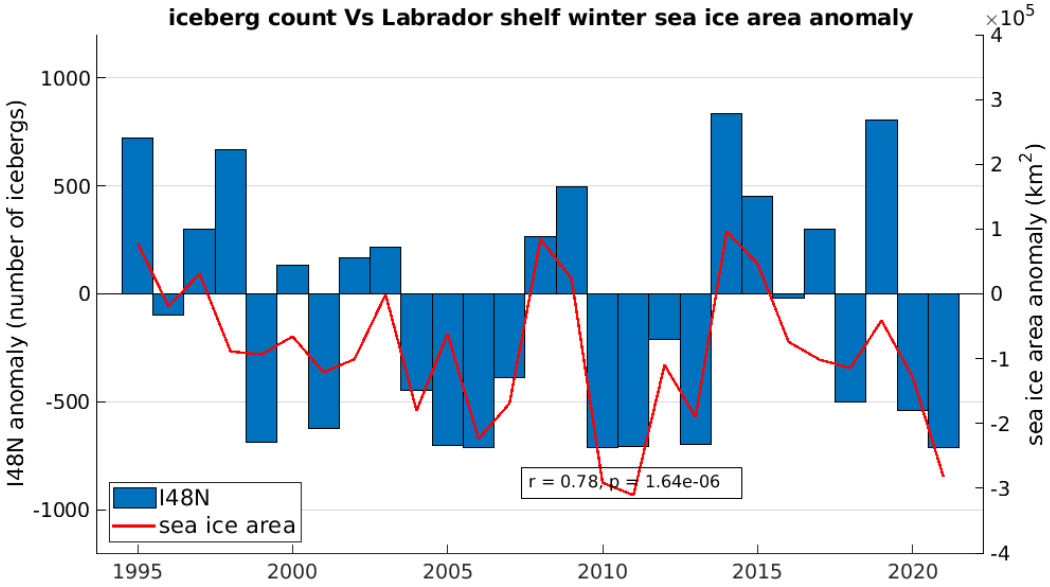

Figure 3.7: Anomaly of yearly (October to September) total number of icebergs crossing 48° N, averaged over the time period 1995 to 2021 (blue bar) with the anomaly in area over Labrador shelf mask covered with sea ice during the winter months (January to March) in the years 1995 to 2021).

years. In [Cyr and Galbraith, 2021] the seasonal maximum sea ice extent off East Canada was found to have a significant, although lower correlation (0.66, p-value < 0.05) with I48N. The inclusion of Labrador shelf sea ice condition during the late fall months in [Cyr and Galbraith, 2021] can be a reason behind this difference.

[Marko et al., 1994] and [Marko et al., 2014] suggested that the sea ice coverage over the Labrador shelf region impacts the iceberg season severity. For example, an extensive sea ice cover in the northern Labrador coast during winter promotes iceberg survival, since it is associated with lower than average ocean temperatures and attenuated waves. [Marko et al., 1994] used sea ice and iceberg count observations for the years 1963 through 1991 and found the existence of a bilinear correlation (refer to figure 1.5) between the annual iceberg count and the 15th April sea ice extent (with thickness > 30 cm) off the south Labrador and Newfoundland region (from 55° N to 47° N). Here, instead of using only a daily value (April 15th) to represent sea ice conditions over the entire iceberg season, we use the winter sea ice area over the Labrador shelf mask (from 62° N to 48°

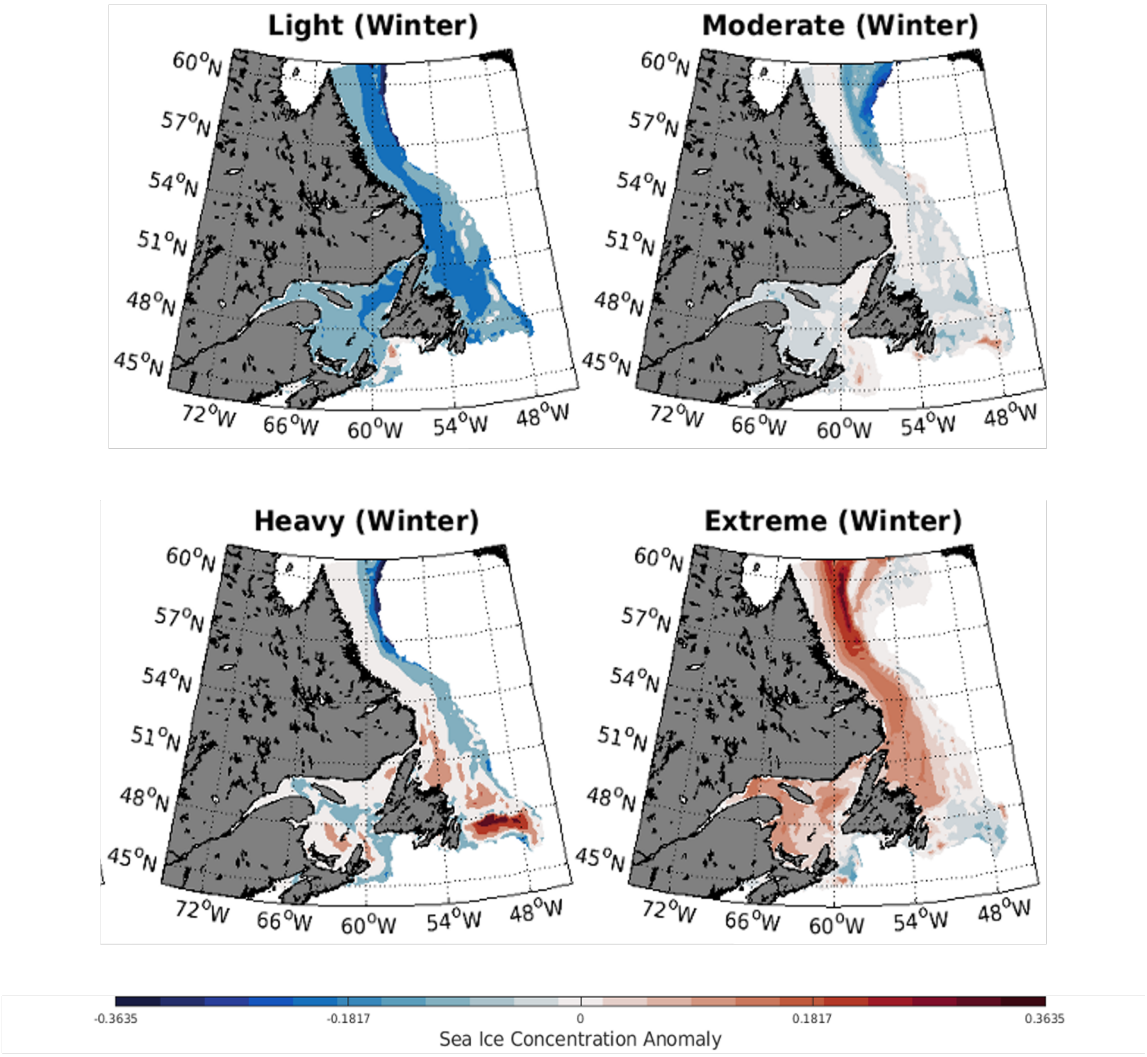

Figure 3.8: Observed winter sea ice concentration anomaly over Labrador shelf mask across severity classes. Light, Moderate, Heavy, and Extreme show the anomaly of sea ice concentration ($\geq$ 15%) over light, moderate, heavy, and extreme iceberg years, respectively, with respect to the average (1995-2021) sea ice concentration from January to March sea ice concentration, averaged over the years 1995 to 2021.

N) to establish its influence on the season severity. Compared to **winter** Labrador sea ice area, the variability in the **spring** Labrador sea ice area shares a (statistically significant) lower correlation value ($r = 0.71$, $p = 3.24 \times 10^{-5}$) with the I48N anomaly. Therefore, the variability in the local *winter* sea ice area might have an even bigger impact on the upcoming iceberg season severity compared to the *spring* sea ice area.

We further investigated the spatial distributions of the winter sea ice concentration anomaly over the whole Labrador shelf region for 1994 to 2021. The maps in figure 3.8 show that during heavier(lighter) iceberg severity years, the Labrador shelf mask was more(less) covered by sea ice than the mean winter sea ice area averaged over those 27 years. This suggests that, the more the Labrador coast is covered with sea ice in winter, the more severe the upcoming iceberg season is going to be. The timing of the sea ice retreat might also influence the onset of the iceberg season on the east coast of Canada, and should be further evaluated.

3.1.2.2. Remote conditions

Sea ice condition in Baffin Bay

In this study we found that, a large percentage (69 to 77, figure 4.7) of I48N comes from the glaciers of the western Greenland. I48N can reasonably approximate the iceberg discharge from the calving sites along the west Greenland coast ([Zhao et al., 2016]). Therefore, while considering the remote factors determining the severity of the iceberg season on the east Canadian waters, we analyzed the oceanic conditions in Baffin Bay and its connection with the I48N. The breaking of the sea ice at the Baffin Island shelf break influences the release of the entrapped icebergs into the offshore branch of the Labrador current that carries them to the Grand Banks ([Marko et al., 2014]). That is, the sea ice concentration off the Baffin Island coast determines the entrapment/smooth passage of the icebergs, and in turn impacts their deterioration rate and their arrival at Newfoundland region. Furthermore, when sea ice concentration and thickness are high in Baffin Bay, icebergs move southward as one with the sea ice pack ([Marson et al., 2024]). Therefore, the sea ice condition in Baffin Bay may have a significant impact on the I48N variability, which we evaluate next.

Figure 3.9 shows the time series of the IIP-observed yearly total iceberg counts from the year 1979 to 2021 (blue bars), plotted with the area covered by sea ice with concentration equal or more than 90% during winter months of the same

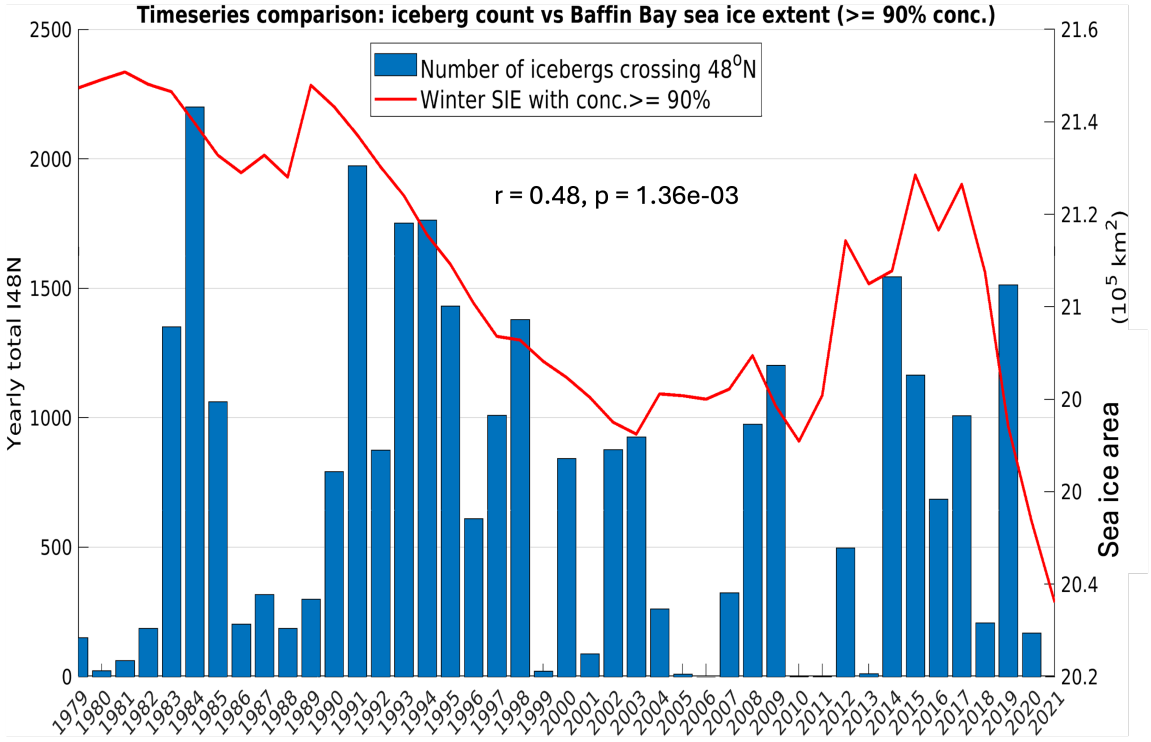

Figure 3.9: The timeseries of the observed yearly total iceberg counts (blue bars) with the observed total area of Baffin Bay covered with high concentration sea ice ($\geq$ 90%) during the winter months (January to March).

period. The I48N shares a statistically significant positive correlation (r = 0.48, p = 1.36×10^{-3}) with the winter sea ice area of high concentration over the entire Baffin Bay. This correlation is lower compared to the correlation between anomalies in I48N and sea ice cover over Labrador coast, may be because: (i) not all the icebergs contributing to I48N encounter the sea ice over Baffin Bay, while most of them do interact with the sea ice area covered Labrador coast; and (ii) Baffin Bay has a bigger area than the Labrador region, which might add bias to the result, (iii) the distance between Baffin Bay and Grand Banks is much larger than that between Labrador region and Grand Banks, which means other environmental factors would modify the presence of the icebergs, lowering the weightage of the impact of the oceanic condition in Baffin Bay on the variability of I48N. For instance, the icebergs' trajectories inside Baffin Bay, and hence the impact of the sea ice on their movement, could vary based on their calving locations and time. For example, the icebergs calved from the northwest sector of

Greenland in the month of February would encounter high sea ice concentration in this part of Baffin Bay. On the other hand, icebergs calved from the same location but in the month of July, or from the southwest sector in the month of February will not experience a very heavy sea ice condition en route. Due to this broad spatial and temporal variation of Baffin Bay sea ice, biases might be instilled in the analyses. To investigate the variation of high concentration winter sea ice over Baffin Bay across the different iceberg severity seasons, we analyzed the spatial distribution of sea ice with anomaly (average deviation from 1979-2021 mean values) of winter concentrations equal to or higher than 90%. The subplots of Figure 3.10 show the spatial distribution of the anomalies described above. We see that even within a very narrow range of variability (± 0.02), a noticeable difference in the concentrations across the severity classes is observed over Baffin Bay. During the winter months of lightly and moderately severe iceberg seasons (figure 3.10a, and 3.10b), less of Baffin Bay shows high concentration of sea ice than it showed during the winter months of heavily severe iceberg seasons (figure 3.10c, and 3.10d). The noticeable differences at the edges of the sea ice around the central to southeast edge of Baffin Bay implies that the ice pack concentration in that region might have an impact on the survival of the icebergs past Davis Strait. This finding supports the hypothesis made in [Marko et al., 2014] that the higher the sea ice concentration in Davis Strait, the more icebergs will endure through early deterioration and will survive long enough to drift further southward. Moreover, as the east limb of the Baffin Bay cyclonic gyre delivers some of the icebergs from west and northwest Greenland sources to the BIC, the sea ice conditions in the North Water polynya might also impact the iceberg survival past Smith Sound (refer to figure 1.2). The higher the sea ice concentration in the above-mentioned area is, the more likely it is that icebergs would make it to the Baffin Island Current (BIC) in larger numbers. This hypothesis of I48N's sensitivity towards sea ice conditions at different spots of Baffin Bay could be a subject of future investigation using models. Finally, we see a very small range of anomaly (-0.002 to 0.002) of sea ice concentration along the Baffin Island coast. However, the trajectories of the icebergs from further north calving sites over the West coast of Greenland could also be impacted by the high concentration sea ice anomaly in this region. A model study of trajectories could reveal further information about it. [Marko et al., 1994], 2014) argued that the longer the icebergs are entrapped in sea ice in that region, the longer their lifetime, which impacts the iceberg season severity. The observed anomalies we found along the Baffin Island coast are too small to make any conclusions about that.

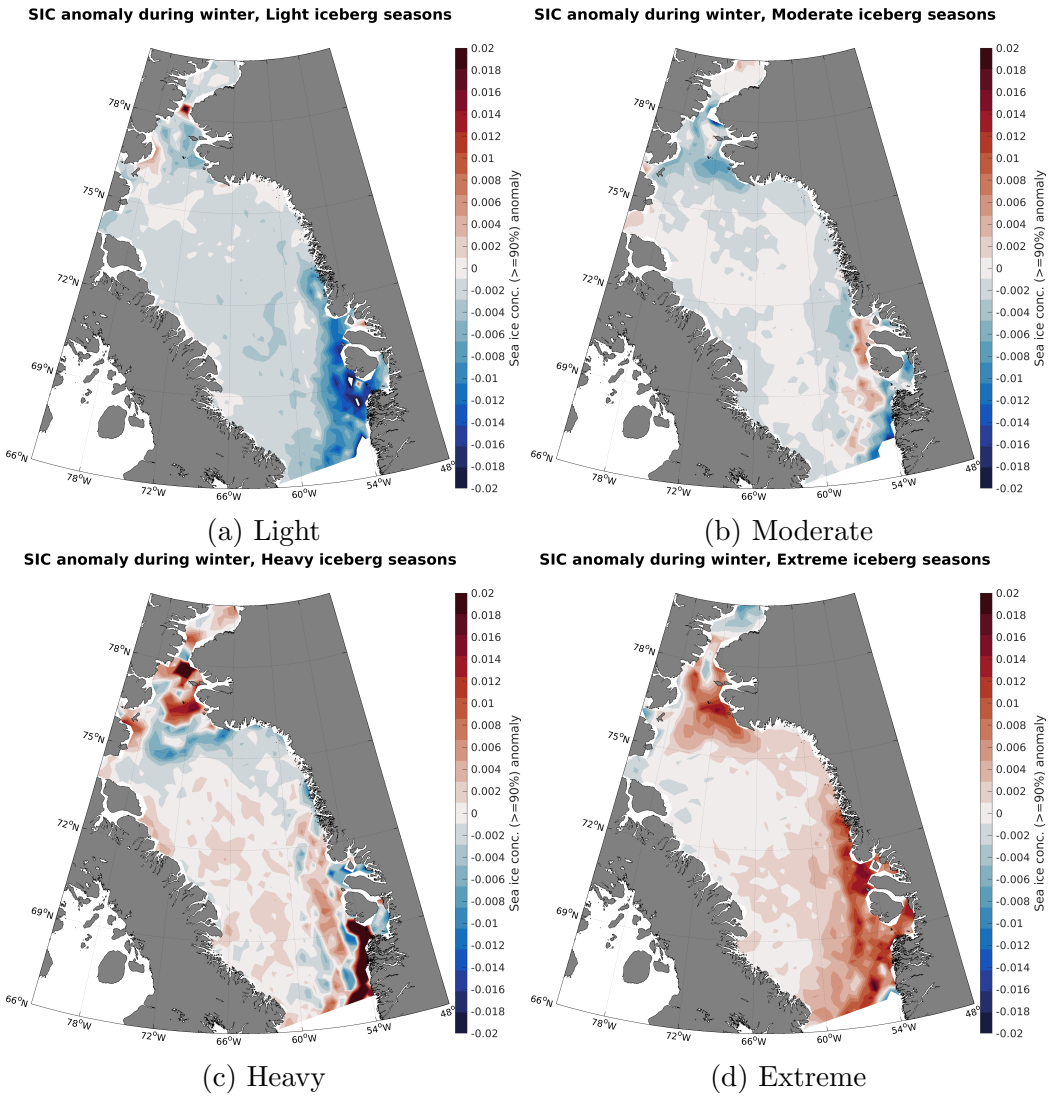

(a) Light (b) Moderate

(c) Heavy (d) Extreme

Figure 3.10: The observed winter sea ice concentration anomalies (computed from averaged winter high concentration sea ice, i.e. $\geq 90\%$) is shown for (a) light, (b) moderate, (c) heavy, and (d) extreme iceberg seasons on the East Canadian coast.

Moreover, readers should note the differences in the methodologies. For example, in [Marko et al., 1994] and [Marko et al., 2014], the authors used the climatological average of sea ice concentration (with thickness above 30 cm) on January 1st, from the data with an average resolution of 2 kilometers, whereas in this study a monthly sea ice data with a coarser resolution (10 to 16 kilometers in Baffin Bay) with a concentration equal or higher than 90% was used (details in chapter 2).

Greenland calving

To explore the possible influence of iceberg calving from Greenland tidewater glaciers on the interannual variability of I48N, we compared the timeseries of observed I48N with the timeseries of estimated calving distributions (expressed in Gigatons/year) from [Bamber et al., 2018b]. For the periods of 1958-2016 and 1994-2016, no significant correlations were found (not shown in figures). The annual calving rates from all the sectors, however, showed a similar upward trend through years, which might have affected the correlations with the I48N. So, we removed the trend and calculated the correlations again. Only the North sector's detrended calving rates were found to have statistically significant positive correlation (r-value = 0.4299) with I48N. A positive correlation means that the more icebergs calved from a sector, the heavier the next iceberg season will be. As elaborated in chapter 2, we analyzed the distribution of time taken by the modelled icebergs from different sectors to reach 48° N, and lagged the [Bamber et al., 2018a] calving rate time series from corresponding sectors by that (median) amount of time (refer to 4.3) prior to the observed I48N to analyze their relationship to the severity of the iceberg season (figure 3.12). Each of the boxplots in figure 3.12 represents the potential contribution of lagged solid discharges (in Gigatons/year) coming from the corresponding sector to I48N falling in different severity categories. For example, the leftmost box in Figure 3.13(a) shows the relationship between the solid discharge from the southeast and I48N light seasons that are 225 days (the modelled median iceberg travel time between Southeast Greenland and 48° N; see figure 4.3) apart. One would expect that the lighter iceberg seasons would be associated with lower calving rates, compared to the heavier iceberg seasons. But this linear response cannot be seen in Figure 3.13. For example, typical calving rates associated with extreme seasons are almost at the same level with light seasons or lower. This finding does not support the claims made in [Bigg et al., 2014] that the calving rates at Greenland's major tidewater glaciers, especially from the northwest sector

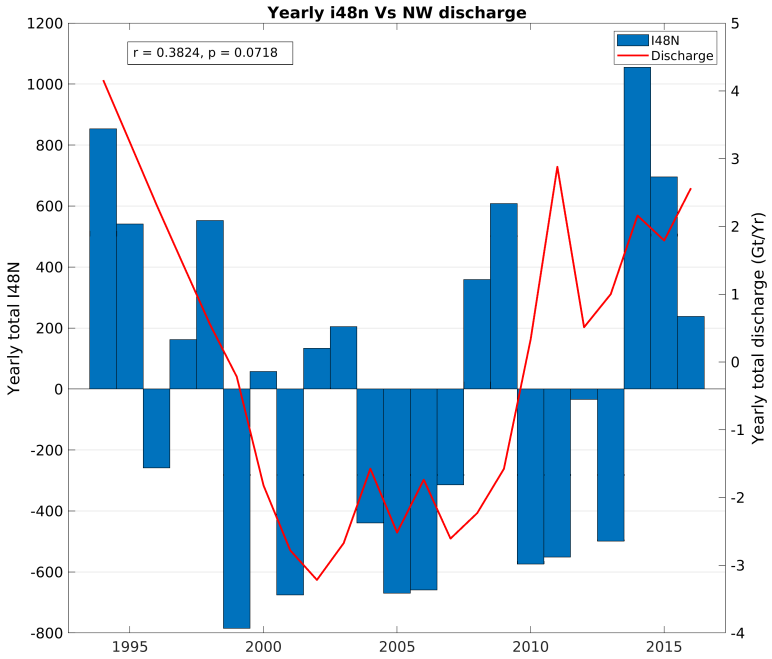

(a) Northwest Greenland

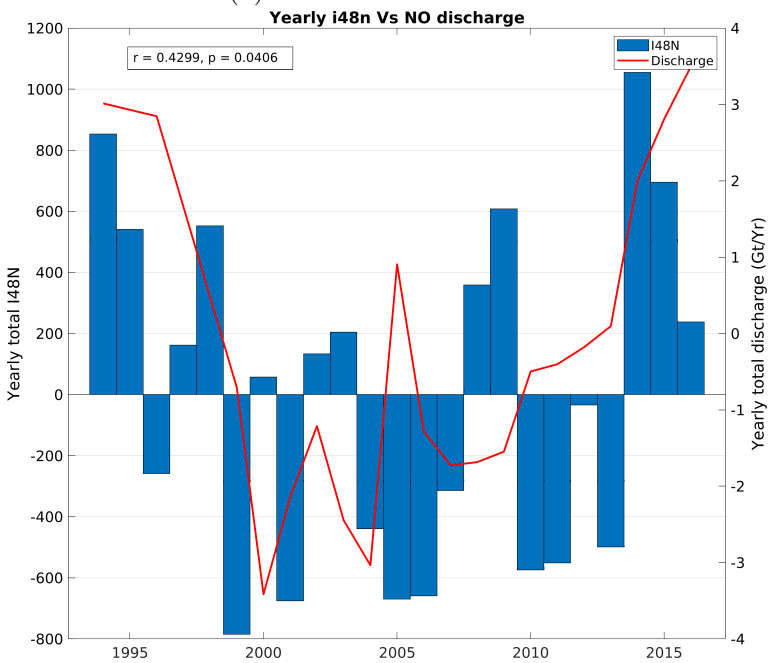

(b) North Greenland

Figure 3.11: Observed anomaly of yearly (October to September) total number of icebergs crossing 48° N, averaged over the time period 1900 to 2021 (blue bar) with the anomaly in solid discharge (in kg/year, red line) from (a) the northwest and (b) the north sectors of Greenland.

determine I48N severity.
[Wilton et al., 2015] studied how the most important contributing origins of icebergs reaching the Newfoundland and Labrador shift from the glacial outlets over southwestern Greenland during the first third of twentieth century to the glacial outlets over central to northwestern Greenland during the later decades, using an ocean-iceberg coupled model. For this study, they used a coarse and a fine resolution model to compute the percentage of modelled I48N contributed by the models' iceberg discharge from different sectors of Greenland. In the finer resolution model (0.25°) the icebergs with north to northwest Greenland origin contribute the most in I48N fluctuation during first three decades of last century. So, we hypothesized that some of these major contributing calving sectors could influence the I48N interannual variability, in turn determine the severity of the iceberg season. However, this contrast in findings could root from the differences in the definitions and/or from the methods chosen for analyses. For example, using sensitivity experiments, [Bigg et al., 2014] showed that while a model with constant calving rate would not reproduce any of the observed I48N variability (even with atmospheric and oceanic conditions varying interannually), a model with a calving rate varying in a similar manner to the I48N would "retain the signal" in the modelled I48N. The complexity of surface velocity distributions across different glaciers is over-simplified with one specific latitude. On the other hand, in this study we used the dataset from [Bamber et al., 2018a] that defined the monthly solid discharge as a product of the surface velocity of the glacier at a given location and its gate area. Therefore, this dataset incorporates both the spatial complexity and temporal variability of calving. Another difference, the connections between the solid discharge and the I48N were established with a constant time-lapse (8 month gap). Here, we used the time that icebergs take to arrive at 48° N from different sectors. For example the January 1997 calving from Northwest sector of Greenland contributes to the April 1998 iceberg counts, as the median number of days taken by the icebergs from the above-mentioned sector to reach Grand Banks is 469. Here we used a very simplified method to derive the travel times from the NEMO model (CFA) outputs. As we can see, either the covariances of the travel times from majority of the sectors, except for the Northwest and Central West are too high, or the size of the dataset (the number of particles reaching 48° N form the sector) is too low, this simplicity can be a source of limitations. This analyses can also have biases from the source of uncertainty in the model. For example, the model does not account for the grounding time of icebergs, nor it resolve the fjords and therefore does not represent any possible time-lapse between the breaking of the icebergs and their

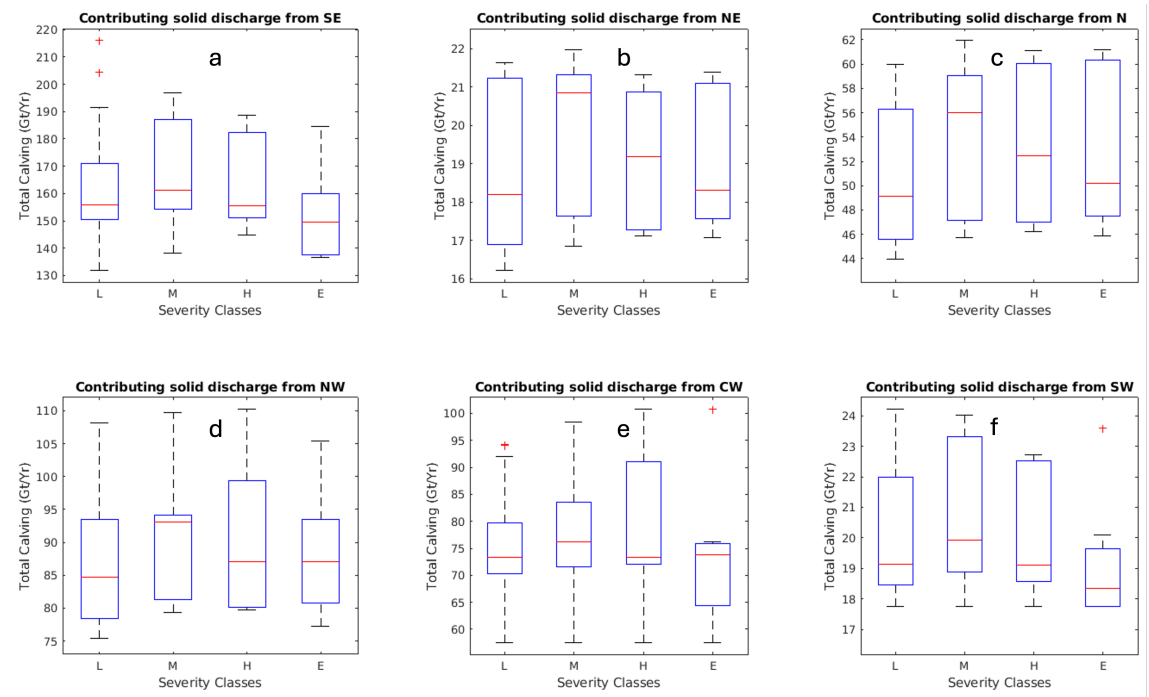

Figure 3.12: The statistical distribution of yearly total solid discharges from six calving sectors (refer to figure 2.5) of Greenland. The boxplots distribution of solid discharge from the sectors Southeast, Northeast, North, Northwest, Central West, and Southwest are shown in the subfigures left top row, middle top row, right top row, left bottom row, middle bottom row, and right bottom row respectively 225, 727, 615, 469, 600, and 216 days prior to the icebergs seasons categorized as light (first boxplot), moderate (second boxplot), heavy (third boxplot), and extreme (fourth boxplot).

entering into the ocean.

The time evolution of the correlations

The importance of different factors in the determination of the iceberg season severity along the east coast of Canada changes from one period to another [Marko et al., 2014] . For example, the I48N-Davis Strait January sea ice extent correlation dropped from 0.642 in 1980-1997 to 0.11 in 1998-2014, while the I48N-Labrador sea ice extent correlation increased from 0.352 in 1980-1997 to 0.456 in 1998-2014. Curious how all the observed correlations respond to different time periods, we investigated the temporal evolution of the correlations of I48N with all the variables (figure 3.13). The time series of I48N was correlated with Labrador shelf winter SST (sstWinterTS), Labrador shelf spring SST (sstSpringTS), 100 m depth averaged spring ocean temperature over Labrador shelf (T100mSpringTS), 100 m depth averaged winter ocean temperature over Labrador shelf (T100mWinterTS) for the periods 1993-2021, 1994-2021, 1995-2021 and so on, upto the period 2010-2021. And the time series of I48N was correlated with winter sea ice area over Labrador shelf (LSsiaWinter), and Baffin Bay high concentration winter sea ice area (siaWinterTS) for the periods 1980-2021, 1981-2021, 1982-2021 and so on, upto the period 2010-2021. The observed correlation between I48N and spring SST is more or less steady with time, whereas I48N's correlation with winter SST, spring dept-averaged temperature, and winter dept-averaged temperature over Labrador shelf depleted as the period narrowed to more recent years. However, the correlations of I48N with both Labrador shelf sea ice and Baffin Bay high concentration sea ice decreased and were steady (approximately 0.7 and 0.3 respectively) for the period 1995-2021 up to the period 2005-2021. The figure 3.14 represents the corresponding statistically significant (i.e. with p-value ≤ 0.05) correlation values for the periods discussed above. The negative correlations are color coded as blue, whereas the the positive correlations as red. We see that after the year 1993, the Baffin Bay high concentration sea ice did not have significant correlation with I48N. This agrees with the hypothesis proposed in [Marko et al., 2014] that the relationships of I48N with its determining factors are changing with time.

A general increase in the highly concentrated sea ice covered area is noticed for the years with severity in the heavy and extreme categories, whereas for the years with lighter season severity, the sea ice covered area showed lower values during the period of 1979 to 2000 (with a correlation value $r = 0.50$, $p = 1.96 \times 10^{-2}$ for this period). This indicates that during that time period, a more extensive sea

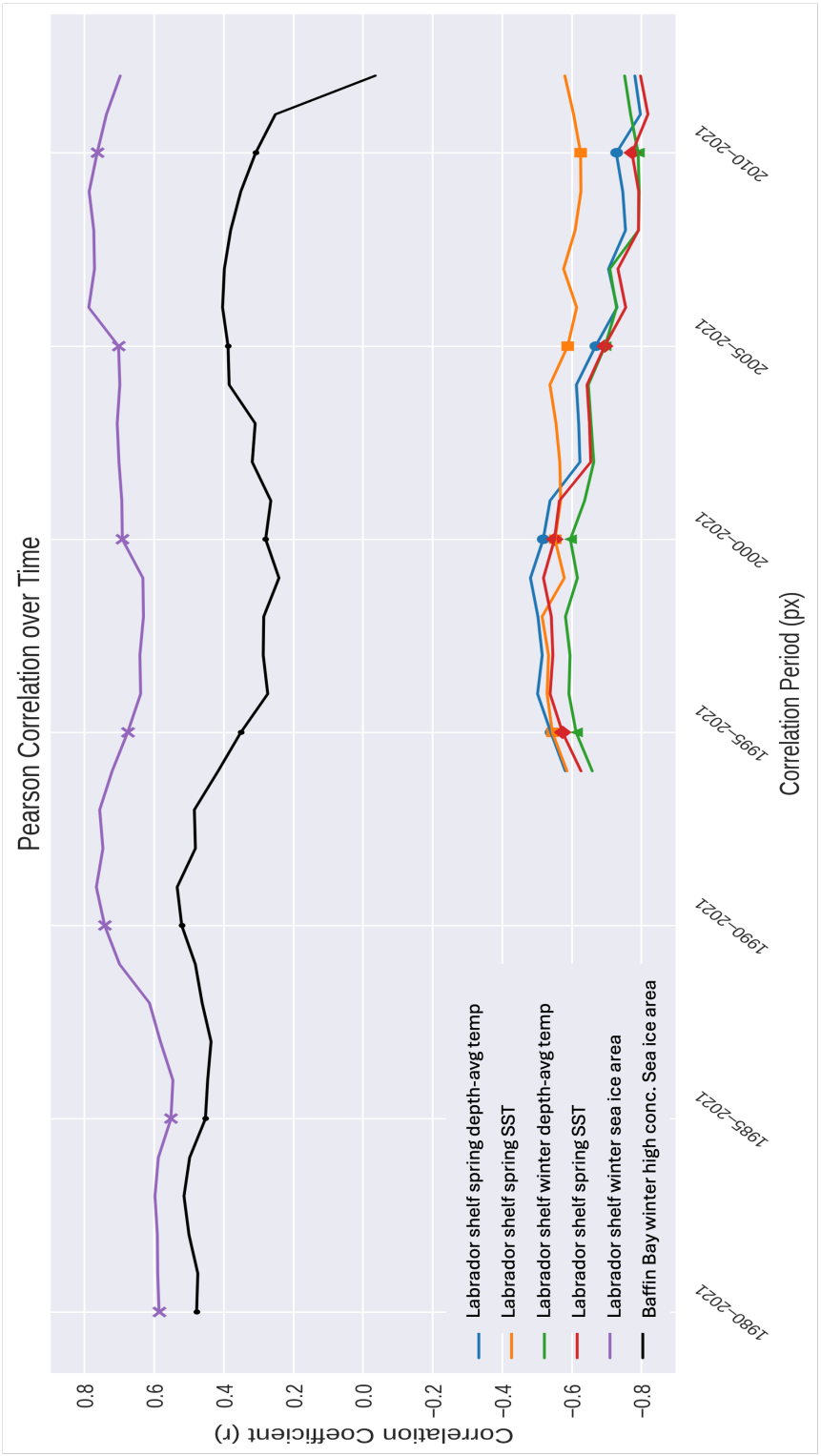

Figure 3.13: The observed time evolution of the correlations between the environmental factors and I48N for Labrador shelf winter SST (sstWinterTS), Labrador shelf spring SST (sstSpringTS), 100 m depth averaged spring ocean temperature over Labrador shelf (T100mSpringTS), 100 m depth averaged winter ocean temperature over Labrador shelf (T100mWinterTS), winter sea ice area over Labrador shelf (LSsiaWinter), and Baffin Bay high concentration winter sea ice area (siaWinterTS).

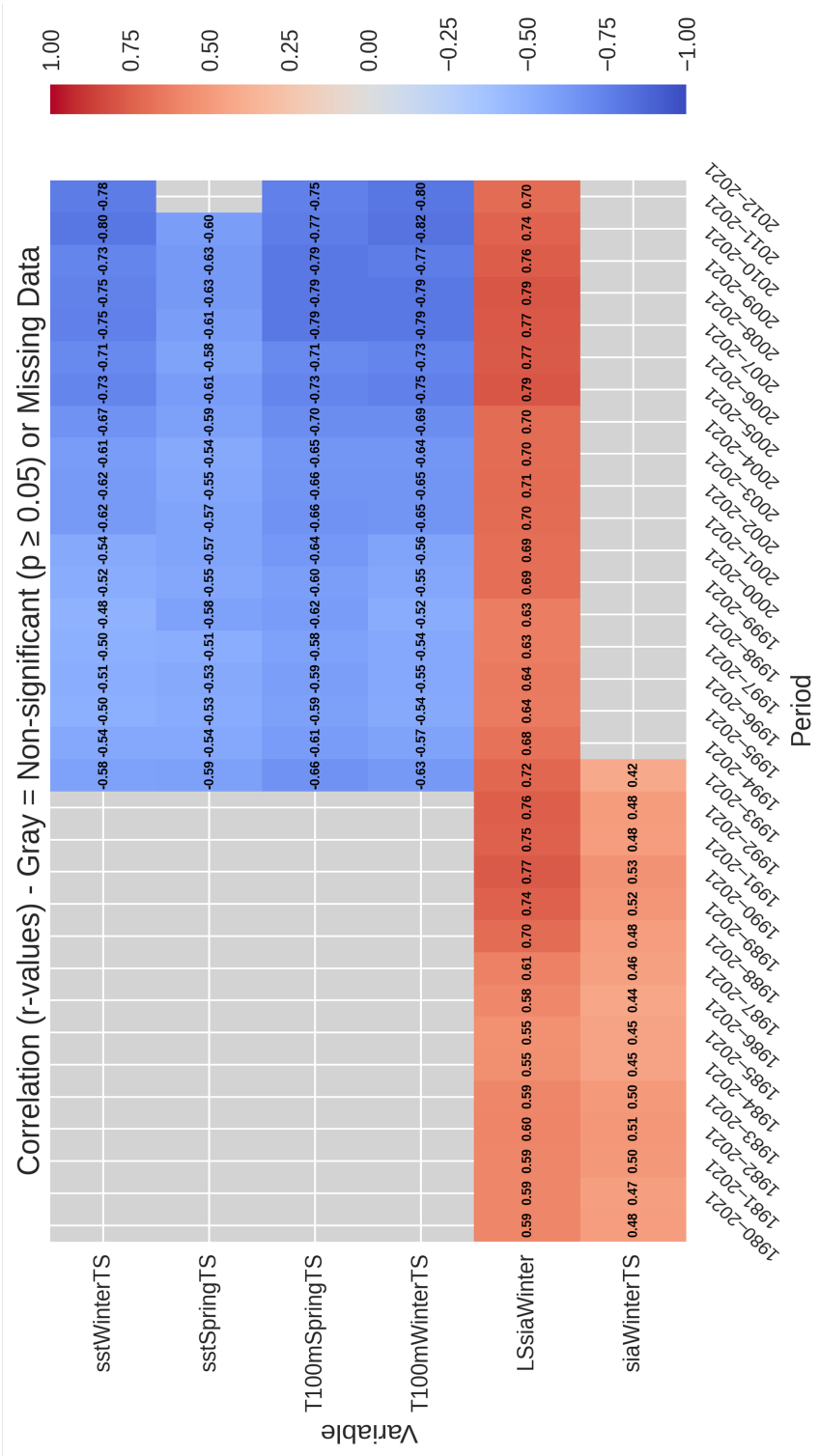

Figure 3.14: Heat map showing the observed Pearson correlation values (along with p-values) between the environmental factors and I48N for Labrador shelf winter SST (sstWinterTS), Labrador shelf spring SST (sstSpringTS), 100 m depth averaged spring ocean temperature over Labrador shelf (T100mSpringTS), 100 m depth averaged winter ocean temperature over Labrador shelf (T100mWinterTS), winter sea ice area over Labrador shelf (LSsiaWinter), and Baffin Bay high concentration winter sea ice area (siaWinterTS).

ice cover over Baffin Bay might have likely allowed icebergs to survive longer and reach 48° north in higher numbers. Over the last two decades (for the period from 2001 to 2021), however, the pattern is not as prominent except for the sub-decadal period of 2012 to 2016. For this period of time the correlation dropped to a statistically insignificant as well as smaller value ($r = 0.32$, $p = 1.7 \times 10^{-1}$). There are prominent differences between the I48N severity values occurring in years that had sea ice covered area values very close to each other, for example: 1988 and 2015 both had approximately 21.35×10^5 km^2 area in Baffin Bay covered with high concentration sea ice, but 1988 was a light season, whereas 2015 was a heavy one. We can see similar discrepancies during the years 2003-2010, 1994-1995, and 2012. This indicates that the impact of this remote factor on iceberg season severity for the two most recent decades decreased compared to the earlier period represented in the plot. We propose that two impetus could cause this lack of synchronicity: (1) other local or remote factors increased to contribute to the season severity more than previous decades. To test this hypothesis, we computed the correlations between Labrador sea ice area in winter and spring for the whole 43 years period, and also for the two periods mentioned above. While, for the entire period the correlations of both winter ($r = 0.71$, $p = 1.25 \times 10^{-7}$) and spring ($r = 0.70$, $p = 1.57 \times 10^{-6}$) sea ice areas with I48N are very close to each other, the spring sea ice grew to have higher correlation value with I48N from 1979-2000 ($r = 0.73$, $p = 1.25 \times 10^{-4}$) to 2001-2021 ($r = 0.74$, $p = 2.11 \times 10^{-4}$). Meanwhile, the winter sea ice correlation value with I48N took a much higher leap from 1979-2000 ($r = 0.70$, $p = 2.87 \times 10^{-4}$) to 2001-2021 ($r = 0.82$, $p = 8.48 \times 10^{-6}$).

However, we did not use a dataset for ocean temperature that dates back to 1979. Therefore, we do not have means to test if the other local factors considered in our study had altered correlations with I48N. (2) the seasonality of the occurrence of high concentration sea ice in Baffin Bay might have shifted, causing changes in the lags between this factor and I48N. For example we considered the correlation of 1986 winter sea ice anomaly over the entire Baffin Bay basin with the iceberg anomaly of the severity year 1986 (that is October 1985 to September 1986). The fact that the icebergs that populated Grand Banks for that season might not all be impacted by the 1986 winter sea ice anomaly from all over the Baffin Bay were not incorporated. Some of the icebergs that reached earlier in the 1986 peak season or during the 1985 fall, could have traveled through sea ice during other seasons in the year 1985 at some parts of Baffin Bay (most likely northern), that have winter sea ice cycles

different from other parts. Icebergs from northern glacial outlets could travel with or can be stuck in the sea ice packs in other seasons, or more than one season in the Baffin Bay gyre. Lack of observations in the northern area make it difficult to find the distribution of time spent by icebergs inside Baffin Bay. Hence, this hypothesis could be a subject to future research.

3.1.3 Section synopsis

During the iceberg season on the east coast of Canada, the major iceberg influx occurs during the months of April and May. This seasonality has been stable for decades, the 1990's numbers are particularly high (figure 4.1)while, the interannual variability of I48N in the current reconnaissance period has increased. Among the local variables that can be impacting the I48N interannual variability, the Labrador shelf winter sea ice area showed a stronger correlation with the year-to-year variation in the I48N, followed by the spring ocean temperature. Moreover, the correlation between the Labrador shelf winter sea ice area and I48N improved significantly in the last two decades compared to the final two decades of the previous century. Among the remote environmental factors that can be influencing the I48N interannual variability, the calving rates only from North sector of Greenland found to have a statistically significant correlation with the interannual variability in I48N. Furthermore, the winter sea ice area with high concentration over Baffin Bay exhibited reasonably good correlation with the I48N variability. Although, this correlation deteriorated in this century from the last two decades of previous century.

3.2 Model output evaluation

In this section, we evaluate the model for the observed relationships between the environmental conditions and I48N. In other words, we investigate whether the model is reproducing observed I48N characteristics, and its relationships with factors showing interconnections in the previous section. For this analysis, we used outputs from the **C**GRF **F**orced **A**tmosphere (CFA) simulation (configuration details in chapter 2) to compare with the observed properties of I48N. This simulation was forced with CGRF atmospheric forcing, initiated with no icebergs in the ocean and no ice mass collected in the size class bins. The period of this simulation is 16 years (2002 to 2017).

3.2.1 Characteristics of modelled iceberg season

To evaluate the model's representation of characteristics of the iceberg season on east Canadian coast, we first compared the seasonality observed by the IIP with the seasonality produced by NEMO in the CFA simulation. In figure 3.15, the modelled seasonality represented by the orange bars agrees with the observed seasonality (the blue bars), both averaged over the years 2003 to 2017, except for a shift in the peak from April to May. However, given that it is not uncommon to have a peak in May in observations (refer to figure 4.1 for peak months in different decades), this shift does not necessarily translates to a model misrepresentation of the iceberg season at the Grand Banks. The interannual

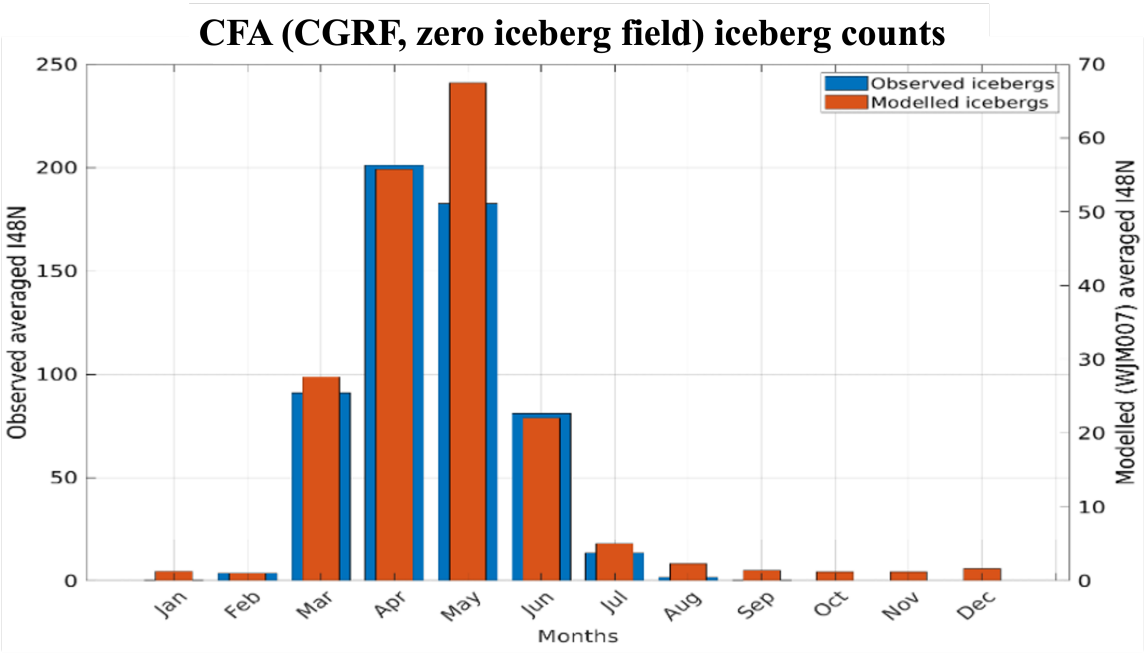

Figure 3.15: The modelled (CFA) average seasonality of I48N averaged over the period (2004 to 2017) of the simulation with CGRF-forced atmosphere (**CFA**).

variability, on the other hand, is not well represented by the CFA simulation (figure 3.16). The yearly total iceberg counts crossing 48°N latitude line are underestimated (compare the left and the right Y-axes in the figure 3.16) in the model. This reduced number can be a result of the definition of the size classes in the model. Furthermore, the breaking of one iceberg into pieces are not accounted for in the modelled iceberg numbers. We see discrepancies in model

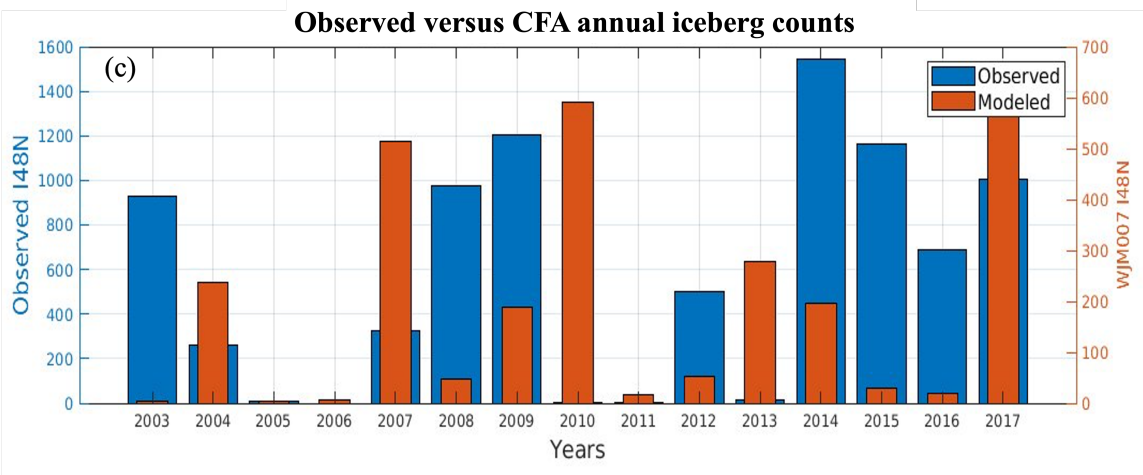

Figure 3.16: The modelled (CFA) yearly total **iceberg** counts crossing 48° N in an IIP-defined iceberg year.

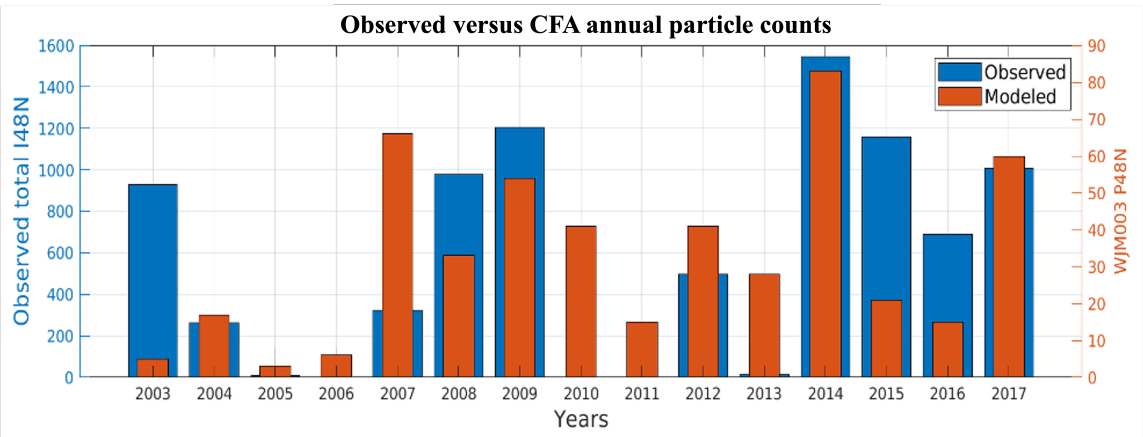

Figure 3.17: The modelled (CFA) yearly total **particle** count crossing 48° N in an IIP-defined iceberg year.

representation of the variation in the number of icebergs crossing 48° N from one year to another. For example, 2010 was observed to be a light iceberg season (blue bars), whereas in the model (orange bars) more than 550 icebergs crossed 48°N, which is categorized as an extreme year in CFA (table 3.1). However, in the model the icebergs are calved in a very idealized manner, i.e. ten size classes with a fixed distribution of mass and an arbitrary number of icebergs in each particle. Those modelled 550 icebergs reaching 48° N in the year 2010 could all be particles from medium size classes, but could also be three or four small size classes. That is, a large number of icebergs at 48° N in the model does not mean the same as in the real world: it is possible that only one particle is crossing that latitude, but that particle contains multiple icebergs. Which would also mean that over-estimation in the number could be attributed to particles/size classes, instead of a distortion of effects of ocean dynamics, and atmospheric condition on the iceberg movement and deterioration in North Atlantic, and in turn on the iceberg occurrence in the east coast of Canada. Hence, we compared the interannual variability between observed icebergs and the modelled particles (P48N) reaching 48° N latitude to investigate the role of mass scaling attribution of the particles/size classes. The orange bars in figure 3.17 represent the annual total number of particles crossing 48° N latitude for IIP-defined iceberg years. We see a better consistency in the pattern shown by year-to-year changes in particle counts compared to the yearly total iceberg counts (compare with the orange bars in figure 3.16). This indicates that the magnitude (absolute value) of the yearly counts of modelled icebergs is not of utmost importance, and evaluating the model representation of severity class ranges would be of more value for this current work. So, instead of evaluating the model for the yearly I48N, we evaluated it based on how the observed correlations are holding up for different severity classes. The reason behind the striking discrepancy between observed and modelled iceberg counts could be as follows: (i) the size-class representation of icebergs in the models is still far from reality. (ii) as the icebergs inside one particle in the model do not spread out and are treated as one point, once one iceberg in the parcel melts, the whole particle vanishes. That means, if an iceberg in the particle of smallest size class melts, or is stuck is sea ice pack before reaching a latitude, we iceberg count is 2000 less in terms of number of icebergs crossing that latitude. (iii) once an iceberg is split into more than one pieces in reality, they add to the number. Whereas in model, the icebergs' counts are same inside one particle from the start to end.

To keep it consistent with the IIP methodology of categorizing the observed

iceberg counts into four severity classes, we used the middle 50% method (described in chapter 2 in details) to define the ranges for the four severity classes of the iceberg season in the model simulations. In the CFA simulation, those ranges and monthly means are shown in the second column of table 3.1 and in figure 3.18 respectively. As shown in the previous section, the icebergs reach the

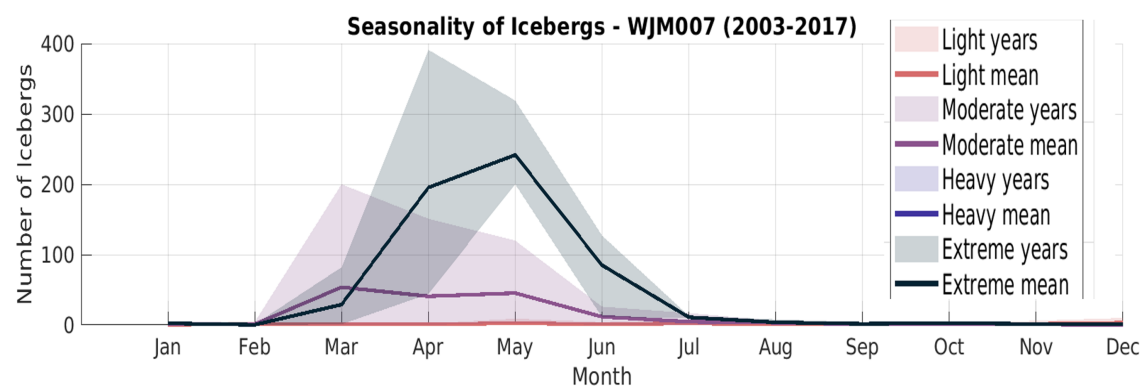

Figure 3.18: The modelled (CFA) monthly iceberg counts distribution across different severity classes.

shipping lanes from late February to August and their count reaches the peak in the months of April and May. The peak month of the observed light, and the extreme iceberg seasons in the CFA simulation matched with the peak month during the observed light, and the extreme iceberg seasons during the current reconnaissance period of IIP (figure 3.4). However, the moderate iceberg seasons in the model had peak in March, and a very close second peak in May, whereas the observed moderate seasons have them in April and May respectively. [Marsh et al., 2015] and [Marson et al., 2021] both recognized that it takes the model 15-20 years to have the iceberg mass in the Northern Hemisphere stabilized. Hence, in these results there could be biases introduced by the underestimation of iceberg counts during first few years, as the simulation CFA started with no particles in the domain, and the catchments for each size class were still accumulating ice. In other words, the fact that this simulation started with no icebergs in the ocean and no ice mass collected in the bins of different size classes means that the simulation does not have a nearly constant inflow of icebergs at 48° N latitude. Instead, iceberg numbers grow as the model starts calving particles in CFA simulation. Therefore, the interannual variability of I48N in this simulation is not only dependent on the environmental forcings, but also on the growing supply of particles upstream.

Table 3.1: Definition of severity classes for outputs of the simulations CFA (second column), and JFA (third column).

Severity	CFA	JFA
Light	0-37	0-10
Moderate	38-338	11-45
Heavy	339-473	46-60
Extreme	≥ 474	≥ 61

3.2.2 Seasonal distribution varying with sizes of the icebergs

To test whether the modelled seasonality of iceberg occurrence in the east Canadian coast is sensitive to the sizes of the icebergs, we plotted the seasonality of the particles in the CFA simulation (figure 3.19b) along side its number of icebergs counterpart (figure 3.19a). In figure 3.19a the seasonality of icebergs of different size classes (large, medium, and small, refer to the definition in section 3.3) show that the larger (red bars) class icebergs keep drifting to 48°N all year round, whereas the small (yellow bars) and medium (orange bars) icebergs maintain the observed season width in the model. This difference in the season span is even clearer in figure 3.19b, where we plotted only the count of particles reaching 48°N in the model. Only the large particles arriving outside of the IIP-defined iceberg season could be the reason behind the model having a season longer than the observed season (figure 3.15). Since modelled iceberg count is underestimated by a factor almost 1/5th of the observed counts, even a very small number of icebergs crossing 48° N outside of the season-months add to the widening of the season in the model. This effect is more pronounced in figure 3.20 as it represents the number of particles reaching Grand Banks in the model along with the observed I48N. The reason behind the different seasonality according to the icebergs' sizes could be:
As spring advances, the smaller particles melt farther north before reaching 48° north latitude. To assess this hypothesis, we plotted seasonality of occurrences of particles with different sizes at six chosen latitudes (58, 56, 54, 52, 50, and 48° N) along the Labrador coast (refer to figure 3.21). The subplots (a), (b), and (c) in figure 3.22 show the average seasonality for P58N, P56N, P54N, P52N, P50N, and P48N of large, medium, and small size classes respectively. The lower the

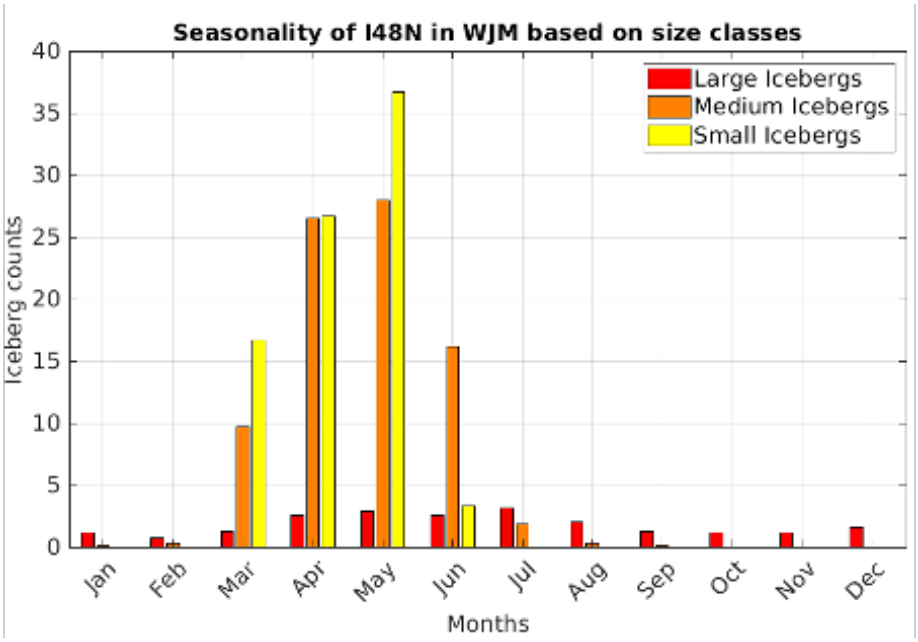

(a) I48N

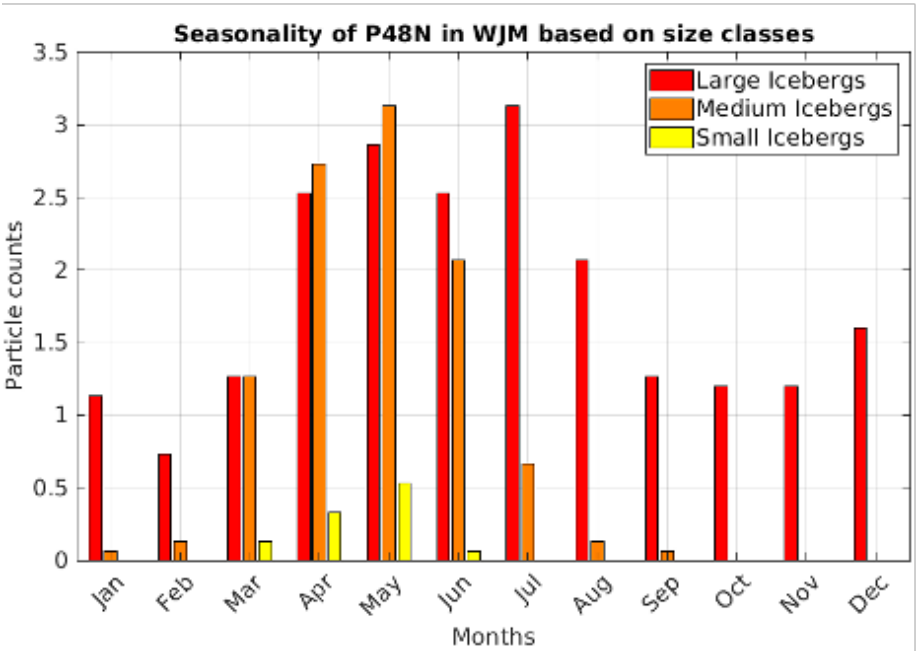

(b) P48N

Figure 3.19: Average (2003-to-2017) seasonality of (a) icebergs from large (red), medium (orange) and small (yellow) size classes, (b) particles from large (red), medium (orange) and small (yellow) size classes.

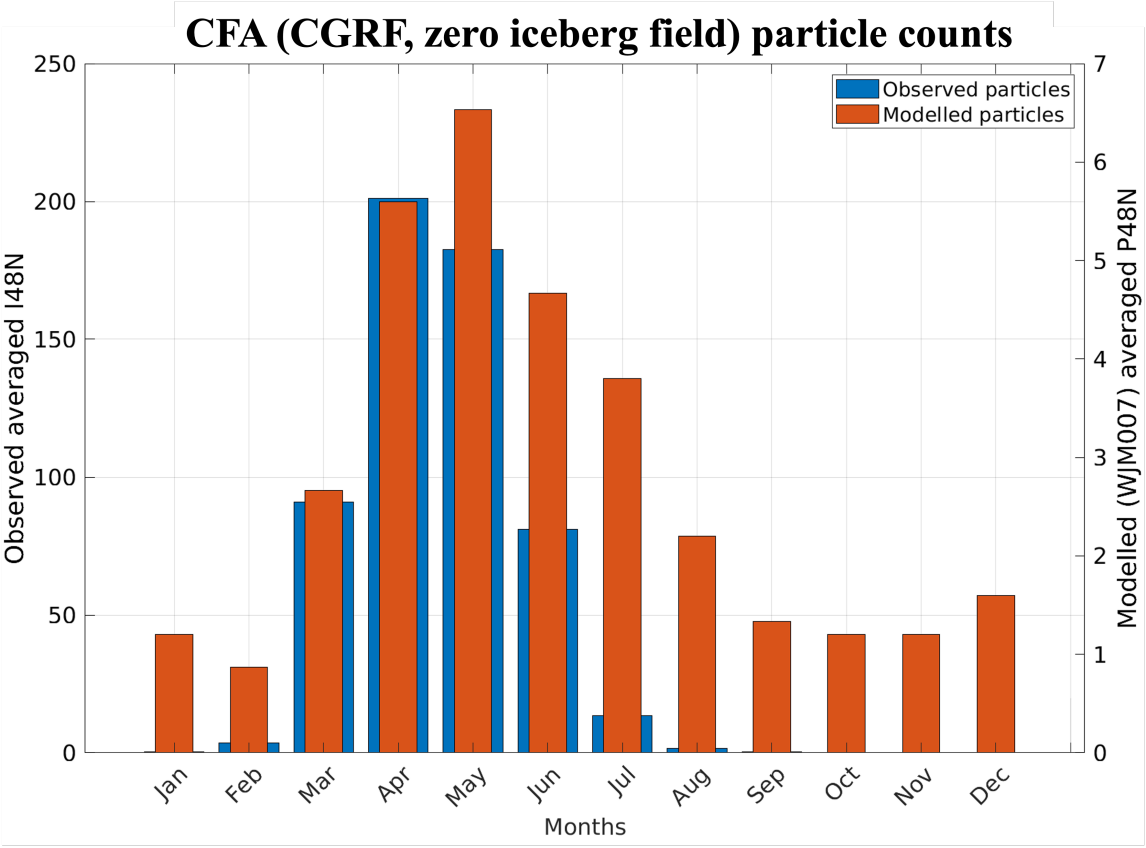

Figure 3.20: Observed icebergs (blue bars) with modelled (CFA) particles from all size classes (orange bars).

latitude, the lighter the color of the line representing the seasonality. Even though the peak arrival month at almost all further north latitudes (for example, 58, 56, and 54° N latitudes) for particles of all sizes is March, the drop in the influx of icebergs vary based on sizes across the further south latitudes. For example, for the large particles (figure 3.22a) the counts in the peak month (March) are closely followed by influxes over late fall and winter months (December to March). The peak arrival months for the medium particles (figure 3.22b) at northern part of Labrador coast is March, and at the southern part are April or May. On the other hand, for the small particles (figure 3.22c) the peak month shifts from February to May as we go further south. The seasonality at 58° N for large particles have a very prominent second peak in October, which is less pronounced for medium particles, and vanishes for the small particles. This

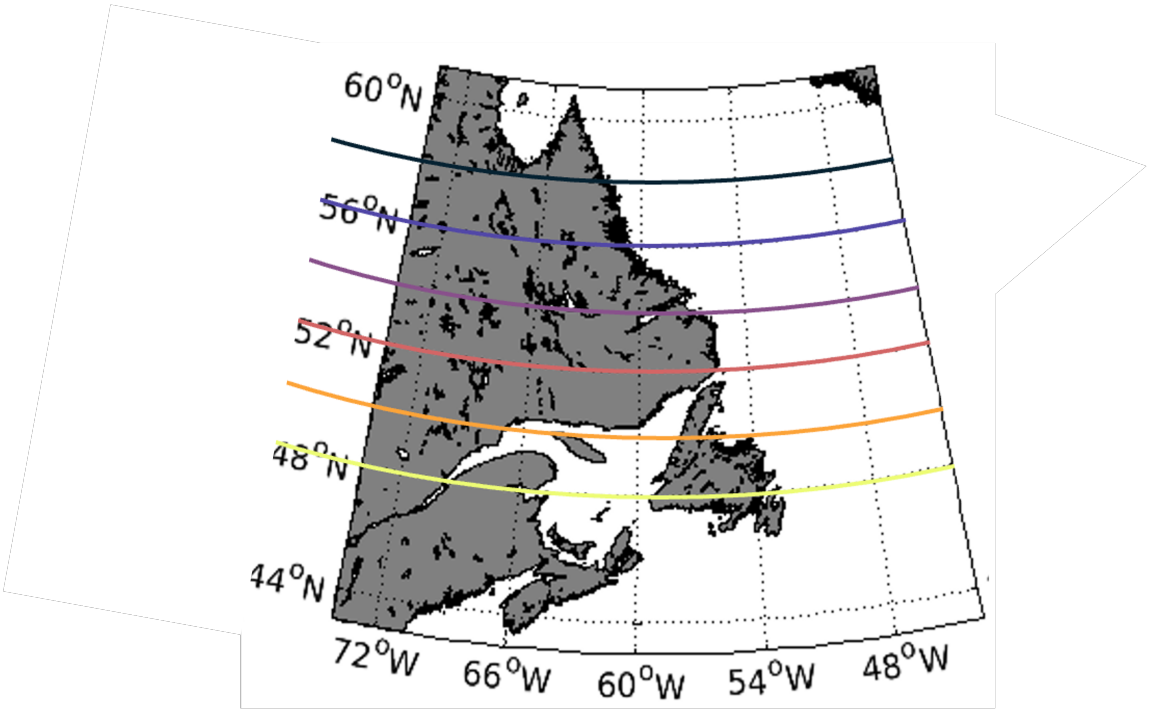

Figure 3.21: The six latitude lines along the Labrador shelf, used to calculate the gradual reduction of the iceberg flux that enters the Labrador current. From the darkest to the lightest line the latitudes are from north to south: 58° N (darkest lines), 56° N, 54° N, 52° N, 50° N, and 48° N (lightest line).

resembles with the upstream oceanic condition, such as sea ice cycle. The late winter sea ice concentration in the Davis Strait and the northern Labrador lowers the ocean temperature in that region [Marko et al., 2014] ensuring the survival of the icebergs from all the sizes further south. This explains the first peak in all three subplots. Whereas, the upstream summer environmental conditions are likely controlling the survival/dissipation of the particles before reaching 58° N October onward.

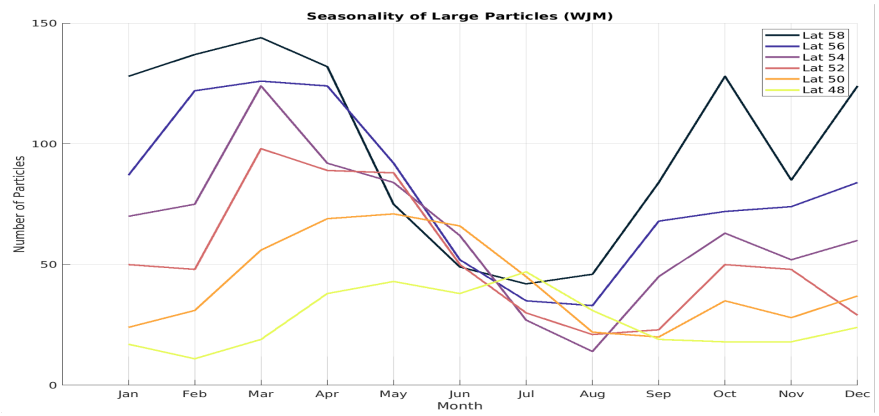

(a)

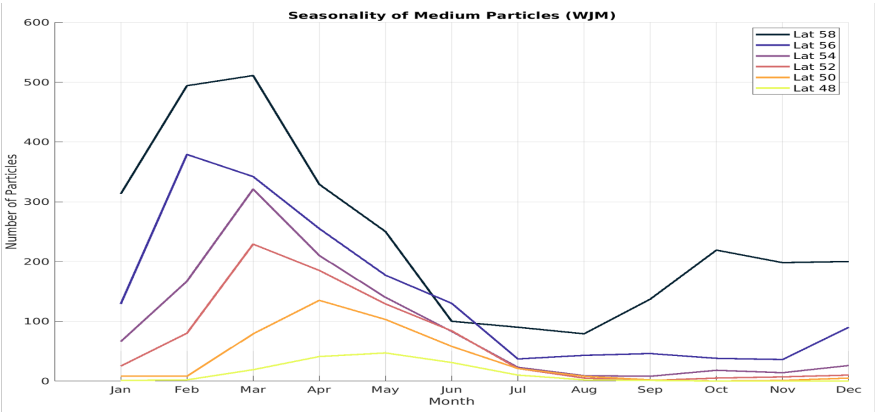

(b)

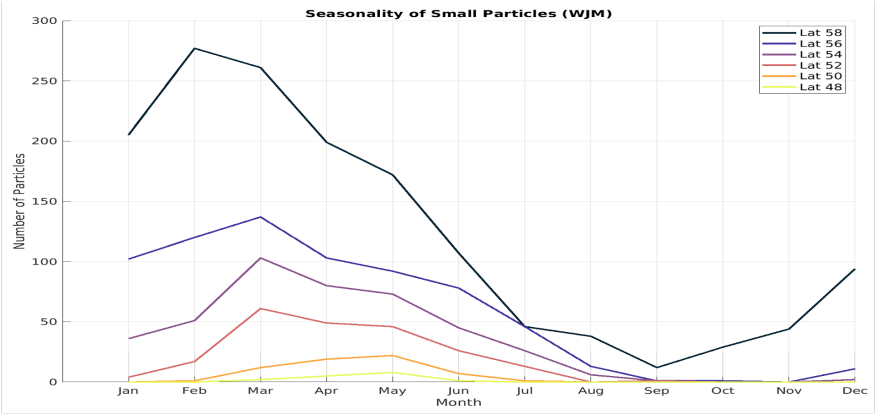

(c)

Figure 3.22: Seasonality of count of (a) large size-class, (b) medium size-class, and (c) small size-class particles reaching 58° N (darkest lines), 56° N, 54° N, 52° N, 50° N, and 48° N (lightest line) latitude in the simulation CFA.

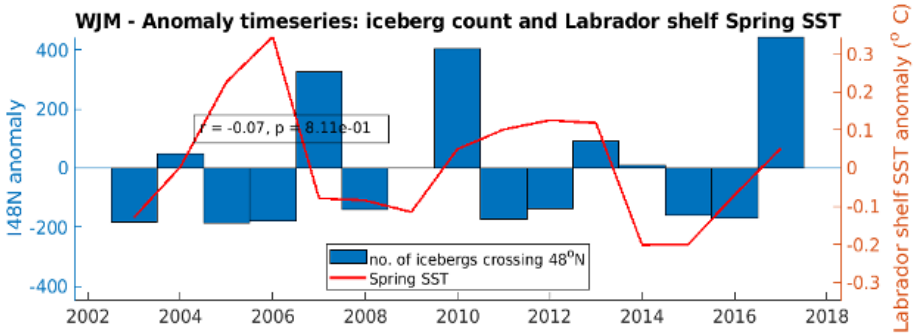

(a) CFA Labrador shelf mask Spring SST

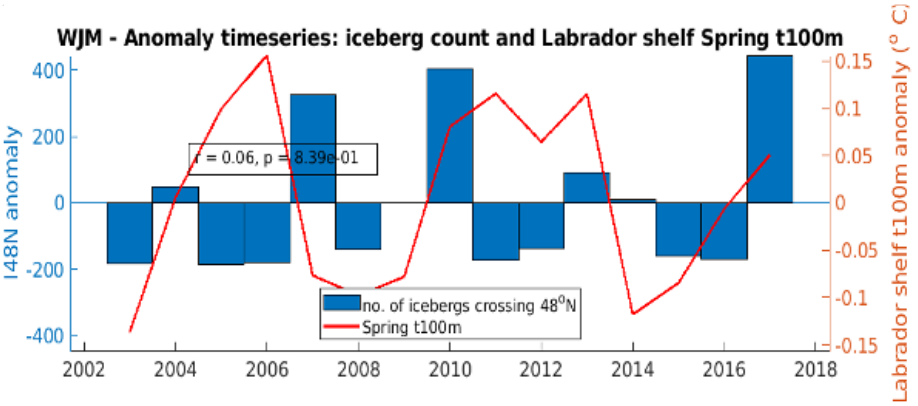

(b) CFA Labrador shelf mask Spring depth-integrated temp

Figure 3.23: Anomaly of yearly (October to September) total number of icebergs crossing 48° N, averaged over the period of simulation (blue bar) with (a) the anomaly in SST (in °Celsius, red line), and (b) the anomaly in temperature (in °Celsius, red line) averaged over the upper 100 meters of ocean over Labrador shelf mask in the simulation CFA.

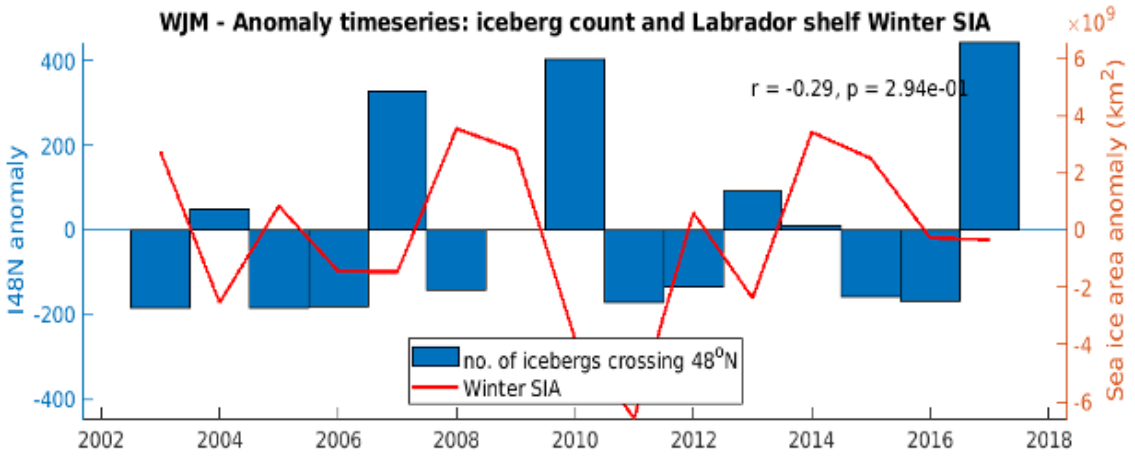

Figure 3.24: Anomaly of yearly (October to September) total number of icebergs crossing 48° N, averaged over the period of simulation (blue bar) with the anomaly in area over Labrador shelf covered with sea ice during the winter months (January to March) in the years 2003 to 2017) in the simulation CFA.

3.2.3 Evaluation of the relationships between I48N and environmental conditions

3.2.3.1. Local conditions

Figure 3.23a shows the yearly time series of the Labrador shelf mask spring SST anomaly (red line) and the yearly total I48N anomaly (blue bars) in the CFA simulation. The iceberg mass in the modelled ocean started stabilizing in the CFA simulation since the year 2006 (one can refer to the figure 3.29 which we discuss in the next section in details). Therefore, we considered correlations between the environmental factors and I48N in the CFA simulation from the year 2006. The correlation value is almost zero (r = - 0.04) and statistically insignificant (p-value = 0.90) for the years 2006-2017. Figure 3.23b shows the yearly time series of the anomalies of spring temperature over the Labrador shelf mask averaged over upper 100 meters of the ocean (red line) with the yearly total I48N anomaly (blue bars) in the CFA simulation. This correlation is not significant as well (r = 0.14, p-value = 0.66). Figure 3.24 shows the relationship between the time series of the anomaly in winter sea ice area on the Labrador shelf mask (red line) and the anomaly in yearly iceberg counts crossing 48°N

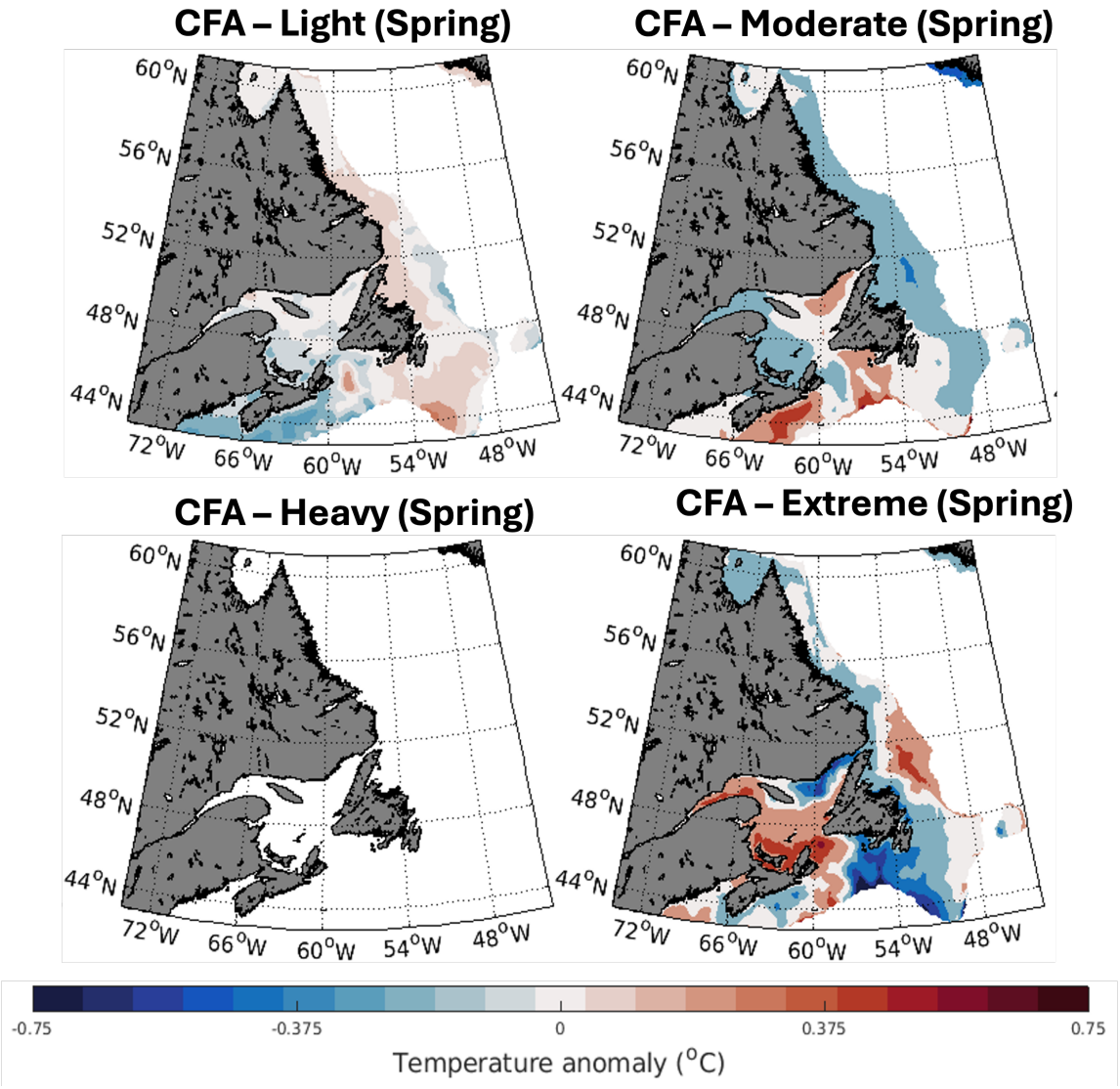

Figure 3.25: Spatial distribution of modelled (CFA) depth-integrated temperature anomaly (in °Celsius) on the Labrador shelf during the spring months (April to June) across the severity classes. In CFA, there was no heavy iceberg season, so, the third figure (CFA - Heavy (Spring) does not have any data.

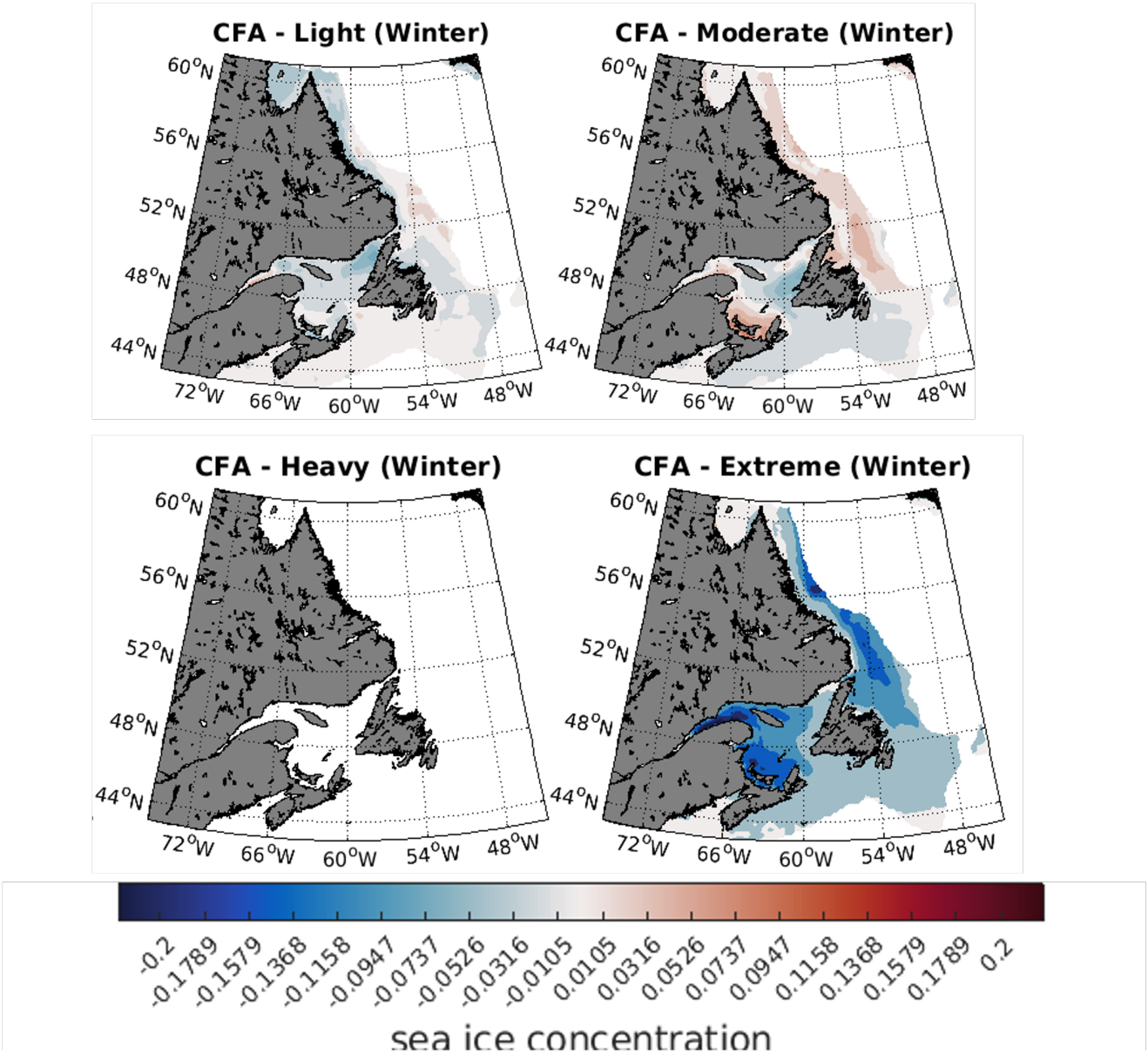

Figure 3.26: Spatial distribution of modelled (CFA) sea ice concentration anomaly on the Labrador shelf over the winter months (January to March) across the severity classes.

(blue bars), which also has no significant correlation (r = -0.27, p-value = 0.66). To test how the iceberg mass stabilization in the ocean impacts the correlations immediately we computed the correlation between I48N anomaly and Labrador shelf winter sea ice anomaly for the years 2004-2017. Although the correlation value improved from -0.24 in 2004-2017, both were still statistically insignificant (p-values ≥ 0.05). This finding deviates from significant observed correlation between winter sea ice condition on the Labrador shelf mask and I48N. Since this simulation was initiated with no iceberg field, and the iceberg spin up time is about 15-20 years for Northern Hemisphere, the lower iceberg counts especially in the initial years of the simulation could be a source of bias in the modelled interconnections between the local oceanic conditions and I48N variability in the CFA simulation. This indicates that even though the iceberg mass in the ocean stabilizes after few years, the model likely needs longer spin up time to reflect the real world correlations.

The spatial representation of the anomalies in the depth-averaged spring ocean temperature on the Labrador shelf mask (upper 100 meters of the ocean) across the severity categories (defined based on the yearly iceberg counts in the CFA simulation) is shown in figure 3.25. A noticeable decrease in the ocean temperature (of value 1 to 1.5° Celsius) along the coastline of Newfoundland and Labrador is noticed as the modelled season severity increases. This also could reserve the relationship closer to the southern Labrador/Newfoundland shelf break, and parts of the Gulf of St Lawrence. This deviation from observed relationships might be related to changes in circulation that is not reflected in the model. However, this needs more investigation in the future. The winter sea ice concentration anomaly (figure 3.26) over the Labrador shelf mask across the severity classes, however, appears to behave the opposite way from what is expected: less sea ice is associated with extreme iceberg seasons, not light ones. The reason why the CFA outputs are not reflecting the real world correlations between the I48N variability and its potential local driving factors could be: (i) the growing population of icebergs in the CFA simulation might have introduced a bias in the I48N variation; (ii) statistical distribution of the calving into the different size classes is yet to be realistically represented for the Northern hemisphere.

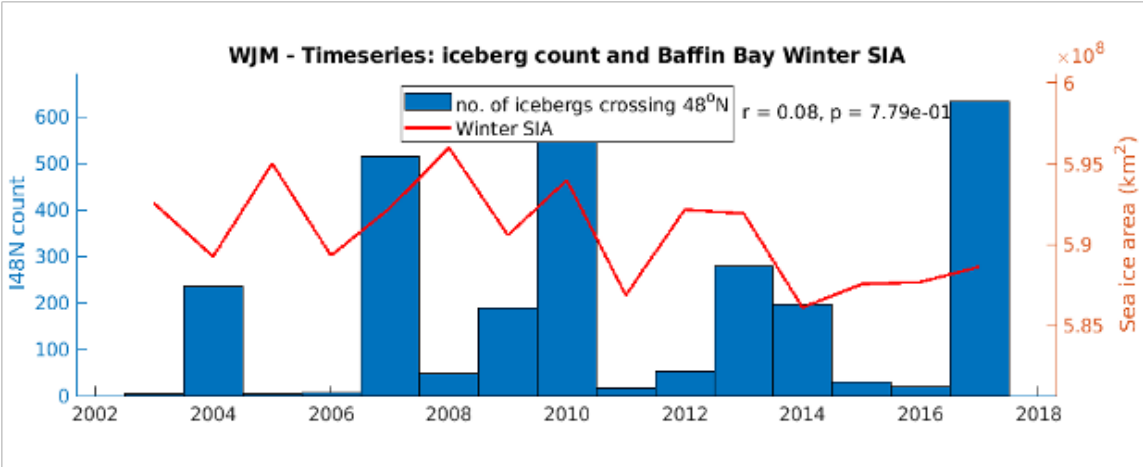

Figure 3.27: Modelled (CFA) yearly total iceberg count (blue bar) and the area (in km^2) of Baffin Bay covered with sea ice with high concentration ($\geq$ 90%) in the winter months (January to March) in the simulation CFA.

3.2.3.2. Remote conditions

Figure 3.27 shows that the yearly time series of the winter sea ice covered ($\geq$ 90%) area in Baffin Bay (red line) shows a statistically non-significant correlation value (r = 0.08, p-value = 7.79×10^{-1}) with the interannual variability of total I48N (blue bars) in the CFA simulation. Moreover, to investigate if the relationship between the Baffin Bay winter high concentration sea ice and the variability of iceberg season severity improves with the period of computation, we calculated it over the years 2004-2017 (r = 0.12, p-value = 6.75×10^{-1}), and 2006-2017 (r = 0.26, p-value = 4.10×10^{-1}). Both showed non-significant correlations. However, the spatial patterns (figure 3.28) in Baffin Bay high concentration ($\geq$ 90%) winter sea ice anomaly (figure 3.27) indicates that, overall, Baffin Bay experiences more extensive sea ice coverage during the winters before the heavier iceberg seasons compared to the winters before the lighter seasons. In particular, the mid to Northeastern part of Baffin Bay displays higher sea ice concentration on years with heavier iceberg season. Observations tend to show higher correlation with the sea ice edge (refer to figure 3.10), whereas the model exhibits better correlation in the middle of the pack. Since the Northwest Greenland sector is one of the most important contributors to the I48N, the similarities between observed and modelled winter sea ice anomaly spatial pattern near this sector in the CFA simulation might indicate that the sea

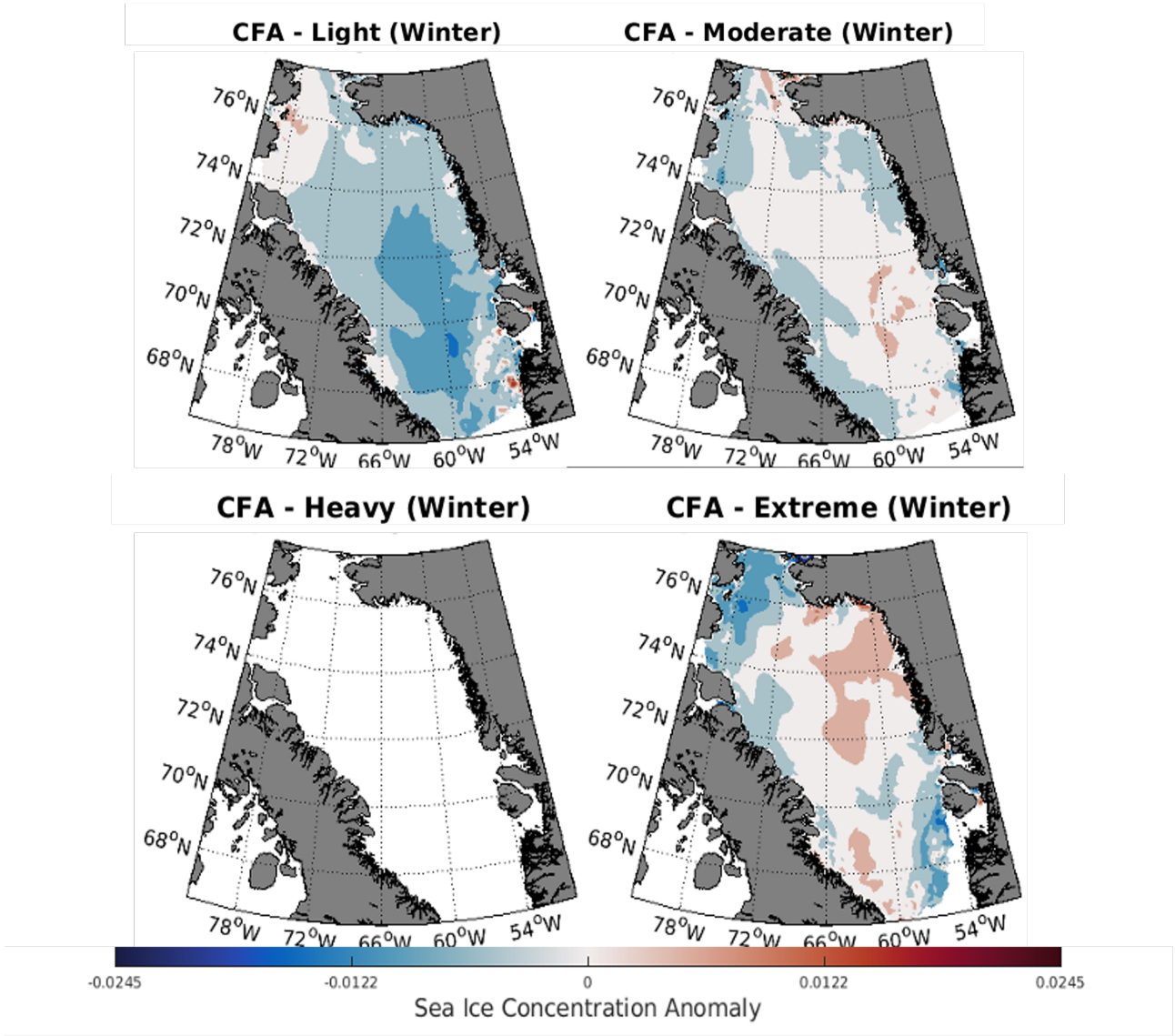

Figure 3.28: Spatial distribution of modelled (CFA) sea ice with high concentration ($\geq 90\%$) across the severity classes.

ice concentration in this region could have an impact on the trajectories of the icebergs that travel through this region, and in turn on their population in the Baffin Island Current (BIC).
The correlations (shown in figure 4.4) between I48N and the environmental conditions derived in the previous sections were majorly non-significant in the model (refer to the figure 4.5. We suspect that the reason behind this is the lack of time CFA simulation had to stabilize the iceberg field and to adjust the model components with it. We discuss this in further details in next section.

3.2.4 Section synopsis

The observed seasonality is reasonably well-represented in the CFA model simulation. However, even though the seasonal peak months were represented correctly, many modelled icebergs were reaching 48° N latitude outside of the IIP-defined iceberg season. To investigate whether those particles belong to any specific size-class, we found that the larger the size of the icebergs in the particles, the broader its season is stretched outside of the defined iceberg season on the east coast of Canada. Could these discrepancies occur due to the fact that the iceberg field in Northern Hemisphere takes 15 to 20 years to stabilize in the model? As the period of this simulation is only 16 years, many icebergs that could potentially reach 48° N were yet to enter Labrador coast, which could introduce bias to the results. The modelled interannual variability of P48N resembled the observed I48N a little better than the modelled interannual variability of I48N.

3.3 I48N sensitivity to atmospheric forcing and initial iceberg field

To test how the model depiction of the I48N properties and its correlations with the environmental factors responds to a more realistic initial iceberg condition, we made a new experiment with a longer simulation. In this section, we will explore how the characteristics of modelled I48N and its relationships with the local and remote environmental factors change when the model is initiated with icebergs in the ocean and partially filled ice "bins" at all Greenland glacial outlets. For this, we used the outputs from the NEMO simulation JFA (configuration details in chapter 2). The atmospheric forcing for this simulation was taken from JRA55-DO, and the simulation was initiated with the final year

iceberg field of the CFA simulation. The period of simulation is 25 years (1993 to 2017). As this simulation is integrated for a different period of time, and initiated with a non-zero iceberg field, this should not be considered as an ideal sensitivity study for the CFA simulation. To mitigate the differences between the two simulations, however, we eliminated the iceberg counts that were already in the ocean at the beginning of the JFA simulation. Moreover, to make the analyses more coherent, we compared the output for same time period while investigating the differences between CFA and JFA.

3.3.1 Model's response to initial iceberg field

Figure 3.29 shows the time evolution of the annual total iceberg mass (in kg/year) in the ocean for both the simulations JFA (upper panel) and CFA (lower panel) throughout their corresponding period of integration. The mass of iceberg in the JFA simulation is steady starting from its first year. On the other hand, in the CFA simulation, the iceberg mass in the ocean has a sharp positive trend from 2002 (0 kg/year) to 2004 (1.5 kg/year on an average). However, it took at least 5 years of integration for the iceberg mass to stabilize. This suggests that it is reasonable to analyze the iceberg counts for the whole 25 years period for the simulation JFA. It is noticeable that the highest value of icebergs' mass in the ocean in the JFA simulation was below 2.5×10^{14} kg/year and amplitude of approximately 1.25×10^{14} kg/year. In CFA, the maximum iceberg mass was above 2.5×10^{14} kg/year, with the same amplitude of approximately 1.25×10^{14} kg/year. Furthermore, in the JFA simulation, only 450 particles reached 48° N, whereas in CFA the number was 493 for the same period (2002-2017). This suggests that, in JFA the mass loss happening north of 48° N is higher.

3.3.2 Characteristics of the modelled iceberg season

Broader seasonality and peak shift

Figure 3.30 represents the seasonality of I48N in the JFA simulation, averaged over the years 1994 to 2017. The highest monthly averaged count of icebergs has reduced to almost one-tenth of the highest monthly averaged count of icebergs in the CFA simulation. The reason behind the low number of icebergs reaching 48°N in JFA is that most of the modelled particles crossing this latitude belong to large size classes, which contain a single iceberg (refer to table 2.3). We found that less than 10 particles from medium and small size classes reached 48°N

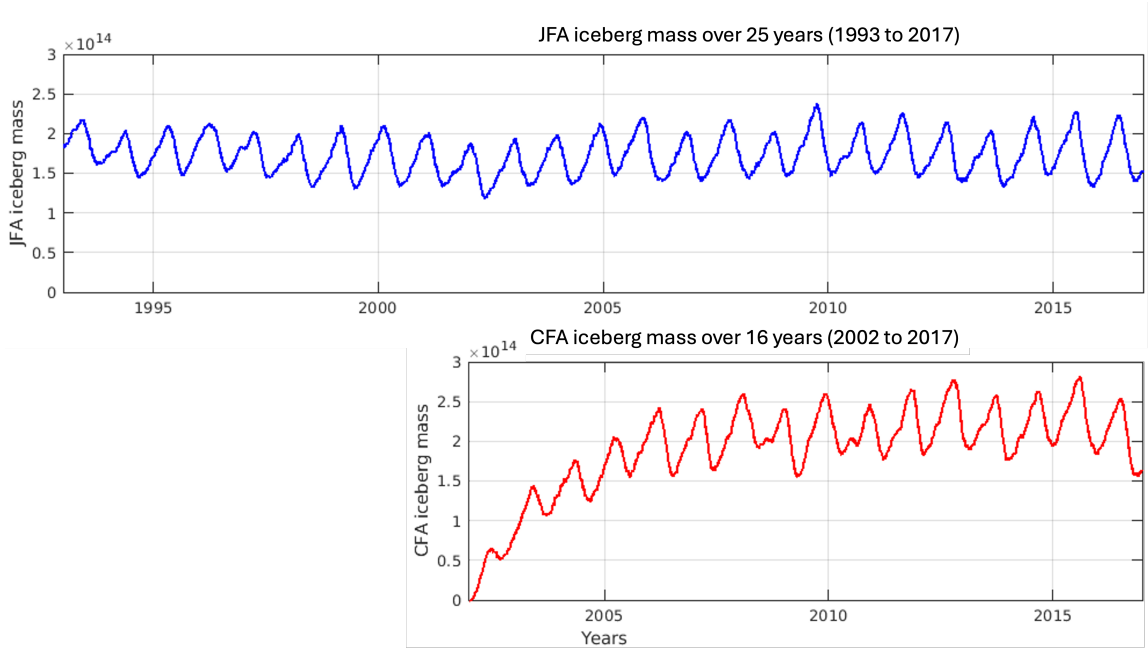

Figure 3.29: The annual total iceberg mass in the ocean (expressed in kg/year) for the whole period of simulation in JFA (upper panel), and in CFA (lower panel).

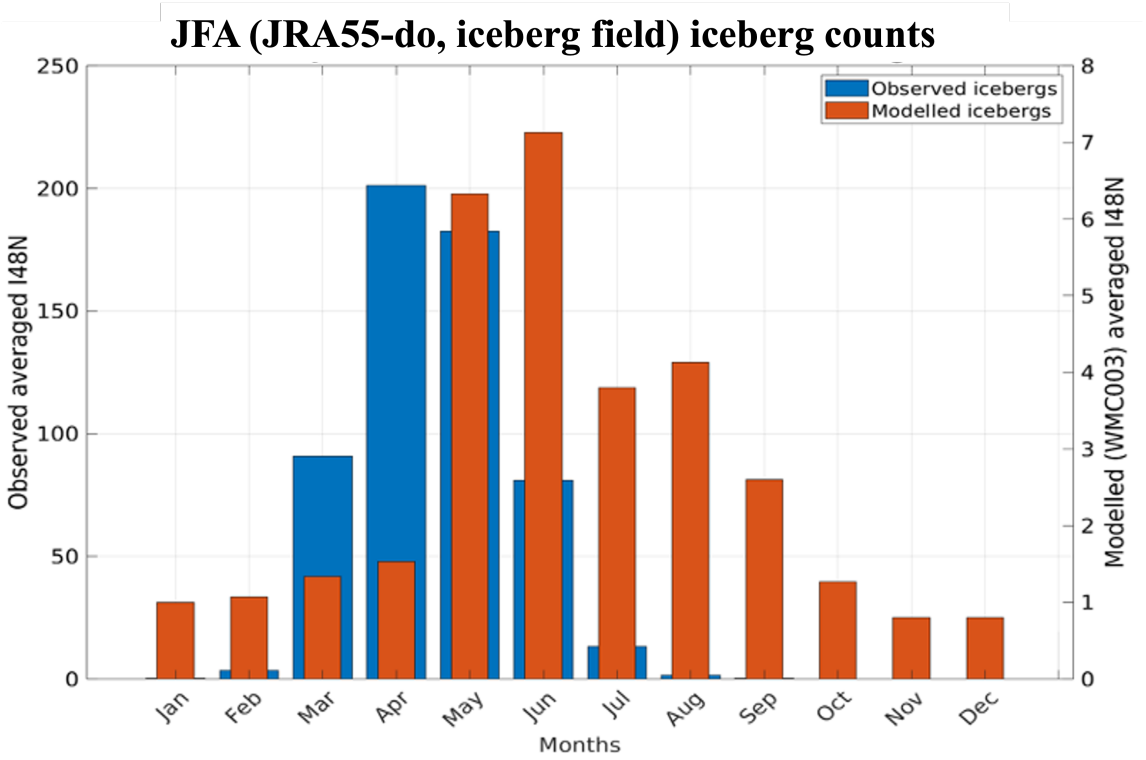

Figure 3.30: Monthly average number of IIP-observed iceberg (blue bars) with modelled average (a) iceberg count (orange bars) at 48°N, in the simulation JFA.

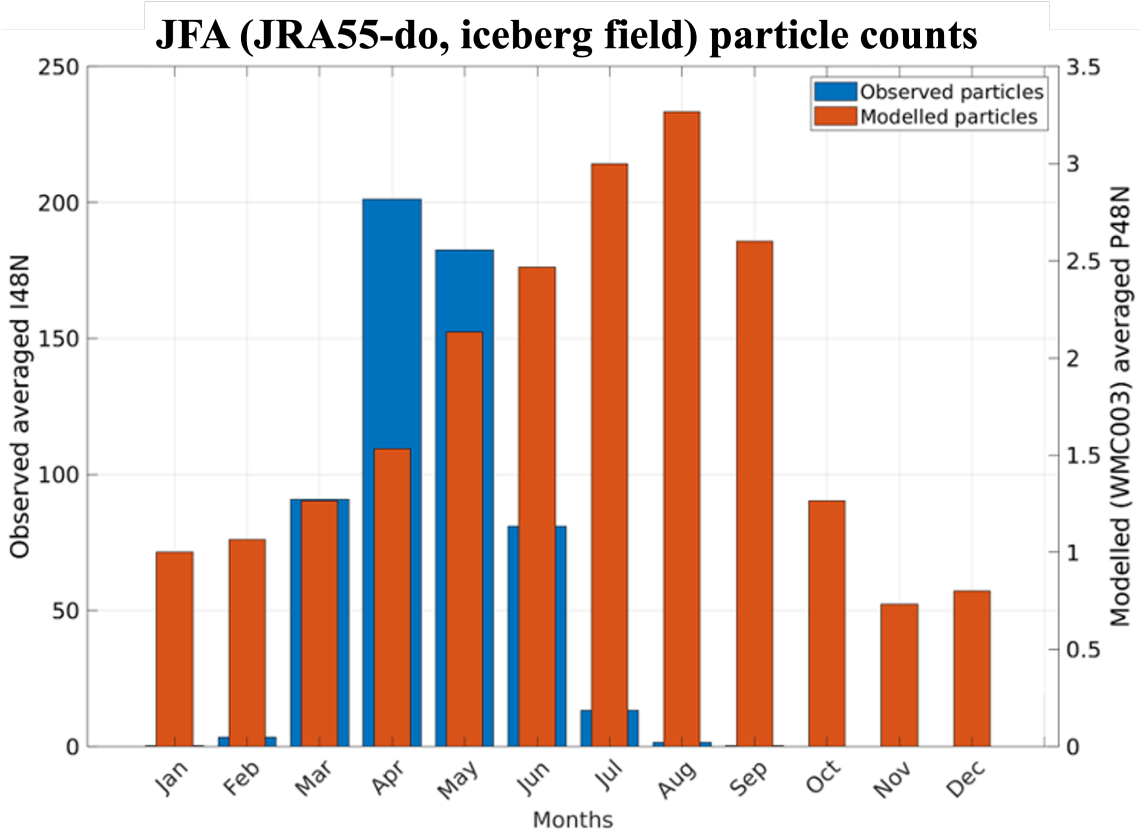

Figure 3.31: Monthly average number of IIP-observed particle (orange bars) at 48°N, in the simulation JFA.

latitude throughout JFA simulation, which is less than 2% of the total number of particles crossing 48°N in JFA.

The season is wider compared to the simulation CFA (refer to figure 3.15). In CFA simulation, approximately 6 out of 33 particles (18%) on an average reached 48°N every year during off-season months. Whereas, in JFA simulation almost 6.25 out of 18.75 particles (33%) reach every year during the off-season months. This extends the iceberg season in this simulation significantly broader in JFA. The peak month is June (7 icebergs on average) and the month with a second highest (6.5) averaged iceberg count is May in this simulation. That means the peaks have shifted towards later months in this simulation (compare to figure 3.15). Note that July is the month where the peak of the large size-class particles (3.2 on average) occurred in the simulation CFA. Figure 3.31 shows the averaged

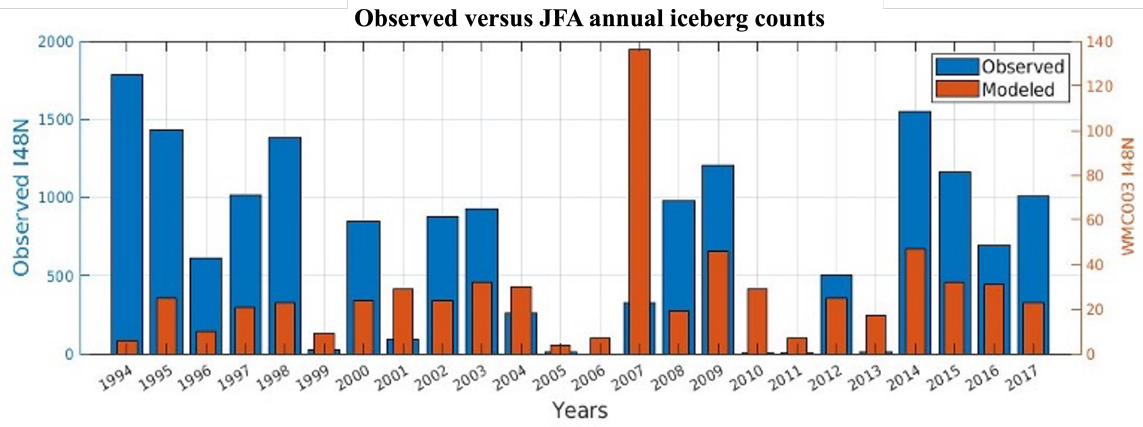

Figure 3.32: The modelled (JFA) yearly total iceberg counts for the years 2003 to 2017.

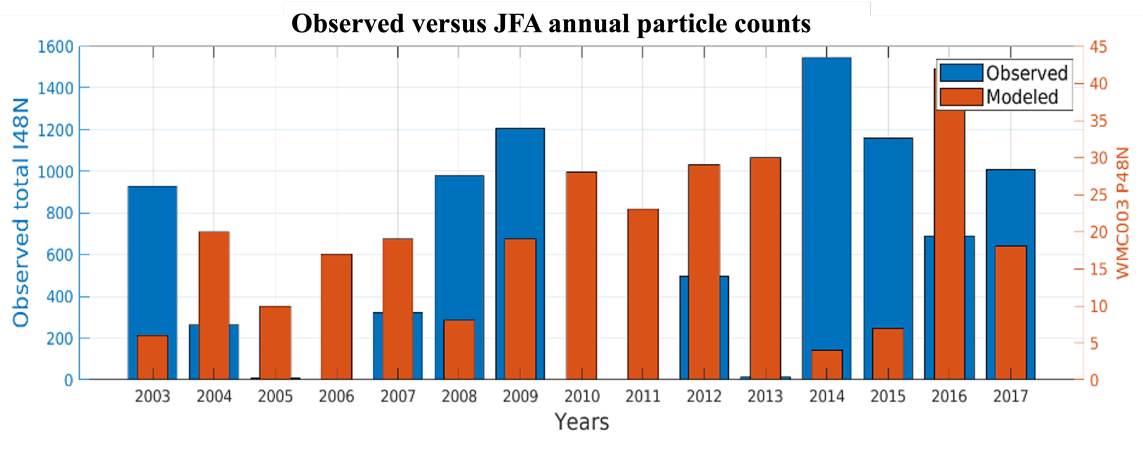

Figure 3.33: The modelled (JFA) yearly total particle counts for the years 2003 to 2017. There is only one extreme iceberg year in JFA, so only a single line representing seasonality of extreme years in the figure.

monthly particle count at 48°N latitude in JFA simulation (orange bars). While, the season of the particles in CFA simulation (orange bars in figure 3.20) is in May, in JFA this maximum is in August. The shift is explained by the dominance of large particles crossing 48° N in JFA simulation. Indeed, when we considered the seasonality of large particles in CFA simulation (figure 3.19b), the peak also occurs towards summer instead of spring. The longer time taken by the

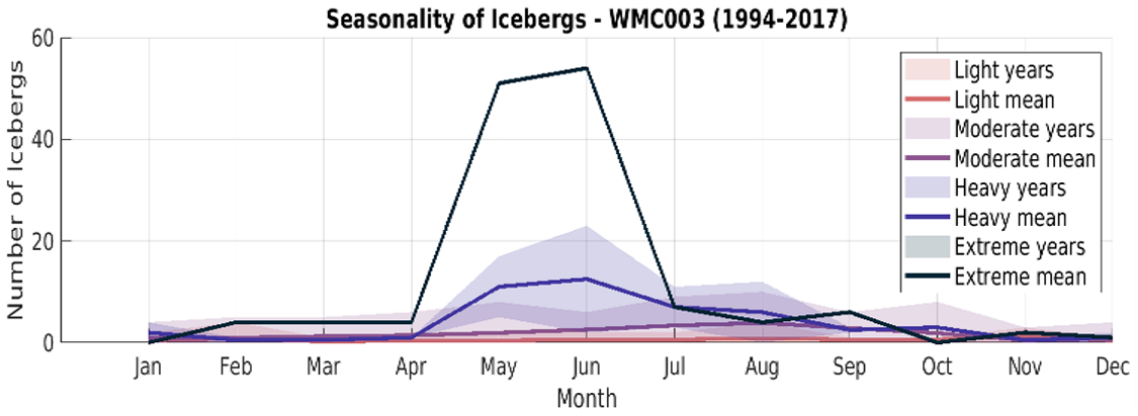

Figure 3.34: The modelled (JFA) seasonality averaged over the period (1994 to 2017).

larger icebergs could be attributed to their trajectories inside the Baffin Bay gyre. Further analyses of size-based trajectories of icebergs could shed more light on this matter, therefore, could be a path for future studies.
In terms of interannual variability of iceberg counts crossing 48° N, JFA (figure 3.32) shows an improvement over CFA (figure 3.16) due to the initialization of JFA with a "populated" iceberg field. The periods of increasing or decreasing severity in I48N improved in JFA, despite the under-estimation of the annual counts. The interannual variability of particle counts crossing 48° N in JFA (figure 3.33), however, is not holding up as good as the annual iceberg counts in this simulation. The ranges of monthly iceberg counts for different severity classes based on the definitions of the lower and upper limits of those categories in the JFA simulation are shown in figure 3.34. The season over all the severity classes became wider in JFA simulation compared to their counterparts in the CFA simulation. The most prominent shift in peak (to August) happened for moderate iceberg seasons. This explains the August peak in particle counts (in figure 3.31) in the JFA simulation. However, in this simulation only one year was qualified as an extreme season. Therefore, this result can not lead us to a unbiased conclusion about the model representation of the seasonality of an extreme iceberg season.

3.3.3 Seasonal distribution varying with sizes of the icebergs

To investigate how the seasonality varies with sizes and how far north it is established, we plotted the total counts of particles crossing the six latitudes (refer to 3.21) in every month for large, medium and small. The subplots (a), (b), and (c) in figure 3.35 show the average seasonality for P58N, P56N, P54N, P52N, P50N, and P48N of large, medium, and small size classes in JFA respectively. Similar to CFA (3.22), we see an increase in particles counts October onward. A noticeable characteristic is that the total number of particles per month is lower in JFA, even though the yearly total of large and medium particles were more in JFA. This explains the broader season in JFA, compared to CFA. Furthermore, unlike CFA, the P58N peaks are in April and May in JFA. This "late entry" of icebergs in the Labrador coast in the simulation JFA indicates that upstream environmental conditions have introduced differences in the influx of icebergs into the Labrador waters between the two simulations.

3.3.4 Differences in environmental conditions

The subplots (a), (b), (c), and (d) in figure 3.36 represent the differences of SST in CFA from the SST in JFA over the whole domain of research during the winter, spring, summer, and autumn, respectively. The ocean surface over the subpolar gyre is mostly warmer (by upto 4 °C) in the JRA55-do forced simulation compared to the CGRF forced simulation. Sea surface temperatures are also warmer in JFA for most of Baffin Bay during summer. Higher iceberg melting in the Labrador shelf break in JFA could be the reason behind the reduced I48N in this simulation (discussed later in details).

3.3.4.1. Local conditions

We compare the variability of the ocean surface and depth-averaged temperatures over the Labrador shelf mask with the I48N variability in figure 3.37. The spring SST anomaly (red line) averaged over the Labrador shelf mask along with the yearly total I48N anomaly (blue bars) for the entire period of the simulation JFA is shown in figure 3.37a. The spring depth (upper 100 meters) ocean temperature anomaly (red line) averaged over the Labrador shelf mask along with the yearly total I48N anomaly (blue bars) for the entire period of the simulation JFA is shown in figure 3.37b. The correlations over the years 1994-2017 are still very low and statistically non-significant in both cases.

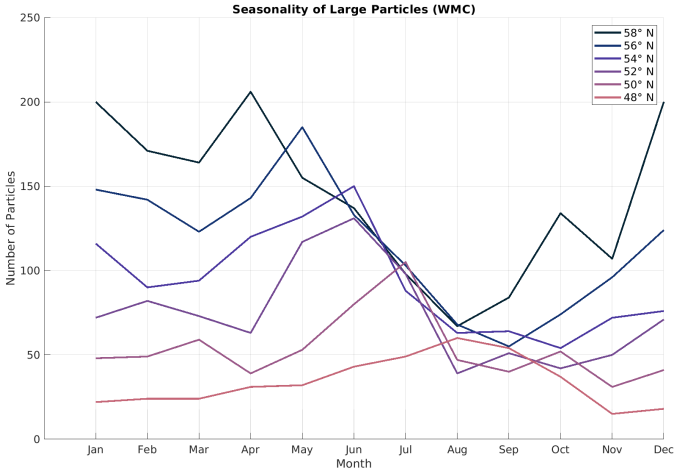

(a)

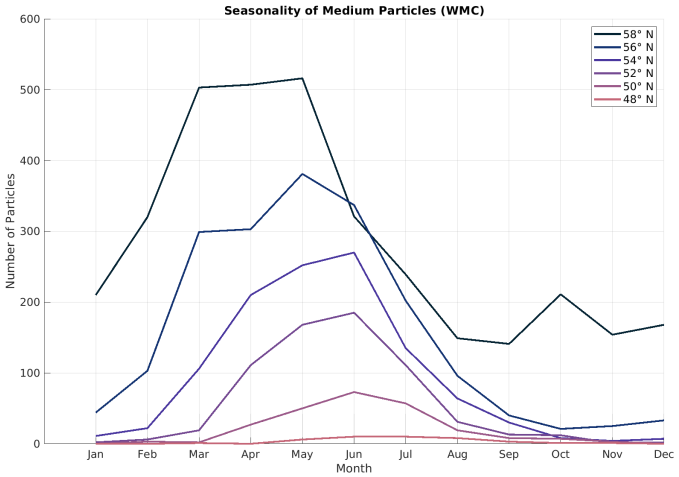

(b)

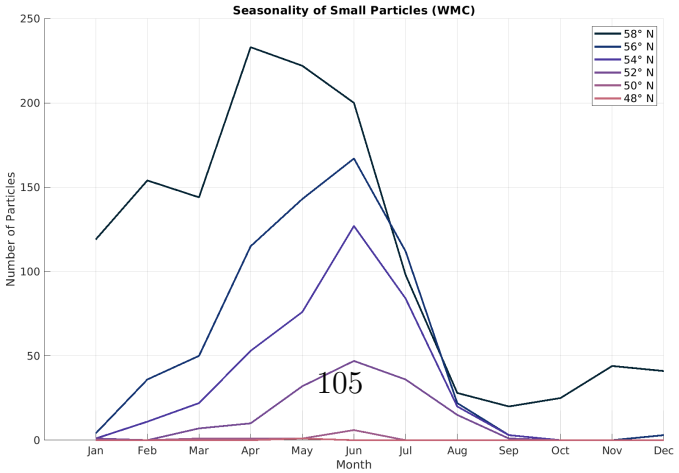

(c)

Figure 3.35: Seasonality of count of (a) large size-class, (b) medium size-class, and (c) small size-class particles reaching 58° N (darkest lines), 56° N, 54° N, 52° N, 50° N, and 48° N (lightest line) latitude in the simulation JFA.

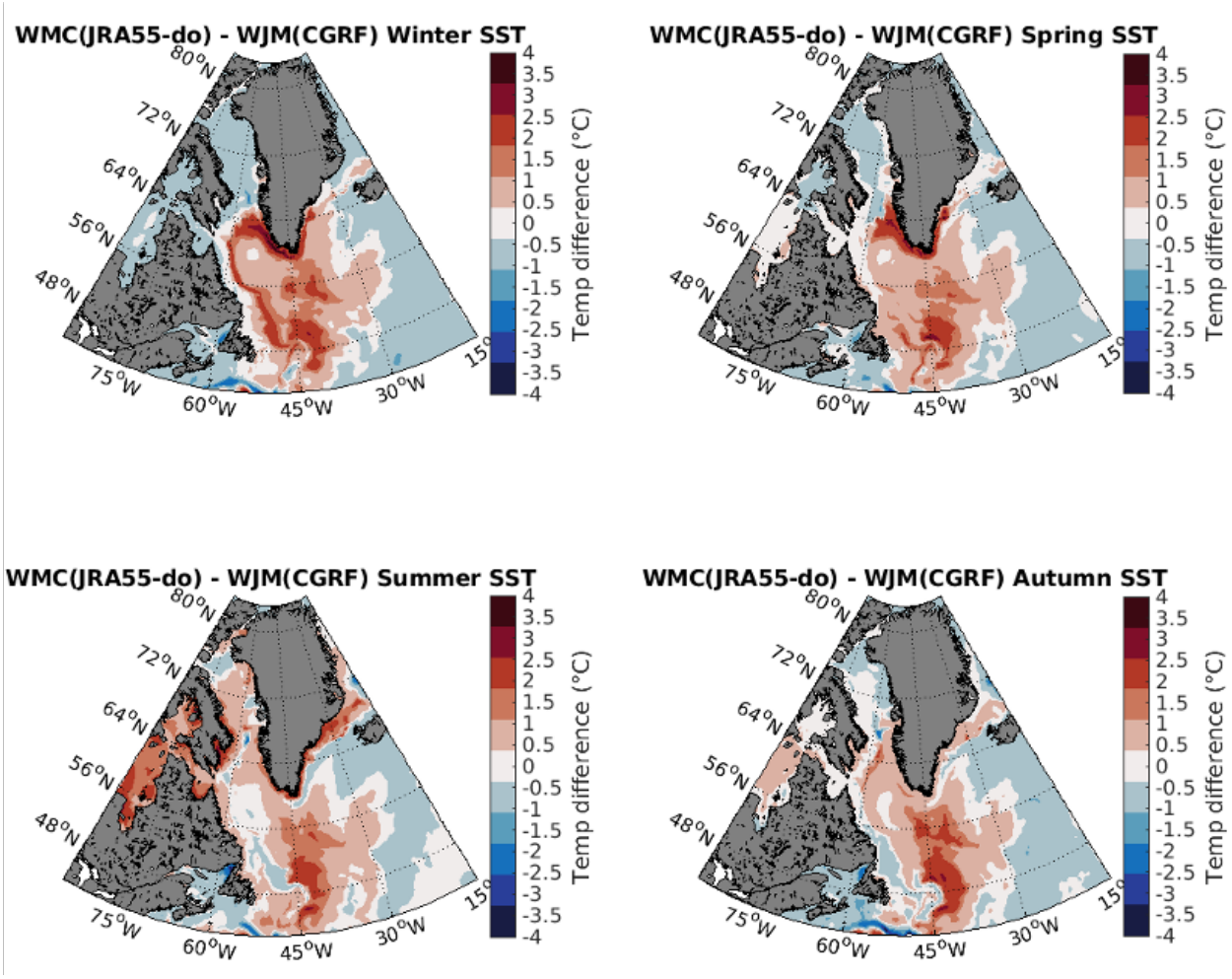

Figure 3.36: The SST in CFA subtracted from the SST in JFA averaged over (a) the winter months, (b) the spring months, (c) the summer months, and (d) the autumn months of the overlapping period of integration (2002 to 2017) over the whole domain of interest.

Moreover, the p-value improved as well, likely because it was calculated for a longer period of time. To test how the correlations evolved with time in the simulation JFA, we computed the correlations between I48N and both the temperature variables for the overlapping time period as well. The results are shown in the figure 3.38. While the relationship with spring SST over the Labrador shelf improved from a non-significant correlation (r = -0.21 p-value =

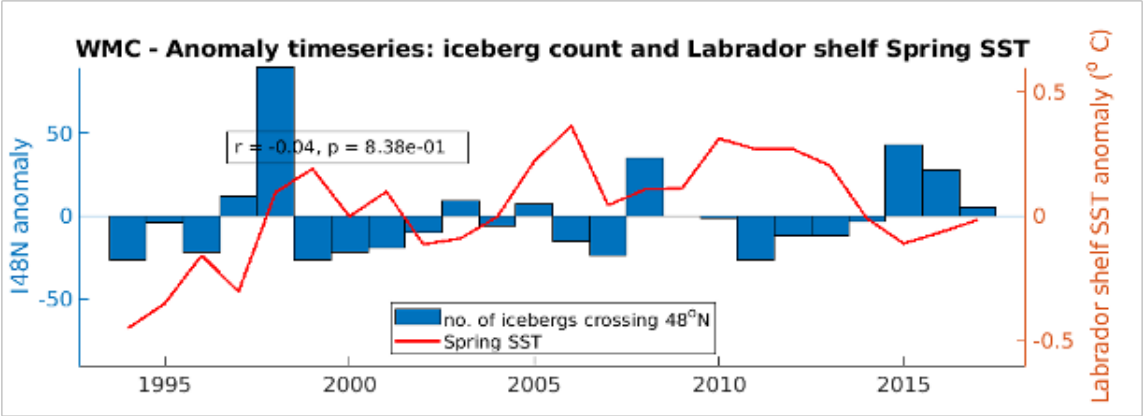

(a) JFA Spring SST over the Labrador shelf mask

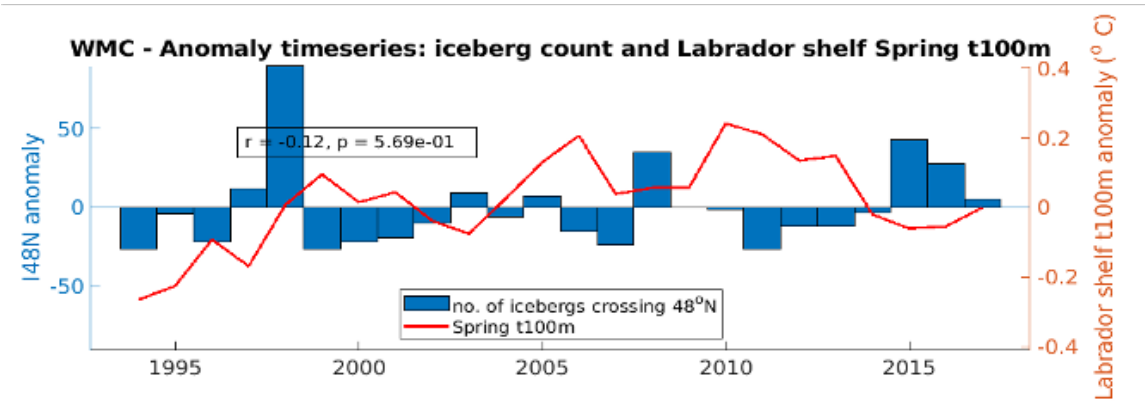

(b) JFA Spring depth-integrated (0-100 m)temperature over the Labrador shelf mask.

Figure 3.37: Anomaly of yearly (October to September) total number of icebergs crossing 48° N, with respect to the averaged over the period of simulation (blue bar) with (a) the anomaly in SST (in °C, red line), and (b) the anomaly in temperature (in °C, red line) averaged over the upper 100 meters of ocean over the Labrador shelf mask in the JFA simulation.

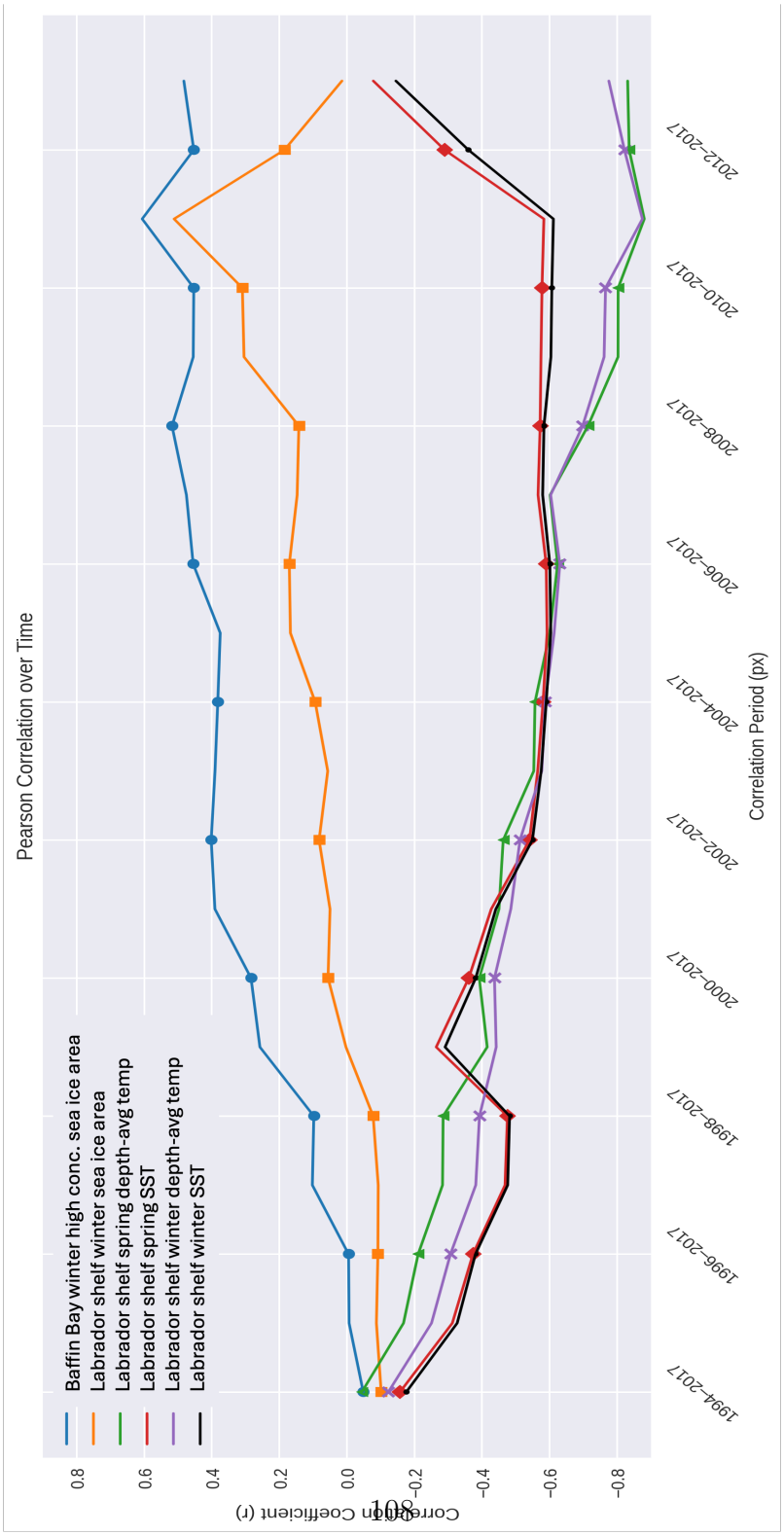

Figure 3.38: The modelled (JFA) time evolution of the correlations between the environmental factors and I48N for Labrador shelf winter SST (sstWinterTS), Labrador shelf spring SST (sstSpringTS), 100 m depth averaged spring ocean temperature over Labrador shelf (T100mSpringTS), 100 m depth averaged winter ocean temperature over Labrador shelf (T100mWinterTS), Winter sea ice area over Labrador shelf (LSsiaWinter), and Baffin Bay high concentration Winter sea ice area (siaWinterTS).

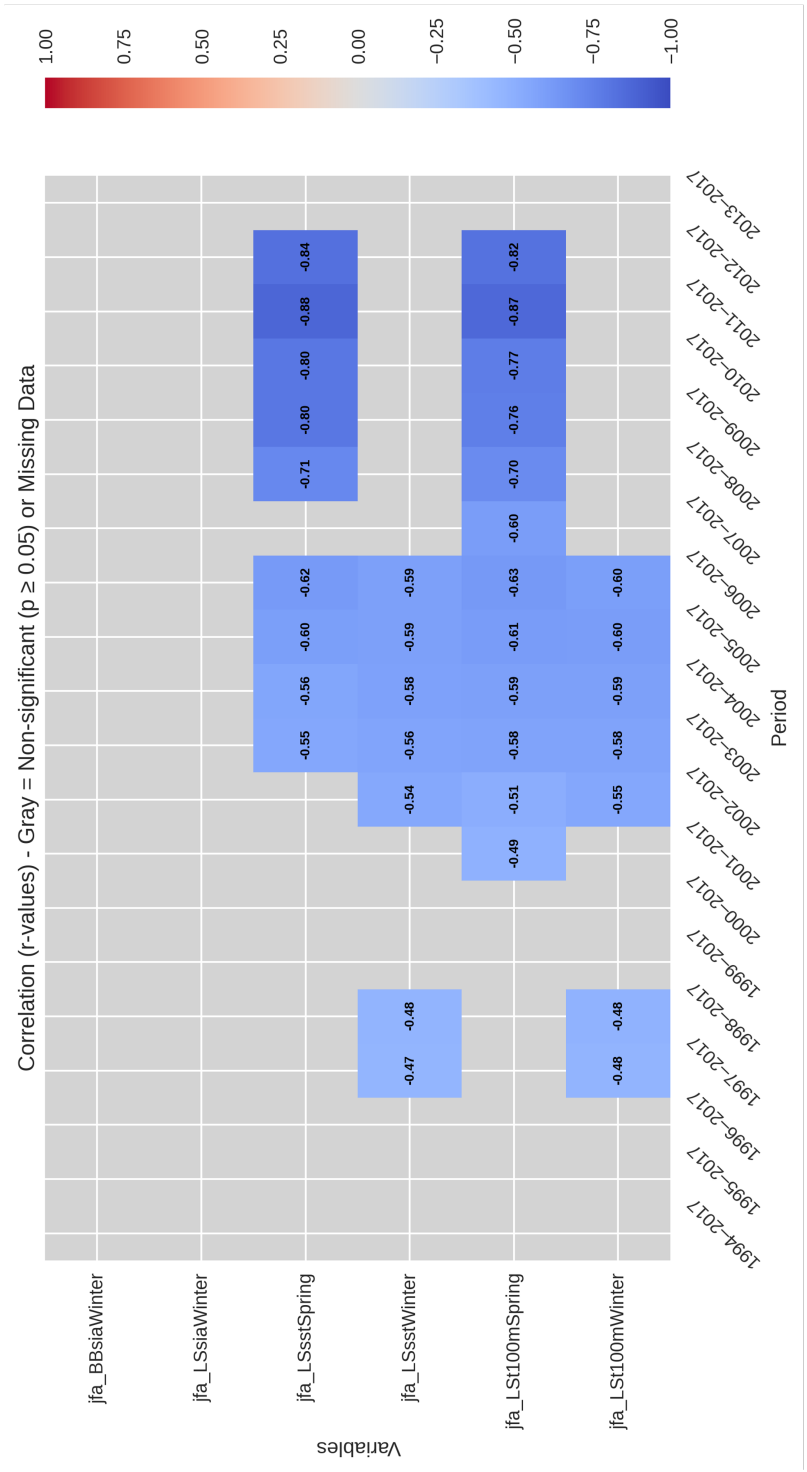

Figure 3.39: Heat map showing the modelled (JFA) Pearson correlation values (along with p-values) between the environmental factors and I48N for Labrador shelf winter SST (sstWinterTS), Labrador shelf spring SST (sstSpringTS), 100 m depth averaged spring ocean temperature over Labrador shelf (T100mSpringTS), 100 m depth averaged winter ocean temperature over Labrador shelf (T100mWinterTS), Winter sea ice area over Labrador shelf (LSsiaWinter), and Baffin Bay high concentration Winter sea ice area (siaWinterTS).

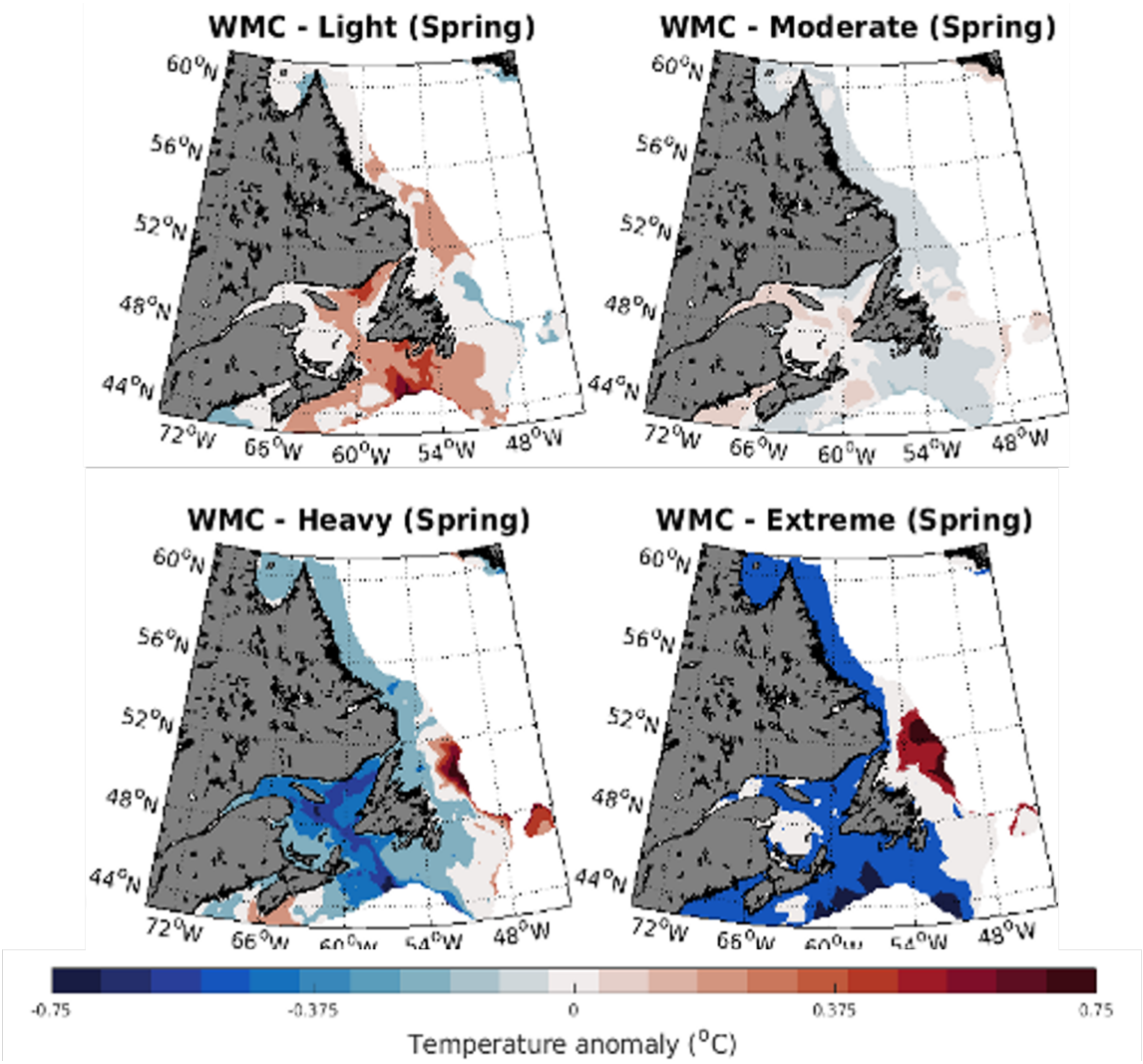

Figure 3.40: Spatial distribution of modelled (JFA) depth-integrated temperature anomaly (in °C) over the Labrador shelf over the spring months (April to June) across the severity classes.

0.3) for period 1996-2017 to a significant correlation (r = -0.56 p-value = 0.04) for period 2004-2017, the relationship with winter SST over the Labrador shelf improved from a non-significant correlation (r = -0.37 p-value = 0.9) for period 1996-2017 to a significant correlation (r = -0.58 p-value = 0.02) for period 2004-2017 (refer to figure 3.39).
Similarly, the relationship with spring depth-integrated temperature over the Labrador shelf mask improved from an insignificant correlation (r = -0.31 p-value = 0.1) for period 1996-2017 to a significant correlation (r = -0.60 p-value = 0.02) for period 2004-2017, the relationship with winter depth-integrated temperature over the Labrador shelf mask increased from an insignificant correlation (r = -0.38 p-value = 0.8) for period 1996-2017 to a significant correlation (r = -0.59 p-value = 0.02) for period 2004-2017. These statistically significant correlation values in the last 14 years of the JFA simulation are very close to the observed correlations between the Labrador shelf temperatures and the observed annual iceberg counts south of 48°N latitude. This suggests that the a longer simulation is necessary to have the representation of the relationships closer to near-realtime values (for reference, the observed values for spring SST, winter SST, spring vertically integrated temperature, and winter vertically integrated temperature were -0.59, -0.58, -0.66, and -0.63, respectively). These results prove that the initial iceberg field reduced the iceberg spin up time in the model, in turn improving the model representation of the correlations quicker. However, this also suggests that in order to have a more robust correlation analyses, we need a simulation with all the components fully adjusted and "in sync".

The four subplots of figure 3.40 represent the spatial anomalies of the depth-averaged temperature over the Labrador shelf mask for different iceberg season severity categories in the JFA simulation. Compared to the CFA simulation (figure 3.25), we see a smoother transition in ocean temperature from lighter severity classes to the heavier classes over almost the entire Labrador shelf mask, except for the outer Newfoundland region. In other words, in JFA the ocean over Labrador region is colder in springs when the iceberg season is heavier along the east coast of Canada. In figure 3.41, the timeseries of annual I48N anomaly (blue bars) and the anomalies in winter sea ice area on the Labrador shelf (red line) are plotted together for the years 1994 to 2017. No significant correlation (r = -0.06, p-value = 0.79) was found between the variables. To investigate if the correlation between I48N and this variable exhibits the similar characteristic of time-evolution as we found for the ocean temperature, we computed the correlations for different periods of JFA simulation. Indeed, we

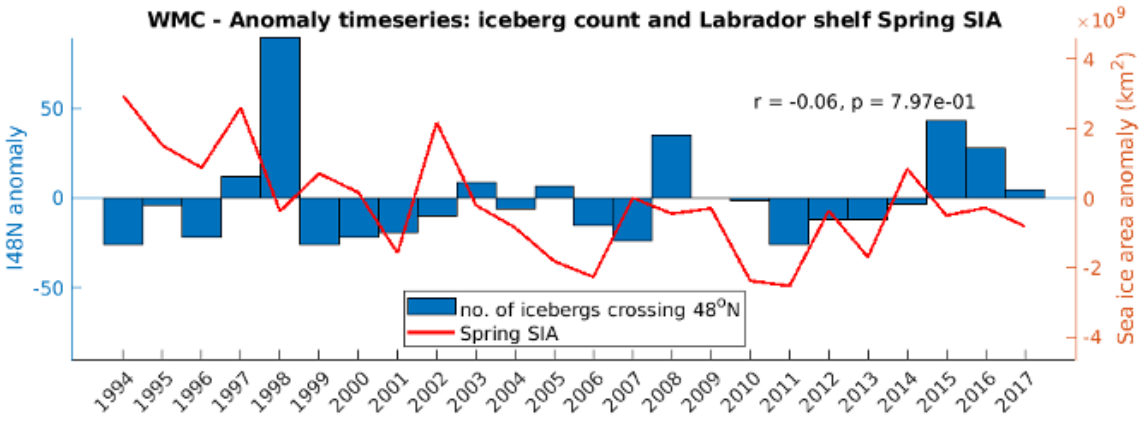

Figure 3.41: Anomaly of yearly (October to September) total number of icebergs crossing 48° N, with respect to average over the period of simulation (blue bar) with the anomaly of sea ice area (in km^2) over the Labrador shelf during the winter months (January to March) in the years 1994 to 2017 in the simulation JFA.

found that the interconnection improved from a statistically non-significant correlation value (r = -0.10, p-value = 0.6) during the period 1996-2017 to a statistically significant correlation value (r = 0.66, p-value = 0.01) during the period 2004-2017 in the JFA simulation. As explained in the section 3.1.2, one should expect a high positive correlation (observed correlation value: r = 0.78, p$\leq$ 0.05) between winter sea ice covered area over the Labrador shelf mask and the severity of the iceberg season. The improvement in JFA correlation between the sea ice area on the Labrador coast and I48 variability in the last 14 years of the simulation indicates that the impact of local sea ice condition during the months before iceberg season is well-depicted in the model once it is fully adjusted. The above findings verify the hypothesis made in [Rudnickas, Serumgard,] and [Cyr and Galbraith, 2021] that a colder ocean covered with more sea ice pre-conditions the location for heavier iceberg seasons. However, the I48N's inter-connection with the local ocean temperature improved closer to the observed correlations compared to that with the local ocean sea ice area. Comparing the spatial anomalies of the sea ice concentration over the Labrador shelf mask between CFA (figure 3.26) and JFA (figure 3.42) simulations, however, we found that the anomalies in the CFA simulation resemble the observations better. However, one should keep in mind that there was no heavy years at all in CFA, and only one extreme year on JFA. Therefore

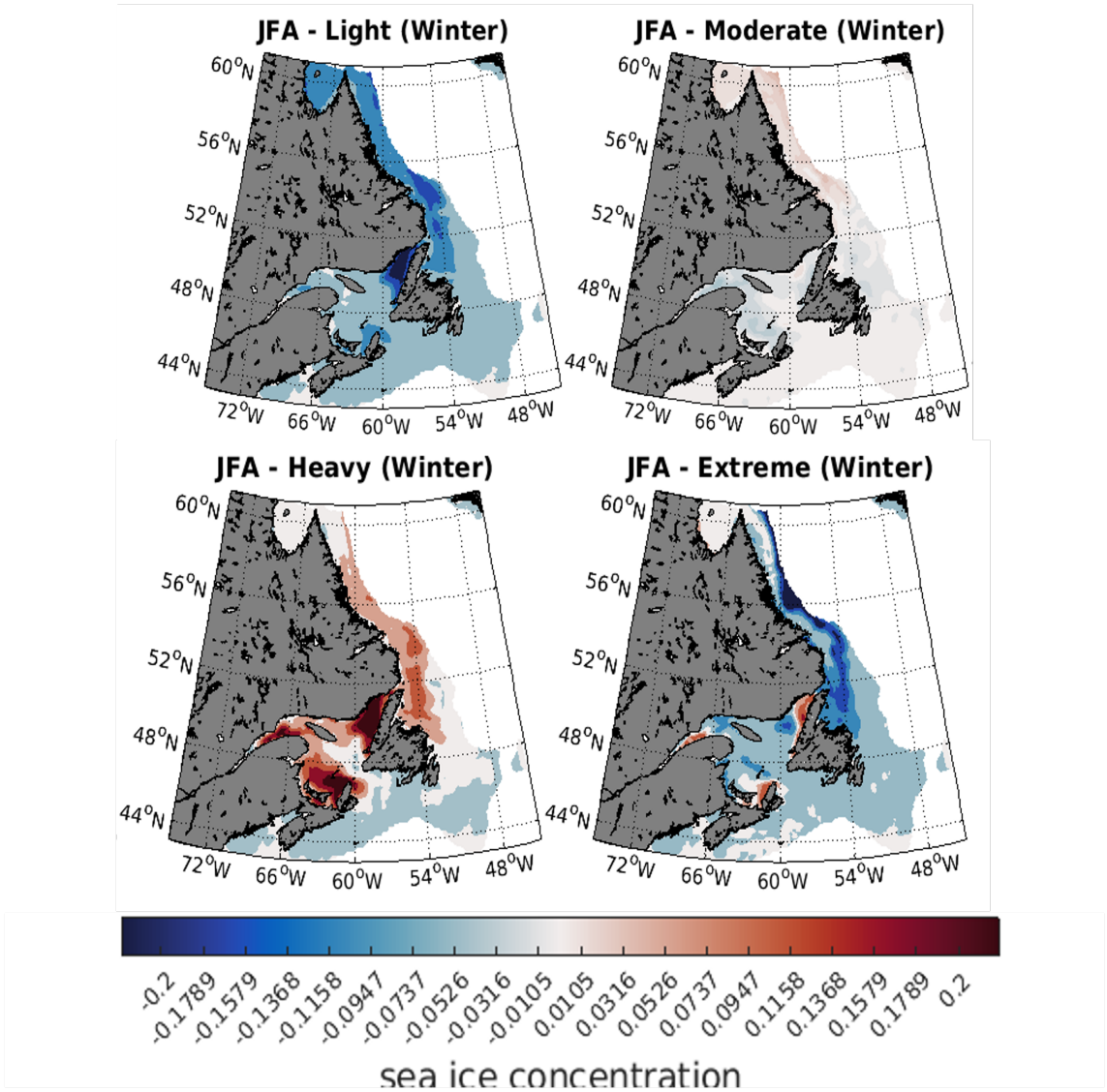

Figure 3.42: Spatial distribution of modelled (JFA) sea ice concentration anomaly on the Labrador shelf mask over the winter months (January to March) across the severity classes.

CFA	Particles			
	Large	Medium	Small	All
58 N	1174	2920	1484	5578
56 N	969	1702	704	3375
54 N	768	1085	423	2276
52 N	624	781	217	1622
50 N	504	428	62	994
48 N	323	154	16	493
JFA	Particles			
	Large	Medium	Small	All
58 N	1723	3439	1328	6490
56 N	1394	1884	655	3933
54 N	1119	1119	397	2635
52 N	889	661	149	1699
50 N	644	249	9	902
48 N	409	40	1	450

Figure 3.43: Table 4.2 shows the absolute numbers for different sized particles (column 2 to 4), for all particles (column 5) for the period 2002-2017.

CFA	Particles			
	Large	Medium	Small	All
58 N	100	100	100	100
56 N	82.5383305	58.2876712	47.4393531	60.5055575
54 N	65.4173765	37.1575342	28.5040431	40.8031553
52 N	53.1516184	26.7465753	14.6226415	29.0785228
50 N	42.9301533	14.6575342	4.17789757	17.8200072
48 N	27.5127768	5.2739726	1.07816712	8.8382933
JFA	Particles			
	Large	Medium	Small	All
58 N	100	100	100	100
56 N	80.9053976	54.7833673	49.3222892	60.6009245
54 N	64.9448636	32.5385286	29.8945783	40.6009245
52 N	51.5960534	19.2207037	11.2198795	26.1787365
50 N	37.3766686	7.24047688	0.67771084	13.8983051
48 N	23.7376669	1.16312882	0.0753012	6.93374422

Figure 3.44: Table 4.2 shows the percentage numbers for different sized particles (column 2 to 4), for all particles (column 5) for the period 2002-2017.

this analyses is not very robust.

To deduce how the variability in I48N is established along the Labrador coast, we first checked if the difference in I48N from CFA to JFA is established before or after particles arrive at the Labrador coast. We selected six latitudes, every two degrees of latitude between 58°N to 48°N along the Labrador coast. To investigate how quickly the particles/icebergs are deteriorating in the two simulations (CFA in the upper block, and JFA in the lower block of the table) we compared the counts in both the simulations in the table 3.43. The counts of large and the medium particles entering the northern Labrador coast at 58° N in JFA simulation is more than those in CFA simulation as expected (since during first few months, CFA did not have any iceberg production). However, it is noticeable that the small iceberg count at 58° N is larger in CFA. That suggests that more smaller particles in JFA are deteriorated upstream compared to in CFA. We are going to test this hypothesis in later section. Considering particle counts at 58°N to be 100%, we compared the percentages of particles across those above-mentioned six latitudes along the Labrador coast in table shown in 3.44 (second to fifth columns) for 2002 to 2017 for both the simulations. This suggests that the medium and small particles melt faster (i.e., disappear farther north), due to the warmer ocean temperatures in JFA is more on the dissipation of the icebergs in JFA, compared to CFA.

On the other hand, fewer small particles are crossing 58°N in JFA simulation compared to that in CFA simulation for the time period of 2002 to 2017. And, even though the total particle counts entering Labrador coast is larger in JFA, a much smaller number of them make it to 48°N. Among 3439 medium particles, only 40 survived as far south as 48°N in JFA. That points out towards two possibilities: (i) the icebergs in JFA are melting quicker in the Labrador coast before reaching 48°N, compared to icebergs in CFA, and/or (ii) the icebergs in JFA arrive at 58°N with less mass compared to icebergs in CFA. To test the first hypothesis, we plotted the iceberg mass loss along the Labrador coast in figure 3.45. The left, middle, and right subplots in this figure show the total mass of the large, medium, and small icebergs reaching the six latitudes from 58° N to 48° N for JFA (red lines) and CFA (blue lines). In general, the mass loss is steeper in the JFA than in CFA. For example, starting with almost same amount of mass, medium sized icebergs are reaching 48° N latitude with a smaller amount of mass in JFA compared to CFA. Also, starting with approximately 6.25×10^{13} kilograms more mass than the CFA simulation, the JFA simulation had the same amount of

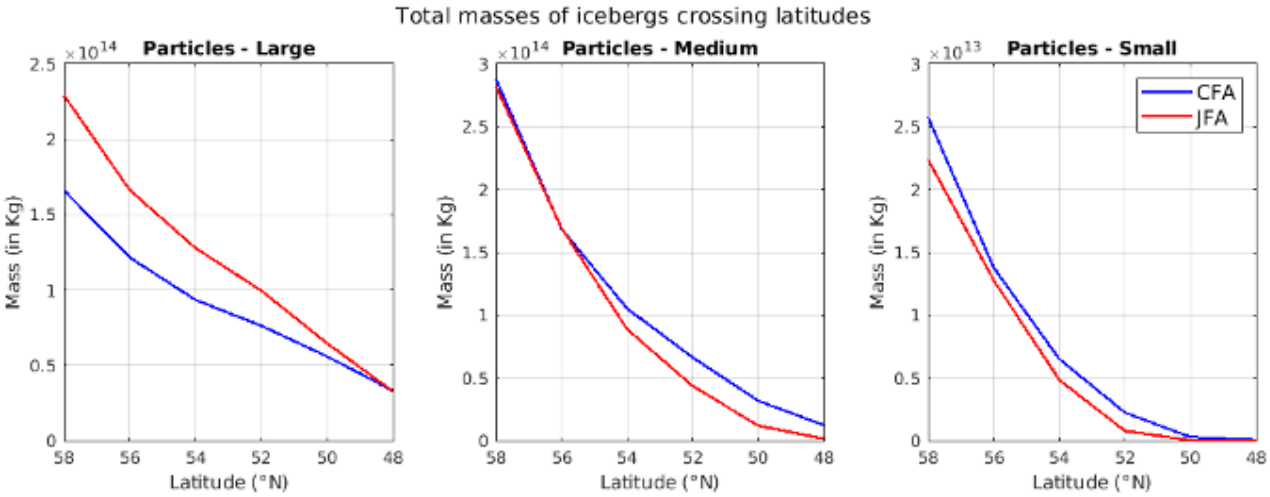

Figure 3.45: Total mass (in kg) of large, medium, and small icebergs crossing the six latitudes (i.e. 58°, 56°, 54°, 52°, 50°, and 48° north) along the Labrador shelf in JFA (red line), and CFA (blue line) simulations.

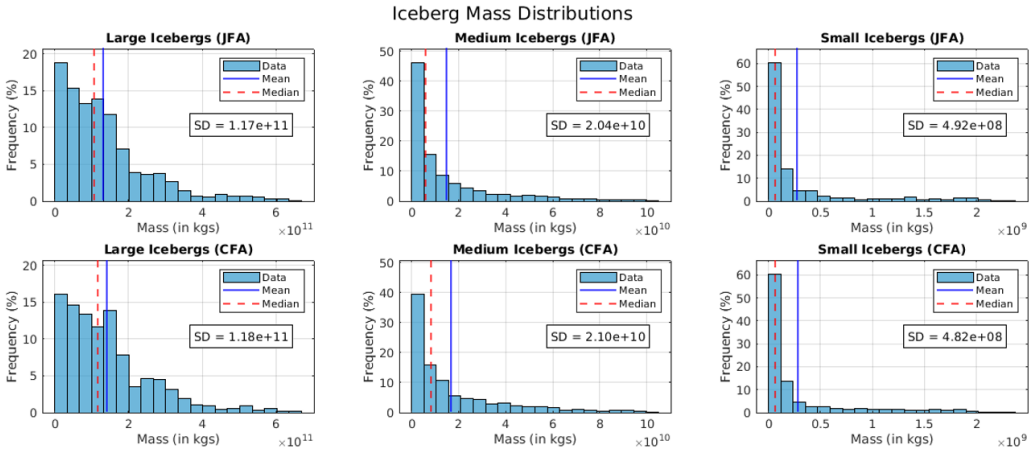

Figure 3.46: Histograms of mass distribution of large (left column), medium (middle column), and small (right column) particles at 58° N in the JFA (top row) and in the CFA (bottom row) simulations respectively. The blue solid lines and the red dashed lines represent the mean, and the median of the corresponding data. SD = standard deviation is shown in the corresponding subplot.

iceberg mass reaching 48° N as CFA. This agrees with [Cyr and Galbraith, 2021] that a colder ocean pre-conditions the east Canadian coast for a heavier iceberg season. Therefore, it is reasonable to consider the local ocean temperature as a governing factor behind the variability in I48N.

3.3.4.2. Remote conditions

Now, the question arises: is the striking difference between the count of icebergs in the two simulations established only along the Labrador coast? Or do processes farther north contribute to it as well? To investigate it, we analyzed the middle row of figure 3.45 with the *Medium* column of the table 3.43 together. In figure 3.45, it is noticeable that the total mass is very close to each other, while, in the table 3.43 we see that the medium particle counts entering the northern Labrador coast is larger in JFA compared to that in CFA. This indicates that the icebergs lost more mass before reaching 58° N latitude in JFA compared to the icebergs in CFA. In fact, the average masses of the large, medium, and small particles entering the northern Labrador coast in CFA (1.41×10^{11}, 1.70×10^{10}, and 2.84×10^{8} kg respectively) are larger than their counterparts in JFA (1.33×10^{11}, 1.48×10^{10}, and 2.80×10^{8} kg respectively). In figure 3.46, the distribution of the masses of all the large (left column), medium (middle column), and small (right column) particle crossing 58° N latitude for the period 2002 to 2017 in the simulations JFA (top row) and CFA (bottom row) are shown. The blue and the dashed red lines in each subplot represent the mean and the median, respectively, for the corresponding data. While, the medians of the masses of the small particles in JFA (7.01×10^{7} kg) and CFA (6.98×10^{7} kg) are similar to each other, the medians of the large and the medium particles are not. For example, the median of the medium size particles in JFA is 6.26×10^{9} kg, while it is 8.52×10^{9} kg in CFA. That is mass of 50% of the medium particles reaching 58° N in JFA is much lower than those in CFA. This proves that the depleted I48N in JFA simulations is not the result of only the melting of icebergs in the warmer ocean along the Labrador coast, but there must be upstream processes causing the icebergs to lose more mass before entering the northern Labrador coast in this simulation compared to the CFA simulation.

For the environmental conditions in the northern part of the iceberg trajectories, we look at Baffin Bay. In figure 3.47, the Baffin Bay average SST in CFA is subtracted from the average SST in JFA for (a) winter, (b) spring, (c) summer, and (d) autumn months. Most of Baffin Bay, especially the western part of it, is

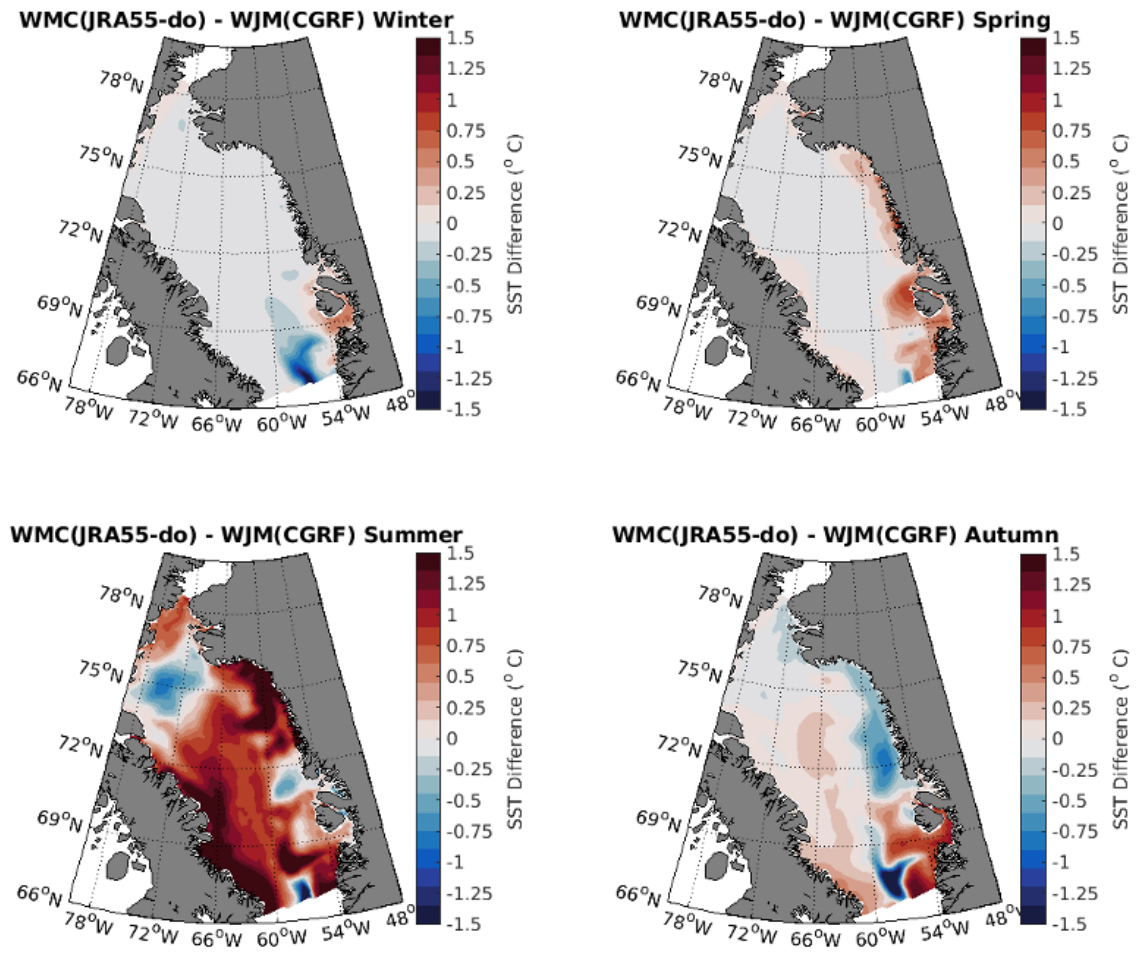

Figure 3.47: The SST in CFA subtracted from the SST in JFA averaged over (a) the winter months, (b) the spring months, (c) the summer months, and (d) the autumn months of the overlapping period of integration (2002 to 2017) over Baffin Bay.

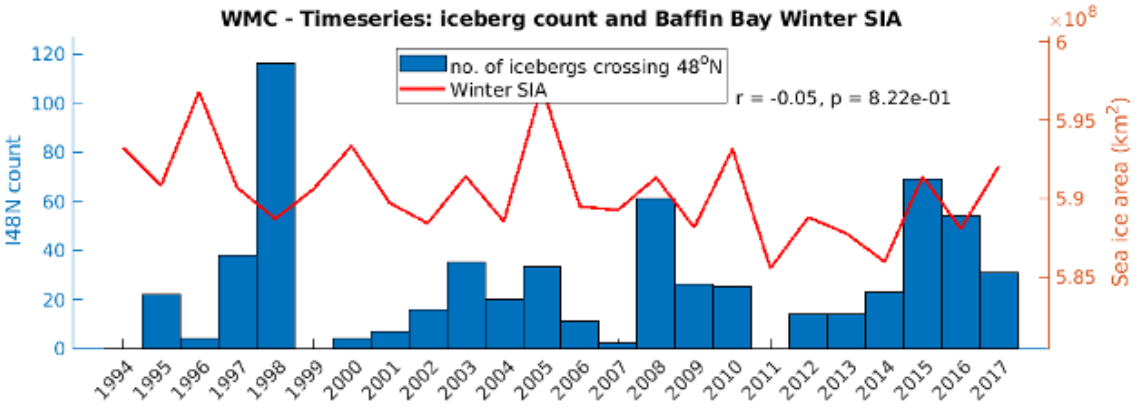

Figure 3.48: Modelled (JFA) yearly total iceberg count (blue bar) and the area (in km^2) of Baffin Bay covered with sea ice with high concentration ($\geq$ 90%) in the winter months (January to March) in the simulation JFA.

1.25 to 1.5 °C warmer in JFA during summer months. The positive anomalies in the west coast of Greenland during the spring and autumn months are also prominent. Figure 3.48 shows the timeseries of annual total I48N (blue bars) with the total area covered (in km^2) by high concentration ($\geq$ 90%) sea ice (red line) for the period 1994 to 2017. Neither any statistically significant correlation, nor any clear similarity between the variabilities in annual total I48N and in winter high concentration sea ice covered area in Baffin Bay were found. No reasonable differences in the general spatial pattern of ice coverage was found between CFA and JFA (refer to figure 4.6). Nor any was found in growth and retreat timings of Baffin Bay sea ice between the two runs (not shown in figures). The four sub-figures in 3.49 show the anomalies of high concentration ($\geq$ 90%) sea ice during the years of different iceberg season severity classes with respect to the mean winter high concentration ($\geq$ 90%) sea ice averaged over the period of simulation (1994-2017). We see a counter-intuitive pattern here (different from CFA), i.e. heavier sea ice condition during the winters before the lighter iceberg season and less severe sea ice condition before the heavier seasons. However, the correlation increased drastically from a statistically non-significant correlation value (r = -0.005, p-value = 9.8×10^{-1}) when we computed it for a longer period (1996 to 2017) to a statistically significant correlation value (r = 0.38, p-value = 1.77×10^{-3}) when we computed it for last 14 years of the simulation (2004-2017). Compared to the corresponding correlations in the CFA simulation, this

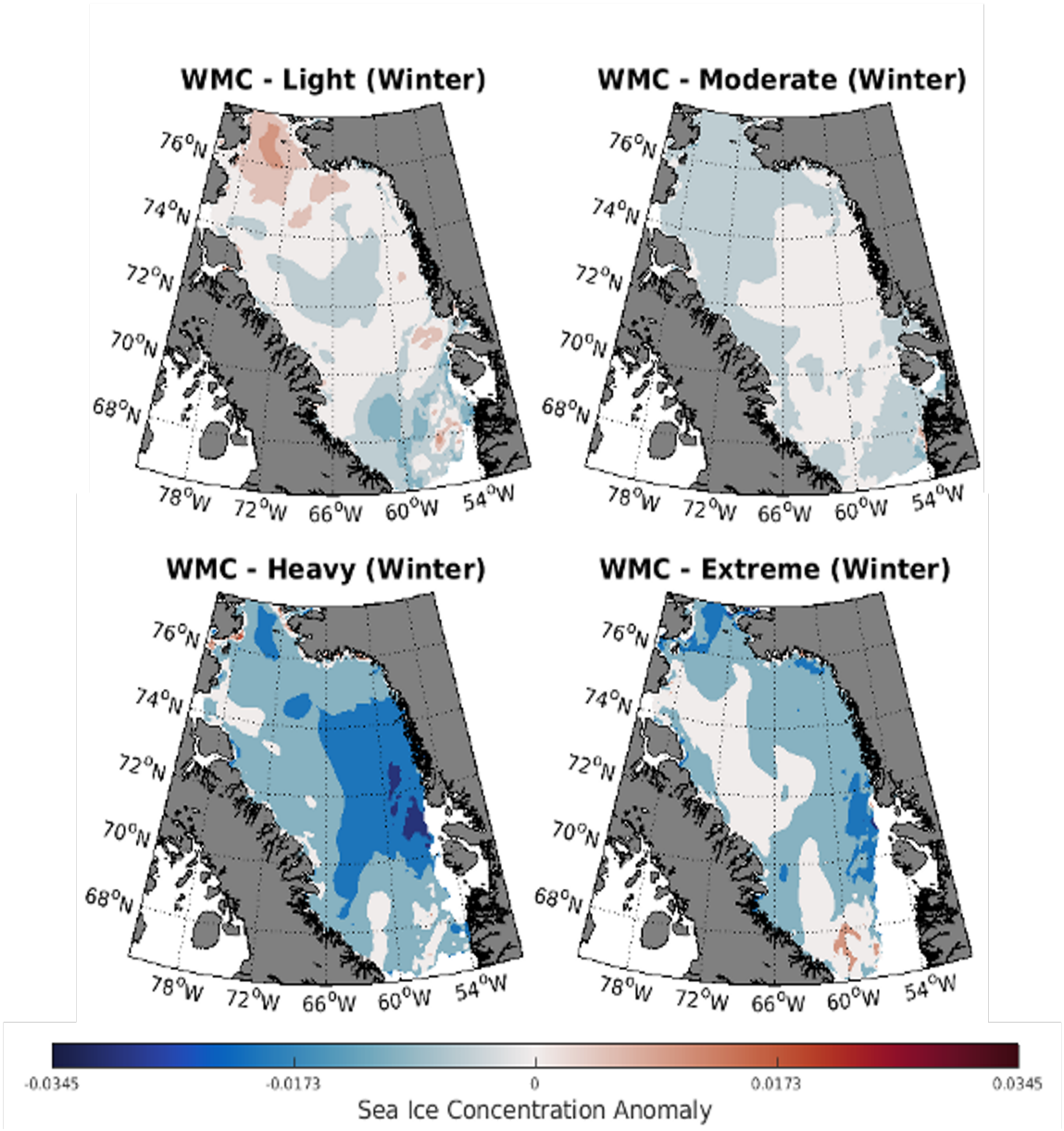

Figure 3.49: Spatial distribution of anomalies in the modelled (JFA) sea ice with high concentration ($\geq 90\%$) across the severity classes.

improvement establishes that the longer simulation provides the relationships between the Baffin Bay sea ice condition and the severity of the iceberg season along the east Canadian coast more time to stabilize. That makes the model representation of its influences on I48N more realistic in turn.

Differences in presence of particles in the model gird cells

Another factor to be considered when looking at the upstream environmental conditions is that, even if temperature and sea ice were very similar between the simulations, icebergs can be traveling through different paths and, therefore, be exposed to different conditions (for example, icebergs drifting mostly in a cold ocean current versus in a warmer one). We counted the number of particles crossing every grid cell in the model domain for both simulations for the years 2002 to 2017 and then subtracted the CFA outcome from JFA. The result is presented in figure 3.50. The CFA simulation is just starting with no icebergs, while JFA was on its tenth year of integration and had an iceberg-populated ocean and with "bins" of the different size classes partially filled with ice. There were 1653 more particles in the JFA simulation (total 35678 particles) than in the CFA simulation (total 34025 particles) during this period. Nonetheless, the blue patches in the figure mean that more particles crossed those grid cells in CFA compared to JFA. The two areas circled with numbers in figure 3.50 are investigated further.

East coast of Greenland: We see a blue patch all along the southeastern coast of Greenland (marked by area 1 circled in magenta in figure 3.50) which means that less particles crossed those grid cells in JFA simulation compared to CFA. To investigate the reason behind it, we explored the differences in wind stress between the two simulations. Figures 3.51 (a), (b), (c), and (d) show the difference (JFA-CFA) of the eastward component of the wind stress between the simulations averaged over the winter, spring, summer, and autumn months, respectively, for the years 2002 to 2017. The red patch along the southeastern Greenland coast all the way to the southern tip of Greenland (in all seasons) mean that there is a stronger eastward or weaker westward wind stress (by 0.01 to 0.02 N/m^2) in the JFA simulation compared to CFA. This suggests that the icebergs calved from the southeast Greenland sources in the simulation JFA could be pushed more offshore by the wind and drift away from the East Greenland Current (EGC).Figure 4.10 also shows the directions of the wind stress during the spring months in the JFA and the CFA simulations,

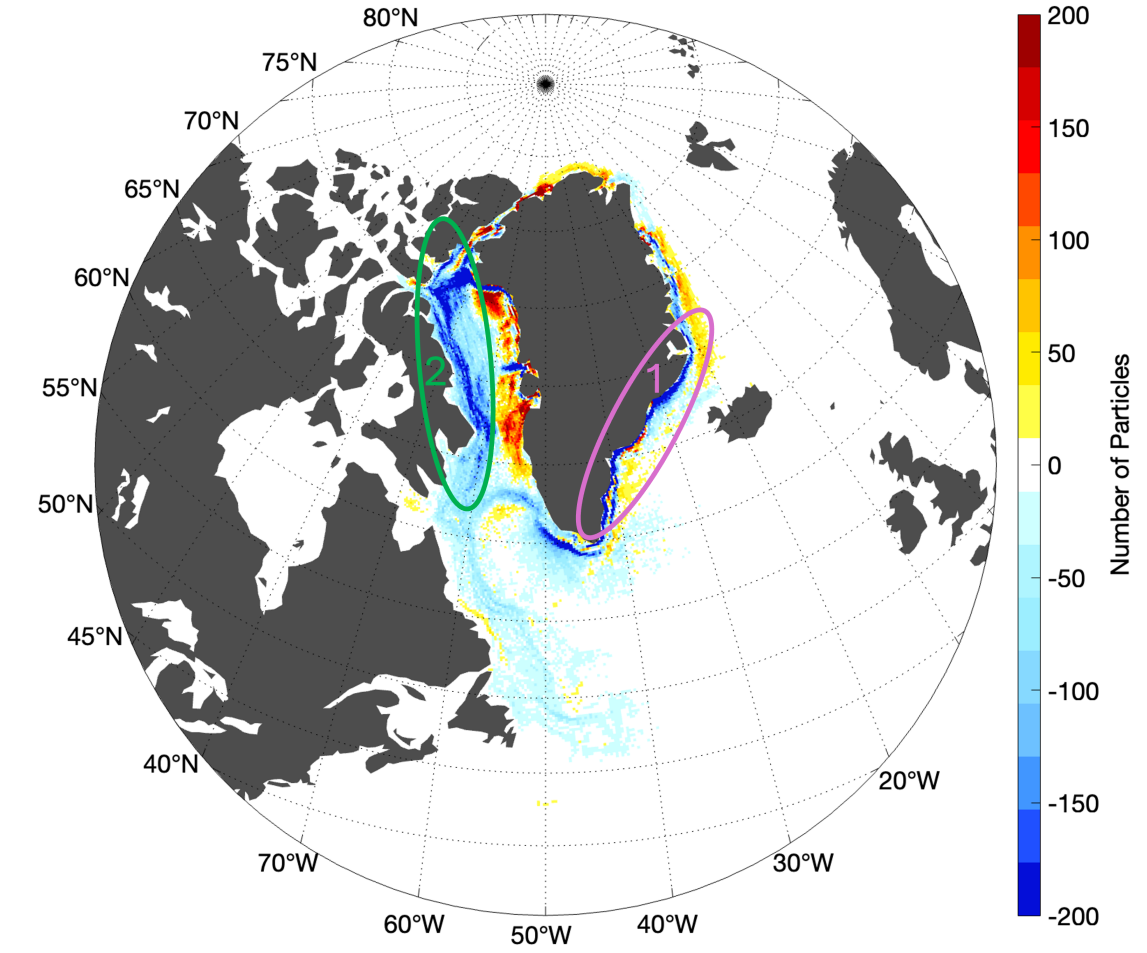

Figure 3.50: Differences in number of particles crossing every grid point of the domain between CFA and JFA from 2002 to 2017.

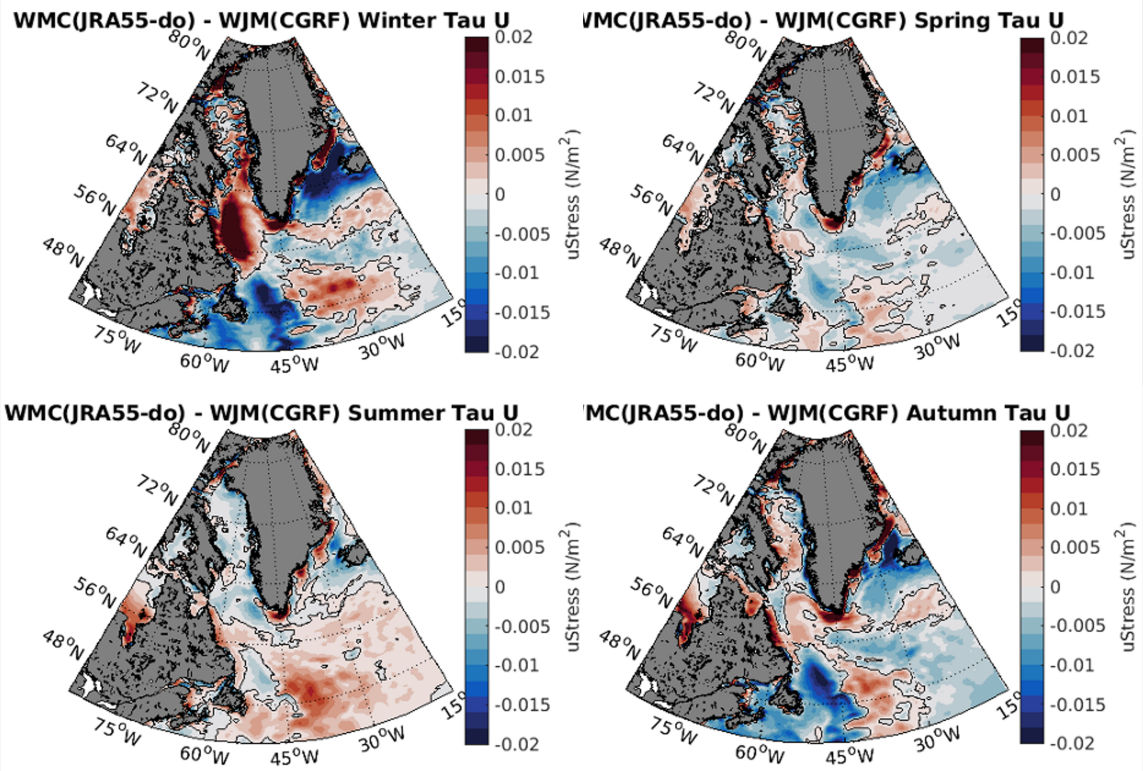

Figure 3.51: The eastward component of wind stress in CFA were subtracted from the eastward component of wind stress in JFA. Those differences averaged over winter, spring months,summer months, and autumn months of the year 2002 to 2017 are shown in (a), (b), (c), and (d) respectively over the whole domain of interest.

respectively. The length of the arrows show the magnitude of the vectors. Along the southeastern coast of Greenland, we see more southwestward stress with larger magnitude in CFA simulation, which could be the reason behind the higher number of CFA particles along the southeastern coast of Greenland and at the southern tip of Greenland. However, in the CFA simulation, only 9% (46 out of 493) of the total number of particles reaching 48° N for period 2002-2017 originated from the Southeast Greenland calving sector (refer to figure 4.7), whereas, in JFA, it increased to 16% (74 out of 450). Therefore, the lack in counts of particles originating from southeastern calving sites in JFA simulation does not explain the lack in particles counts arriving at 48° N completely.

Baffin Island shelf: Of 450 particles reaching 48° N in JFA, 176 came from the Northwest sector, and 114 came from central West (refer to figure 2.5). And, of 493 particles reaching 48° N in CFA, 258 came from the Northwest sector, and 104 came from central West. Many of the icebergs calved from these two largest contributing sectors (figure 4.7) follow the Baffin Bay gyre circulation which consists of the northward WGC and then the southward BIC. Therefore, it is important that we investigate the reason behind the blue patch over the west side of Baffin Bay marked with green circle (area 2) in figure 3.50. We hypothesized that the differences in several environmental factors could cause that blue patch. For instance, (i) ocean temperature, (ii) wind stress, (iii) Sea Surface Height (SSH). We investigated how the above-mentioned factors vary in the two simulations. To test if the difference in icebergs' distribution along Baffin Island coast between the two simulations was caused by the generally warmer temperatures in JFA (see figure 3.36), we plotted the spatial distribution of difference in Baffin Bay sea surface temperature between the simulations (i.e., SST in JFA - SST in CFA) for the four seasons for the years 2002-to-2017. We see temperature differences upto 1.5 °C between JFA and CFA over the Baffin Island shelf and Northwest/Southwest Greenland during the summer months. To further investigate if a warmer ocean was melting more particles (especially particles from small size classes) in JFA compared to those in CFA, we analyzed the average iceberg melt rates for both simulations (figure 3.52). Although melting rates are actually lower for JFA over the Baffin Island shelf, melting is higher in JFA compared to CFA along the west Greenland coast. This could cause many particles of Northwest origin melt quickly after calving. This finding suggest that this warmer temperature might be a reason behind a smaller particle count from Northwest sector reaching 48° N in JFA. Therefore, it can be inferred that the temperature of the ocean water in Baffin Bay is a significant

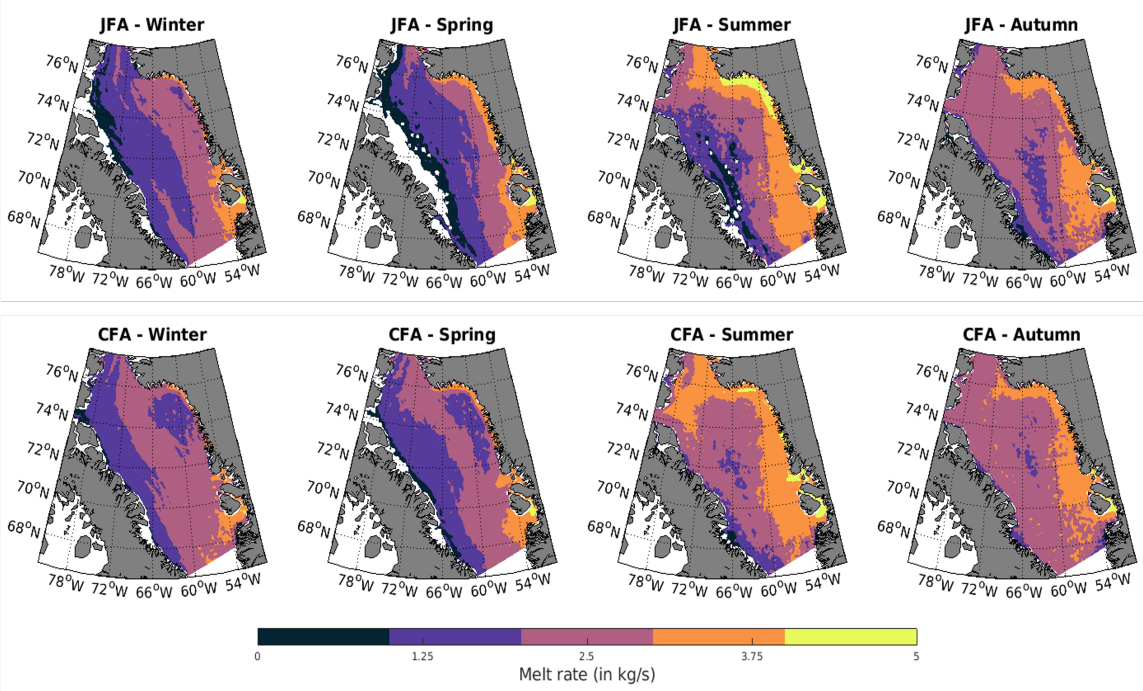

Figure 3.52: The logarithm (power of 10) of rate of iceberg melt in JFA (top row), and in CFA (bottom row) for the seasons Winter, Spring, Summer, and Autumn, averaged over the period 2004-2017.

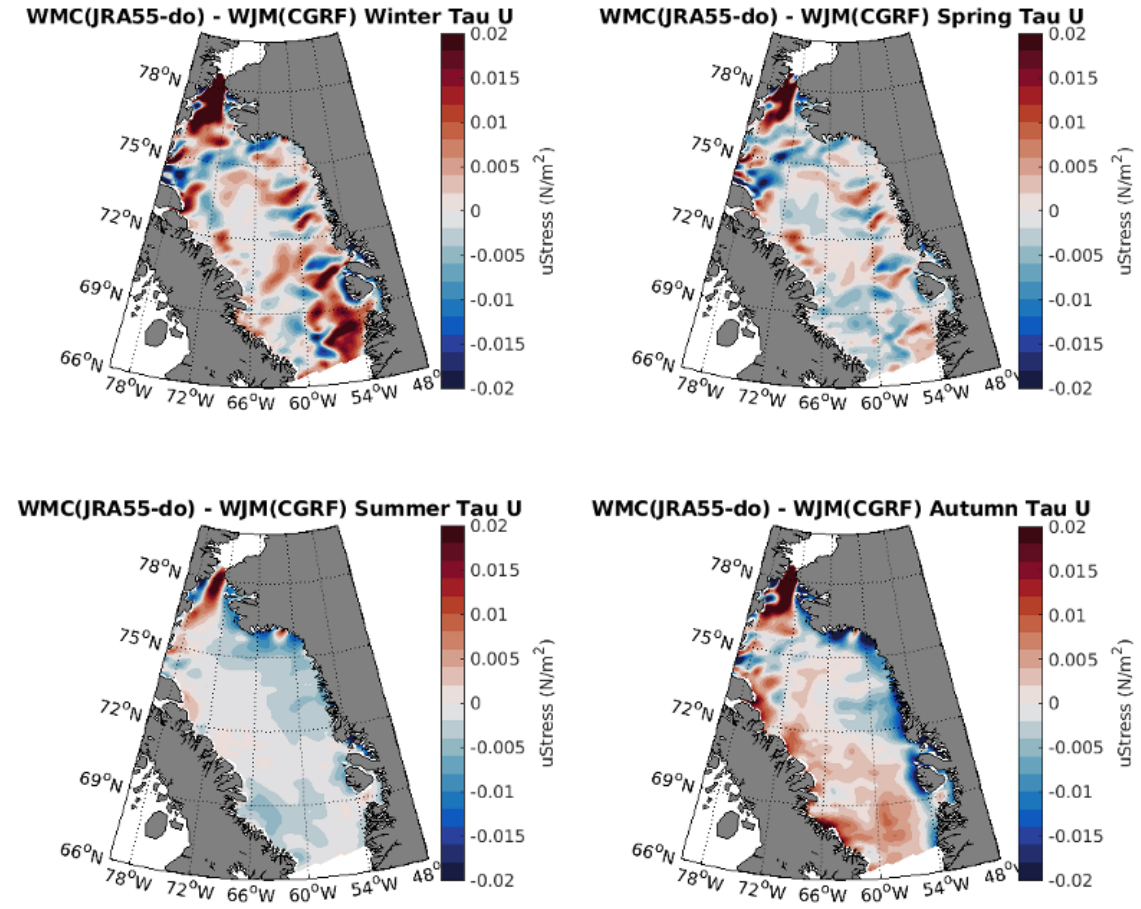

Figure 3.53: The eastward wind component values in CFA subtracted from the zonal wind component value in JFA averaged over (a) the winter months, (b) the spring months, (c) the summer months, and (d) the autumn months of the overlapping period of integration (2002 to 2017) over the Baffin Bay.

factor in determining the iceberg influx in the east coast of Canada. We see a sudden negative value in JFA - CFA particle counts (blue patch marked by green circle) in figure 3.50 south of Smith Sound (refer to figure 1.2), which is retained throughout the Baffin Island shelf. In order to find out the possible reason that caused this abrupt depletion in JFA particles counts, we analyzed difference in the wind stress in that region between the two simulations. Figure 3.53 shows the differences of the eastward wind stress ($\vec{\tau}_U$) between the two simulations (JFA - CFA) for all four seasons over Baffin Bay for the years 2002 to 2017. In all

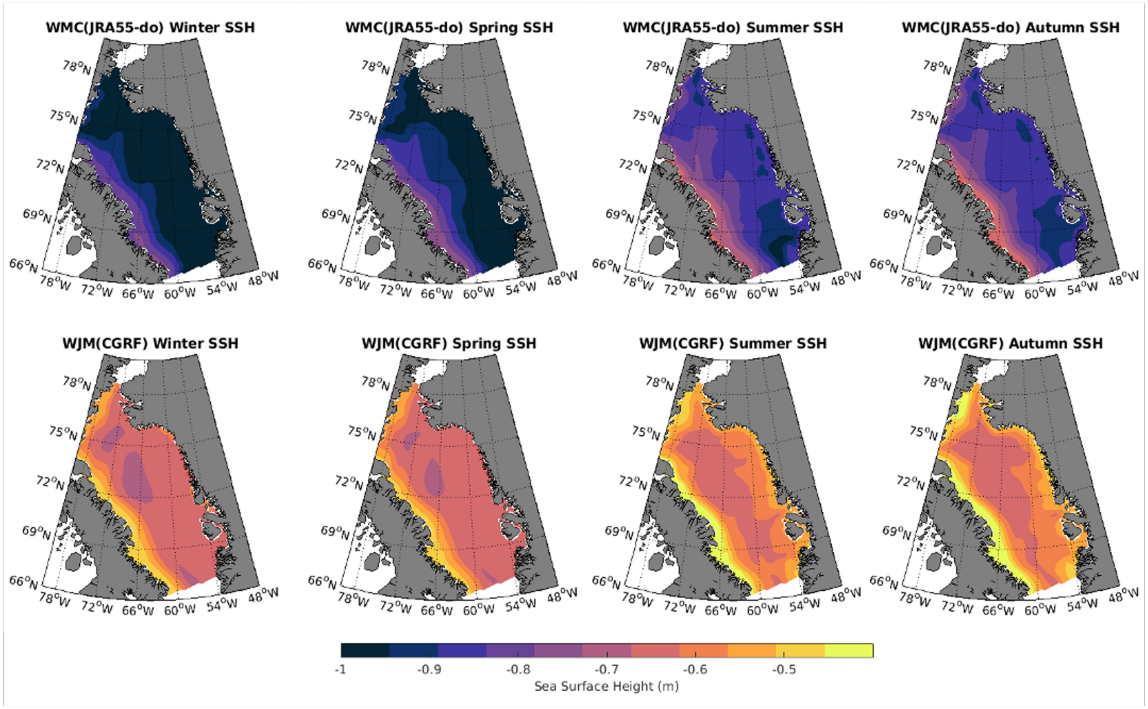

Figure 3.54: Upper panel: Spatial distribution of sea surface height averaged over (a) winter, (b) spring, (c) summer, and (d) autumn months in the simulation JFA. Lower panel: Spatial distribution of winter sea surface height averaged over (e) winter, (f) spring, (g) summer, and (h) autumn months in the simulation CFA.

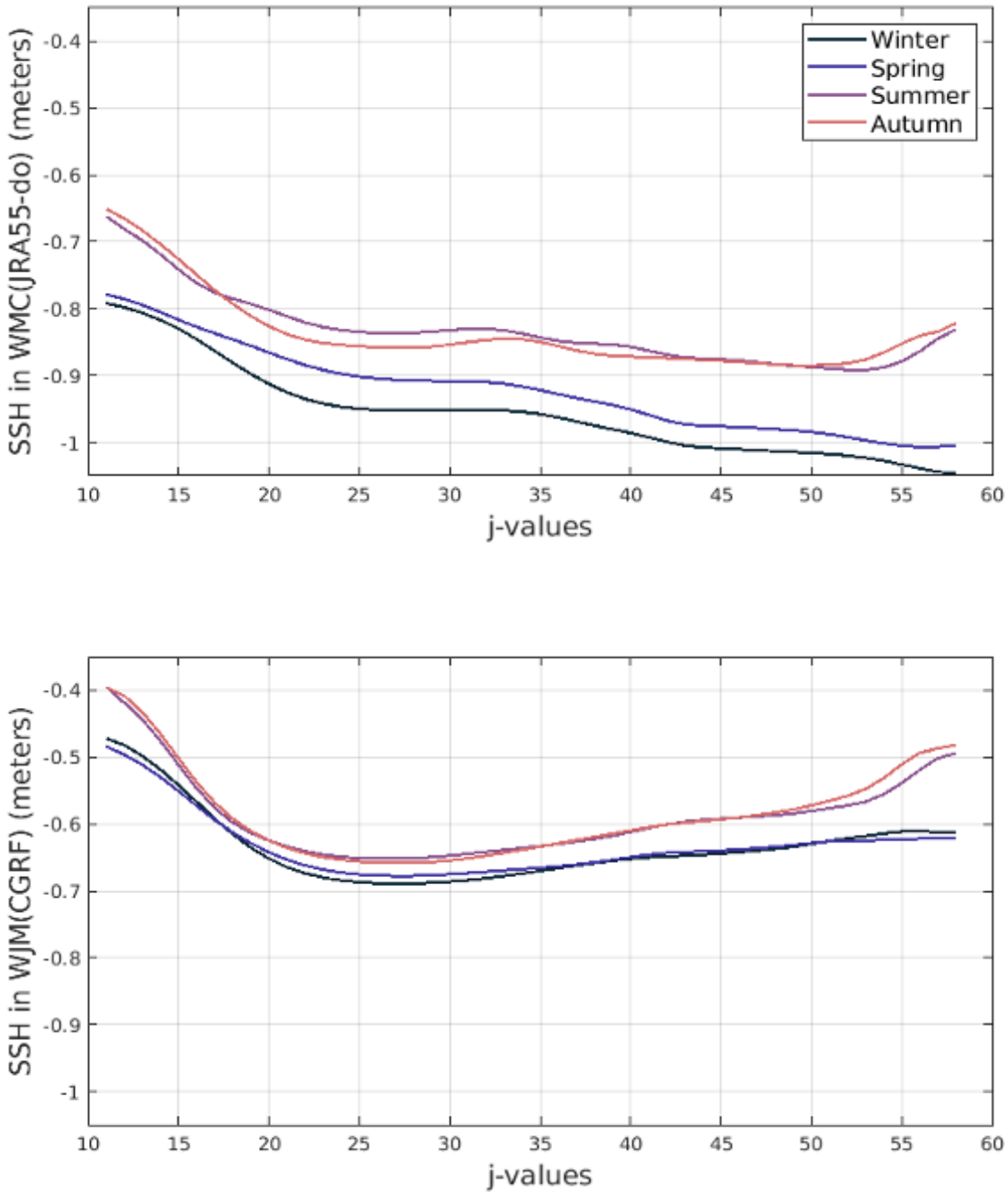

Figure 3.55: Seasonal average of SSH in JFA (in the upper panel), and in CFA (in the lower panel) along the dashed red line across Baffin Bay shown in the map 1.3.

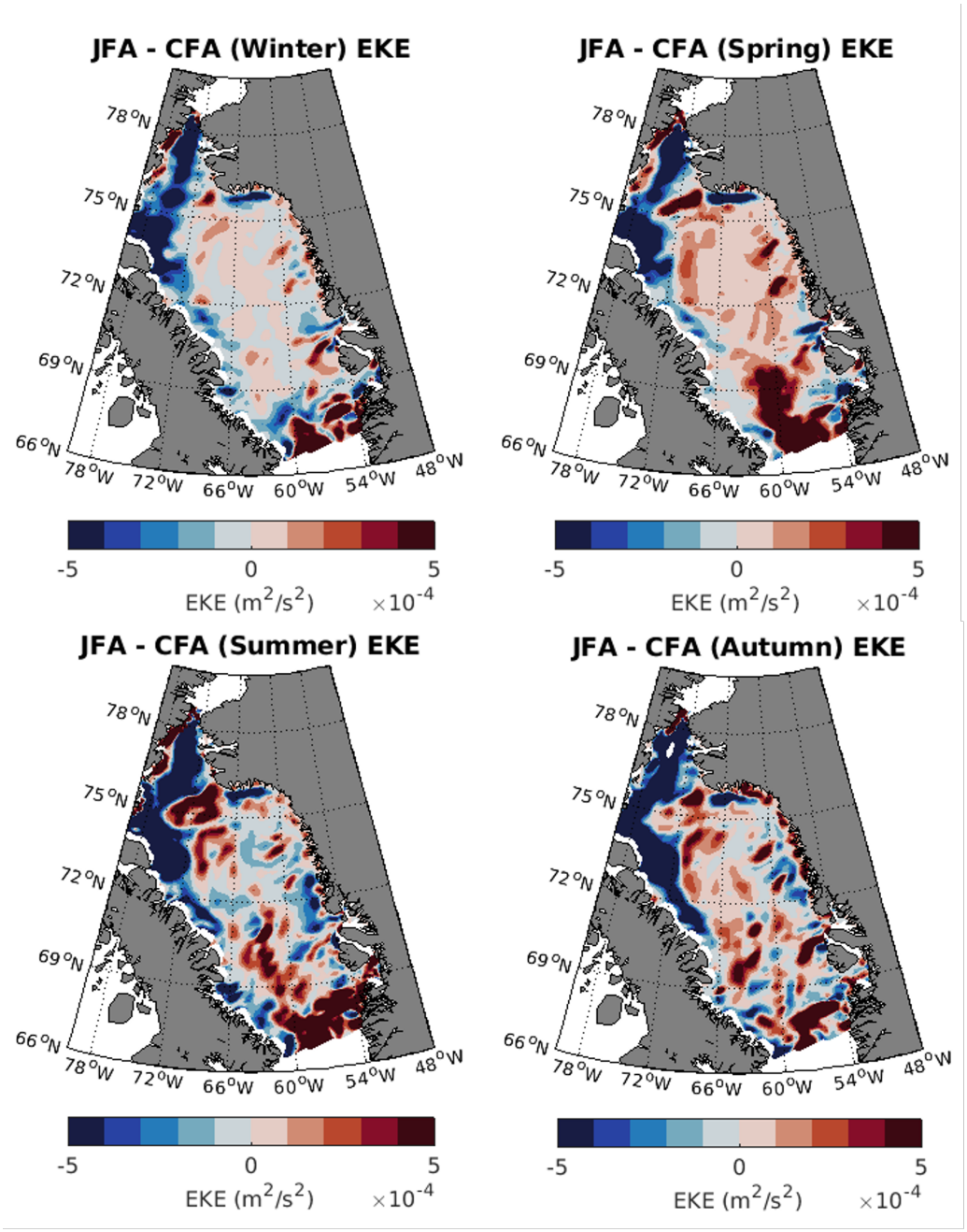

Figure 3.56: The eddy kinetic energy in CFA subtracted from the eddy kinetic energy in JFA averaged over (a) the winter months, (b) the spring months, (c) the summer months, and (d) the autumn months of the common period of integration (2002 to 2017) over the Baffin Bay.

seasons, we see a prominent red patch with a value 0.02 N/m^2 south of Smith Sound, which translates to a more eastward (or less westward) wind stress ($\vec{\tau}_U$) in JFA as opposed to CFA. This could potentially block the JFA particles from entering the BIC.

In [Zeinali Torbati et al., 2020] the drift of the icebergs was found to be determined by the sea surface height in the open ocean with no sea ice cover. After evaluating wind stress differences between the simulations, we investigate differences in sea surface height (SSH) which would lead to distinct geostrophic circulations. Given that the icebergs' keels are significantly larger than their freeboard, it follows that larger icebergs will be mostly forced by those geostrophic currents [Marson et al., 2018], and therefore their trajectories would be affected by any changes in this circulation. In figure 3.54 the spatial distribution of Baffin Bay seasonal average of sea surface height (SSH) for the simulation JFA (top row) and the simulation CFA (bottom row) are shown. In CFA, a generally higher SSH is observed compared to JFA. To have a better look at the SSH gradient across the basin, Figure 3.50 shows the SSH along the transect indicated in figure 1.3. In CFA, we see a higher SSH on both sides of Baffin Bay compared to the mid-basin especially during the summer and autumn months. On the other hand, in JFA the SSH monotonically decreases from the west to the east side of the basin in winter and spring. In figure 3.55 the subplot (a) shows the average seasonal SSH along the mid basin cross-section (dashed red line in the figure 1.3) for winter (black), spring (blue), summer (magenta), and autumn (red) months in meters in the simulation JFA, whereas the subplot (b) shows the same for the CFA simulation, both along j, i.e. zonal model grid. Baffin Bay in CFA has a steep SSH gradient on the western side (j-values 10 to 20), indicating a strong and narrow BIC. On the eastern side of Baffin Bay, the slight upwards gradient as one approaches the West Greenland coast indicates a stronger WGC that is even stronger in summer and autumn (SSH gradients is steeper in these two seasons compared to in winter and spring). In JFA, the western SSH gradient is smaller and the upwards gradient in the east disappears in winter and spring. An in general lower SSH all over the basin with a more monotonous west-to-east slope in JFA was indeed found (subplot (b) of 3.55). This contrast suggests that the Baffin Bay gyre circulation is likely stronger in CFA compared to that in JFA, causing the particles calved at Northwest Greenland outlets reach Baffin Island coast more in number.

Figure 4.11 shows the meridional component of ocean velocity across Davis Strait (solid navy blue line in figure 1.3) for the CFA simulation. We see well-defined

southward (blue) and northward (red) cores to the west (Baffin Island side) and east (Greenland side), respectively, for all months of the year. JFA (figure 4.12), however, has a weak and broad southward flux through most of Davis Strait, and a northward flux that only appears at the west Greenland shelf break during summer and autumn months. A weak BIC and seasonal WGC might be the reason behind the reduced number of particles that traveled southward along the Baffin Island shelf: the stronger and more consistent circulation in CFA is likely more effective in driving the particles calved from west Greenland northwards and westward to the BIC.

As the Baffin Bay circulation is in geostrophic balance, the pressure gradient force connected with sea surface elevation balances the coriolis force. Therefore, a verification of energy differences in the Baffin Bay gyre circulation between the two simulations could further testify the argument in the previous subsection. To verify that, we analyzed the anomaly in eddy kinetic energy (EKE) between the two runs for four seasons over Baffin Bay. The spatial distribution of seasonal average of JFA - CFA Baffin Bay EKE over the first layer of ocean for the two simulations are compared in the figure 3.56. We see vibrant blue patches in the northwester Baffin Bay, which represents a more energetic (5×10^{-4} m^2/s^2) surface circulation in CFA compared to JFA. This explains the differences in SSH between the two simulations for all the seasons across Baffin Bay. The circulation in JFA is not strong enough to keep the particles from drifting into the mid-basin, and thus caused the depletion in the iceberg counts in BIC (the circle number 3 in figure 3.50). This analysis suggests that the hydrodynamics in Baffin Bay gyre could be a very important contributing factor in determining the I48N variability. Furthermore, a strong positive anomaly south of Davis Strait in the figure 3.56 stands for a more energetic surface (5×10^{-4} m^2/s^2) ocean in JFA. This, along with the southward flow (shown in figure 4.12) of values 0.2 m/s might also explain the loss of particles with southwestern Greenland origin the JFA simulation, hence the lower I48N.

3.3.5 Section synopsis

In JFA simulation, due to the initial iceberg field, the iceberg mass in the ocean is stabilized from the first year. However, a very small number of particles reached 48° N. Large particles arrived at 48° all year round, making the season even wider than that in CFA. The peak month in the average season is shifted to August. The correlations among the local ocean conditions and the modelled I48N

matched the observed correlations closely after 2004. The correlation between upstream sea ice condition and modelled I48N in JFA also improved significantly in later years. In other words, the model took about a decade to fully equilibriate the relationships. A warmer ocean in Labrador shelf was found to melt the icebergs faster in this simulation compared to in CFA. However, in JFA the total iceberg mass entering east coast of Canada was lowered by upstream processes compared to the same in CFA simulation. Despite the fact that in JFA simulation, we had more particles than in CFA near the west Greenland calving sites, the particle counts in Baffin Island coast was much lower in JFA. The Baffin Bay SST and SSH were found to cause this anomaly. The ocean temperature was much warmer in JFA near the highest contributing calving sectors that increased the iceberg melt rate in that region in JFA. Moreover, a steeper SSH gradient in Baffin Bay was found in CFA that is associated with a stronger circulation moving the particles from West Greenland origin towards Baffin Island shelf. On the other hand, in JFA simulation, the SSH gradient was more flat encouraging more southward flow in the eastern side of the basin. Therefore, a lot less number of particles from their west Greenland calving locations entered BIC in JFA simulation. It could be inferred that the iceberg season severity off the east coast is dependent on the upstream oceanic condition, especially, around the major contributing calving sites, and the upstream ocean circulations.

Chapter 4

Summary and conclusion

With the growing interannual variability in the observed number of icebergs reaching the east coast of Canada, the projection of an upcoming iceberg season becomes more challenging. Under the backdrop of a warming world during the recent decades, scientists anticipate further increase in calving from tidewater glaciers (that are the major source of the icebergs reaching east coast of Canada) in Greenland. The shipping and other offshore activities are also expected to increase with shorter sea ice season. Therefore, the ability to predict the severity of the upcoming iceberg season is desirable. Moreover, due to challenges in data collection in cold regions, there is a scarcity of observations of the iceberg trajectories from northern regions. Hence, iceberg modelling is necessary, and more accuracy in the model representation of the icebergs in the North Atlantic is required in order to improve the understanding of processes governing the iceberg distribution in these sub-Arctic waters. In this study, we evaluated the Nucleus for European Modelling of the Ocean (NEMO) model representation of interconnections between iceberg season severity in east coast of Canada and its potential drivers, as suggested in previous studies. In addition, we tested the iceberg model sensitivity towards different atmospheric forcings.

4.1 Findings

1. During the current reconnaissance period (1983-2021) of International Ice Patrol (IIP), the iceberg season became longer compared to the previous periods. The interannual variance of the Icebergs south of 48° North (I48N) has also increased.

2. Among the local environmental conditions that might be driving I48N

variability, the observed ocean temperature in Newfoundland and Labrador shelf during the peak iceberg season exhibited strong correlations with the observed year-to-year fluctuation of the iceberg season. In general, the warmer the upper layer of the ocean during spring, the lighter the severity of the iceberg season was. The winter sea ice concentration in the northern part of Labrador coast displayed an even higher correlation with the iceberg severity variability. Moreover, this correlation was found to increase from the first half (1979-2000) of the above-mentioned period to the second half of that period. This might indicate that the winter sea ice concentration over the Labrador shelf impacts the severity of the iceberg season in recent decades more than before. During the winters of the heavier to extreme iceberg years, the Labrador coast was covered with more sea ice.

3. The observed interannual variability in Baffin Bay high concentration ($\geq 90\%$) sea ice covered area (for the years of observation: 1979 to 2021) did not share any statistically significant correlation with the variability in the iceberg counts in Grand Banks region. However, the spatial patterns at the sea ice edge of Baffin Bay were observed to vary accordingly with the upcoming severity of the iceberg season along the east Canadian coast: there was less (more) highly concentrated sea ice pack during the winter months of the lighter (heavier) iceberg years.

4. The observed calving rate, as suggested in former studies, was expected to be higher during the years of larger iceberg influx at 48° N. In this study, we found no such relationships. However, in this analysis, biases could be large.

5. Iceberg counts reaching 48° N are largely underestimated in the model. The reason behind this might be linked to the calving distribution and size classes defined in the model.

6. Although the peak months (April-May) of the iceberg season is rightly represented during the spring months, the modelled season is broader. In fact, a few (3 to 5 % of the peak) modelled icebergs arrive at the Grand Banks during the off-season months (September through January). As the large class particles reach 48° N all year round.

7. The modelled I48N seasonality also vary based on the size of the icebergs. The larger the size class of the particles, the longer (all year round) the iceberg season is in the model. Icebergs of small size classes reach 48° N only during the spring-summer months.

8. The observed improvement in correlation between the ocean temperature and the I48N when the temperature along the iceberg keel was considered over just the skin temperature is not reflected in the model. However, the observed correlation between the local ocean temperatures (both SST and vertically

averaged) and the I48N were better represented in JFA compared to CFA for the period 2004 to 2017. For the corresponding entire periods of simulation, in both CFA (2002-2017) and JFA (1993-2017) simulations, the I48N-local sea ice area correlations are statistically non-significant and low (-0.29, ans -0.06 respectively) compared to the observed correlation (0.81). In JFA, however, the correlation significantly improved for the period 2004-2017, which also resembles the increase in observed correlations with time. For all the three local factors, the model representation of relationships with I48N improved for the later period in JFA. This increase in correlations with time might be associated with the ocean adjustment to the atmospheric forcing in the model and sub-sequentially the adjustment of the iceberg model to the "balanced" ocean field.

9. For the lighter iceberg years, the northern Labrador shelf has lesser concentration of sea ice during the winter months in the JFA simulation.

10. For the remote environmental influence, the association of Baffin Bay winter sea ice cover with the upcoming season severity was non-significant in both simulations, when computed over their corresponding whole periods of integration. However, when calculated for the 2004-2017 period, the JFA correlation grew close to the observed correlation. This again indicates that the relationships between I48N and its governing factors take time to emerge in the model due to model adjustment to forcings.

11. The zonal wind stress difference between the two simulations seem to play a role in determining iceberg distribution regionally, especially along the east coast of Greenland.

12. A noticeable difference in Baffin Bay sea surface temperature due to different atmospheric forcing was found, especially during summer months. A warmer (0.7 to 1 °C) ocean in JFA melted many icebergs near their northwestern calving grounds. A flatter sea surface height slope decreased the strength of the West Greenland Current and therefore decreased the northward flux of icebergs calved from the Central West and Southwest sectors. These phenomena together led to lower number of particles reaching the Baffin Island Current in this simulation compared to CFA simulation. A cooler ocean in CFA caused the particles to survive in the Baffin Bay circulation and to enter Labrador shelf with more mass in general. Moreover, steeper sea surface height gradients in both sides of Baffin Bay in CFA encouraged a stronger BIC. That is, a stronger BIC was more effective in carrying the particles south towards the Labrador Current. In JFA, as the BIC was broader and weaker, icebergs were likely allowed to drift out of this boundary current. These differences in the remote conditions gave rise to a prominent difference in the iceberg masses and counts entering the Labrador shelf

between the two simulation.

4.2 Limitations and biases

We need to keep the following possible sources of biases and errors in mind, when drawing conclusions from the outcomes of this study:
1. The size distribution is based on Antarctic icebergs, and it is likely not the same for Greenlandic icebergs in the real world. As all the forces in the dynamic equations are functions of dimensions or mass of icebergs, and the time rate of disintegration of mass also depends on those attributes, an unrealistic size distribution could generate biases in both drifting and melting of icebergs. [Åström et al., 2021] showed that representing calving from independent fractures with an exponential function, and from correlated branched fractures with a power-law function leads to a more accurate size and frequency of icebergs.
2. The calving forcing does not provide any solid discharge for Canadian Arctic Archipelago.
3. In the real world, Greenland icebergs are calved into fjords, where they loose approximately 50% of their mass. The particles in the model, however, are released directly into the ocean. As the horizontal resolution we use is not high enough to capture the fjord dynamics and thermodynamics, a lot of real-world fjord-related processes especially in terms of mass loss are unaccounted for in the model.
4. Due to lack of upstream observation of iceberg trajectories, we used model outputs to acquire values (the statistical distribution of which is shown in the figure 4.3) of the most typical time taken by the icebergs to reach the Grand Banks from their different origins. Therefore, the methodology we adopted to establish the time gap between the I48N and the calving contributing the I48N might not be realistic.
5. Given the eddy-permitting resolution (approximately 12 to 20 km over the domain of interest) of the used configuration, many sub-grid scale processes that could potentially impact the icebergs, movement are not represented in the simulation.
6. The short period of integration of the CFA simulation could introduce biases in the definitions of the severity classes. Also, JFA results suggest that the model takes about a decade to stabilize the correlations, even after starting with an iceberg field. Therefore, short simulations such as CFA are likely unable to reproduce the relationships between environmental forcing and I48N.
7. Grounding of the icebergs is not properly parameterized yet in the model,

which is frequently observed in real world. In addition to that, the lack of fast ice parameterization (which is suggested to be important in determining the release of the icebergs during the sea ice melting in [Marko et al., 2014]) could introduce errors in the arrival time of the modelled icebergs at the east coast of Canada.
8. The correlation analyses might not be robust as we worked with small number of data points in the time series. Observational analyses include 27 years, whereas CFA include only 14 years, and JFA only 24 years.

4.3 Conclusion

A warming environment has shortened the sea ice season, encouraging offshore activities along the east coast of Canada, where icebergs from Greenland pose threats to offshore structures and ships. Consequently, marine industries require accurate predictions of iceberg season severity. At the same time, climate change–driven increases in Greenland glacier iceberg discharge have raised the likelihood of iceberg occurrences along the east Canadian coast, while the variability of iceberg numbers in North Atlantic waters has become more unpredictable in recent decades. These phenomena together call for deeper insight into the interconnections between environmental factors and iceberg season severity.
Sparse information about icebergs' trajectories in the upstream regions makes identification of the most dominant drivers challenging, making improved model representation critical. In this study, we found that a more sea ice-covered ocean in winter and a cooler spring ocean over the Labrador shelf were observed before the heavier iceberg seasons. The model study showed that a warmer ocean, in simulations with warmer atmospheric forcing, accelerated iceberg mass loss before reaching the northern Labrador coast. Differences in Baffin Bay circulation energy, linked to the sea surface elevation, influence iceberg transport through the basin, significantly affecting their influx into the Labrador current. Since most icebergs reaching eastern Canadian shipping lanes originate from west Greenland glaciers, this finding provides a basis for future model sensitivity studies.
The longer simulation initialized with a stabilized iceberg mass captured correlations between oceanic conditions and iceberg interannual variability more accurately compared to the shorter run starting without icebergs. This highlights the importance of spin-up periods, recommending a longer spin-up for future studies. Furthermore, we suggest future studies on observed relationship between sea surface height and iceberg season severity. Additionally, refining representations of iceberg size classes and mass-frequency distributions could

bring model predictions closer to real-world iceberg occurrences along the east coast of Canada, advancing the model toward accurate iceberg season prediction.

Bibliography

[Bamber et al., 2018a] Bamber, J. L., Tedstone, A. J., King, M. D., Howat, I. M., Enderlin, E. M., Van Den Broeke, M. R., and Noel, B. (2018a). Land Ice Freshwater Budget of the Arctic and North Atlantic Oceans: 1. Data, Methods, and Results. *Journal of Geophysical Research: Oceans*, 123(3):1827–1837.

[Bamber et al., 2018b] Bamber, J. L., Tedstone, A. J., King, M. D., Howat, I. M., Enderlin, E. M., van den Broeke, M. R., and Noel, B. (2018b). Land Ice Freshwater Budget of the Arctic and North Atlantic Oceans: 1. Data, Methods, and Results. *Journal of Geophysical Research: Oceans*, 123(3):1827–1837. _eprint: https://onlinelibrary.wiley.com/doi/pdf/10.1002/2017JC013605.

[Barker and Carrieres, 2004] Barker, A. and Carrieres, T. (2004). Determination of Iceberg Draft, Mass and Cross-Sectional Areas. *Proceedings of the International Offshore and Polar Engineering Conference*.

[Bigg et al., 1997] Bigg, G. R., Wadley, M. R., Stevens, D. P., and Johnson, J. A. (1997). Modelling the dynamics and thermodynamics of icebergs. *Cold Regions Science and Technology*, 26(2):113–135.

[Bigg et al., 2014] Bigg, G. R., Wei, H. L., Wilton, D. J., Zhao, Y., Billings, S. A., Hanna, E., and Kadirkamanathan, V. (2014). A century of variation in the dependence of Greenland iceberg calving on ice sheet surface mass balance and regional climate change. *Proceedings of the Royal Society A: Mathematical, Physical and Engineering Sciences*, 470(2166):20130662.

[Bigg et al., 2021] Bigg, G. R., Zhao, Y., and Hanna, E. (2021). Forecasting the severity of the Newfoundland iceberg season using a control systems model. *Journal of Operational Oceanography*, 14(1):24–36.

[Bouillon et al., 2009] Bouillon, S., Morales Maqueda, M. , Legat, V., and Fichefet, T. (2009). An elastic–viscous–plastic sea ice model formulated on Arakawa B and C grids. *Ocean Modelling*, 27(3-4):174–184.

[Cenedese and Straneo, 2023] Cenedese, C. and Straneo, F. (2023). Icebergs Melting. *Annual Review of Fluid Mechanics*, 55(1):377–402.

[Cyr and Galbraith, 2021] Cyr, F. and Galbraith, P. S. (2021). A climate index for the Newfoundland and Labrador shelf. *Earth System Science Data*, 13(5):1807–1828.

[Deschepper et al., 2023] Deschepper, I., Myers, P. G., Lavoie, D., Papakyriakou, T., and Maps, F. (2023). Understanding the Physical Forcings Behind the Biogeochemical Productivity of the Hudson Bay Complex. *Journal of Geophysical Research: Biogeosciences*, 128(6).

[Enderlin et al., 2016] Enderlin, E. M., Hamilton, G. S., Straneo, F., and Sutherland, D. A. (2016). Iceberg meltwater fluxes dominate the freshwater budget in Greenland's iceberg-congested glacial fjords. *Geophysical Research Letters*, 43(21).

[Fichefet and Maqueda, 1997] Fichefet, T. and Maqueda, M. A. M. (1997). Sensitivity of a global sea ice model to the treatment of ice thermodynamics and dynamics. *Journal of Geophysical Research, Washington, DC*, 102(C6):12609–12646. Place: WASHINGTON Publisher: Blackwell Publishing Ltd.

[Gladstone et al., 2001] Gladstone, R. M., Bigg, G. R., and Nicholls, K. W. (2001). Iceberg trajectory modeling and meltwater injection in the Southern Ocean. *Journal of Geophysical Research: Oceans*, 106(C9):19903–19915. _eprint: https://onlinelibrary.wiley.com/doi/pdf/10.1029/2000JC000347.

[Hanna et al., 2013] Hanna, E., Navarro, F. J., Pattyn, F., Domingues, C. M., Fettweis, X., Ivins, E. R., Nicholls, R. J., Ritz, C., Smith, B., Tulaczyk, S., Whitehouse, P. L., and Zwally, H. J. (2013). Ice-sheet mass balance and climate change. *Nature (London)*, 498(7452):51–59. Place: London Publisher: Nature Publishing Group UK.

[Helly et al., 2011] Helly, J. J., Kaufmann, R. S., Stephenson, G. R., and Vernet, M. (2011). Cooling, dilution and mixing of ocean water by free-drifting icebergs

in the Weddell Sea. *Deep Sea Research Part II: Topical Studies in Oceanography*, 58(11-12):1346–1363.

[Hill, 2005] Hill, B. (2005). Ship collisions with iceberg database. Report to PERD: trends and analysis. Technical report, National Research Council of Canada. Institute for Ocean Technology. Publication Title: Technical Report (National Research Council of Canada. Institute for Ocean Technology) Volume: TR-2005-17.

[Hu et al., 2019] Hu, X., Myers, P. G., and Lu, Y. (2019). Pacific Water Pathway in the Arctic Ocean and Beaufort Gyre in Two Simulations With Different Horizontal Resolutions. *Journal of Geophysical Research: Oceans*, 124(8):6414–6432.

[Ivanova et al., 2015] Ivanova, N., Pedersen, L. T., Tonboe, R. T., Kern, S., Heygster, G., Lavergne, T., Sørensen, A., Saldo, R., Dybkjær, G., Brucker, L., and Shokr, M. (2015). Inter-comparison and evaluation of sea ice algorithms: towards further identification of challenges and optimal approach using passive microwave observations. *The Cryosphere*, 9(5):1797–1817.

[Jean-Michel et al., 2021] Jean-Michel, L., Eric, G., Romain, B.-B., Gilles, G., Angélique, M., Marie, D., Clément, B., Mathieu, H., Olivier, L. G., Charly, R., Tony, C., Charles-Emmanuel, T., Florent, G., Giovanni, R., Mounir, B., Yann, D., and Pierre-Yves, L. T. (2021). The Copernicus Global 1/12° Oceanic and Sea Ice GLORYS12 Reanalysis. *Frontiers in Earth Science*, 9:698876.

[Kern et al., 2020] Kern, S., Lavergne, T., Notz, D., Pedersen, L. T., and Tonboe, R. (2020). Satellite passive microwave sea-ice concentration data set inter-comparison for Arctic summer conditions. *The Cryosphere*, 14(7):2469–2493.

[Krause et al., 2024] Krause, J., Carroll, D., Höfer, J., Donaire, J., Achterberg, E. P., Alarcón, E., Liu, T., Meire, L., Zhu, K., and Hopwood, M. J. (2024). The macronutrient and micronutrient (iron and manganese) content of icebergs. *The Cryosphere*, 18(12):5735–5752. Publisher: Copernicus GmbH.

[Kubat et al., 2005] Kubat, I., Sayed, M., and Savage, S. B. (2005). An Operational Model of Iceberg Drift. *International Journal of Offshore and Polar Engineering*, 15(2).

[Lichey and Hellmer, 2001] Lichey, C. and Hellmer, H. H. (2001). Modeling giant-iceberg drift under the influence of sea ice in the Weddell Sea, Antarctica. *Journal of Glaciology*, 47(158):452–460.

[Madec and Imbard, 1996] Madec, G. and Imbard, M. (1996). A global ocean mesh to overcome the north pole singularity. *Climate Dynamics*, 12:381–388.

[Marko et al., 2014] Marko, J. R., Fissel, D. B., Martinez De Saavedra Alvarez, M., Ross, E., and Kerr, R. (2014). Iceberg severity off the east coast of North America in relation to upstream sea ice variability: An update. In *2014 Oceans - St. John's*, pages 1–6, St. John's, NL. IEEE.

[Marko et al., 1994] Marko, S. R., Fissel, D. B., Wadhams, P., Kelly, P. M., and Brown, R. D. (1994). Iceberg Severity of Eastern North America: Its Relationship to Sea Ice Variability and Climate Change. *Journal of climate*, 7(9):1335–1351.

[Marsh et al., 2015] Marsh, R., Ivchenko, V. O., Skliris, N., Alderson, S., Bigg, G. R., Madec, G., Blaker, A. T., Aksenov, Y., Sinha, B., Coward, A. C., Le Sommer, J., Merino, N., and Zalesny, V. B. (2015). NEMO–ICB (v1.0): interactive icebergs in the NEMO ocean model globally configured at eddy-permitting resolution. *Geoscientific Model Development*, 8(5):1547–1562.

[Marson et al., 2021] Marson, J. M., Gillard, L. C., and Myers, P. G. (2021). Distinct Ocean Responses to Greenland's Liquid Runoff and Iceberg Melt. *Journal of Geophysical Research: Oceans*, 126(12):e2021JC017542.

[Marson et al., 2024] Marson, J. M., Myers, P. G., Garbo, A., Copland, L., and Mueller, D. (2024). Sea Ice-Driven Iceberg Drift in Baffin Bay. *Journal of Geophysical Research: Oceans*, 129(5):e2023JC020697. _eprint: https://onlinelibrary.wiley.com/doi/pdf/10.1029/2023JC020697.

[Marson et al., 2018] Marson, J. M., Myers, P. G., Hu, X., and Le Sommer, J. (2018). Using Vertically Integrated Ocean Fields to Characterize Greenland Icebergs' Distribution and Lifetime. *Geophysical Research Letters*, 45(9):4208–4217.

[Martin and Adcroft, 2010] Martin, T. and Adcroft, A. (2010). Parameterizing the fresh-water flux from land ice to ocean with interactive icebergs in a coupled climate model. *Ocean Modelling*, 34(3-4):111–124.

[Masina et al., 2017] Masina, S., Storto, A., Ferry, N., Valdivieso, M., Haines, K., Balmaseda, M., Zuo, H., Drevillon, M., and Parent, L. (2017). An ensemble of eddy-permitting global ocean reanalyses from the MyOcean project. *Climate Dynamics*, 49(3):813–841.

[Merino et al., 2016] Merino, N., Le Sommer, J., Durand, G., Jourdain, N. C., Madec, G., Mathiot, P., and Tournadre, J. (2016). Antarctic icebergs melt over the Southern Ocean: Climatology and impact on sea ice. *Ocean Modelling*, 104:99–110.

[Mountain, 1980] Mountain, D. (1980). On predicting iceberg drift. *Iceberg Dynamics Symposium*, 1(3):273–282.

[Pennelly and Myers, 2021] Pennelly, C. and Myers, P. G. (2021). Impact of Different Atmospheric Forcing Sets on Modeling Labrador Sea Water Production. *Journal of Geophysical Research: Oceans*, 126(2).

[Peterson et al., 2015] Peterson, I., Pettipas, R., and Rosing-Asvid, A. (2015). Trends and Variability in Sea Ice and Icebergs off the Canadian East Coast. *Atmosphere-Ocean*, 53(5):582–594.

[Pizzolato et al., 2016] Pizzolato, L., Howell, S. E. L., Dawson, J., Laliberté, F., and Copland, L. (2016). The influence of declining sea ice on shipping activity in the Canadian Arctic. *Geophysical Research Letters*, 43(23):12,146–12,154. _eprint: https://onlinelibrary.wiley.com/doi/pdf/10.1002/2016GL071489.

[Rackow et al., 2017] Rackow, T., Wesche, C., Timmermann, R., Hellmer, H. H., Juricke, S., and Jung, T. (2017). A simulation of small to giant Antarctic iceberg evolution: Differential impact on climatology estimates. *Journal of Geophysical Research: Oceans*, 122(4):3170–3190. _eprint: https://onlinelibrary.wiley.com/doi/pdf/10.1002/2016JC012513.

[Rignot et al., 2011] Rignot, E., Velicogna, I., van den Broeke, M. R., Monaghan, A., and Lenaerts, J. T. M. (2011). Acceleration of the contribution of the Greenland and Antarctic ice sheets to sea level rise. *Geophysical Research Letters*, 38(5). _eprint: https://onlinelibrary.wiley.com/doi/pdf/10.1029/2011GL046583.

[Robe et al., 1980] Robe, R., Maier, D., and Russell, W. (1980). Long-term drift of icebergs in Baffin Bay and the Labrador Sea. *Cold regions science and technology*, 1(3):183–193. Publisher: Elsevier B.V.

[Rudnickas, Serumgard,] Rudnickas, Serumgard. 2018_annual_report_final.pdf.

[Smith et al., 2014] Smith, G., Roy, F., Mann, P., Dupont, F., Brasnett, B., Lemieux, J.-F., Laroche, S., and Bélair, S. (2014). A new atmospheric dataset for forcing ice–ocean models: Evaluation of reforecasts using the Canadian global deterministic prediction system. *Quarterly Journal of the Royal Meteorological Society*, 140.

[Smith, 1993] Smith, S. D. (1993). Hindcasting iceberg drift using current profiles and winds. *Cold Regions Science and Technology*, 22(1):33–45.

[Smith, E., 1993] Smith, E. (1993). Summary of iceberg Records In the North Western North Atlantic, 1880-1926. In *Report of the International Ice Patrol Services in the North Atlantic*, volume Bullentin No. 15, pages 75–77.

[Stadnyk et al., 2021] Stadnyk, T. A., Tefs, A., Broesky, M., Déry, S. J., Myers, P. G., Ridenour, N. A., Koenig, K., Vonderbank, L., and Gustafsson, D. (2021). Changing freshwater contributions to the Arctic. *Elementa: Science of the Anthropocene*, 9(1):00098.

[Stephenson et al., 2011] Stephenson, G. R., Sprintall, J., Gille, S. T., Vernet, M., Helly, J. J., and Kaufmann, R. S. (2011). Subsurface melting of a free-floating Antarctic iceberg. *Deep Sea Research Part II: Topical Studies in Oceanography*, 58(11-12):1336–1345.

[Straneo and Heimbach, 2013] Straneo, F. and Heimbach, P. (2013). North Atlantic warming and the retreat of Greenland's outlet glaciers. *Nature*, 504(7478):36–43.

[Sudom et al., 2014] Sudom, D., Timco, G., and Tivy, A. (2014). Iceberg sightings, shapes and management techniques for offshore Newfoundland and Labrador: Historical data and future applications. In *2014 Oceans - St. John's*, pages 1–8, St. John's, NL. IEEE.

[Tang et al., 2004] Tang, C. C., Ross, C. K., Yao, T., Petrie, B., DeTracey, B. M., and Dunlap, E. (2004). The circulation, water masses and sea-ice of Baffin Bay. *Progress in Oceanography*, 63(4):183–228.

[Trivers, G.,] Trivers, G. International Ice Patrol's Iceberg Season Severity. In *Report of the International Ice Patrol Services in the in the North Atlantic*, volume Bulletin No 80, pages 49–59.

[Tsujino et al., 2018] Tsujino, H., Urakawa, S., Nakano, H., Small, R. J., Kim, W. M., Yeager, S. G., Danabasoglu, G., Suzuki, T., Bamber, J. L., Bentsen, M., Böning, C. W., Bozec, A., Chassignet, E. P., Curchitser, E., Boeira Dias, F., Durack, P. J., Griffies, S. M., Harada, Y., Ilicak, M., Josey, S. A., Kobayashi, C., Kobayashi, S., Komuro, Y., Large, W. G., Le Sommer, J., Marsland, S. J., Masina, S., Scheinert, M., Tomita, H., Valdivieso, M., and Yamazaki, D. (2018). JRA-55 based surface dataset for driving ocean–sea-ice models (JRA55-do). *Ocean Modelling*, 130:79–139.

[Wilton et al., 2015] Wilton, D. J., Bigg, G. R., and Hanna, E. (2015). Modelling twentieth century global ocean circulation and iceberg flux at 48°N: implications for west Greenland iceberg discharge. *Progress in Oceanography*, 138:194–210.

[Zeinali Torbati et al., 2020] Zeinali Torbati, R., Turnbull, I. D., Taylor, R. S., and Mueller, D. (2020). Evaluation of the relative contribution of meteorological and oceanic forces to the drift of ice islands offshore Newfoundland. *Journal of Glaciology*, 66(256):203–218.

[Zhao et al., 2016] Zhao, Y., Bigg, G. R., Billings, S. A., Hanna, E., Sole, A. J., Wei, H.-l., Kadirkamanathan, V., and Wilton, D. J. (2016). Inferring the variation of climatic and glaciological contributions to West Greenland iceberg discharge in the twentieth century. *Cold Regions Science and Technology*, 121:167–178.

[Åström et al., 2021] Åström, J., Cook, S., Enderlin, E. M., Sutherland, D. A., Mazur, A., and Glasser, N. (2021). Fragmentation theory reveals processes controlling iceberg size distributions. *Journal of Glaciology*, 67(264):603–612.

Appendix

4.4 Supplementary figures

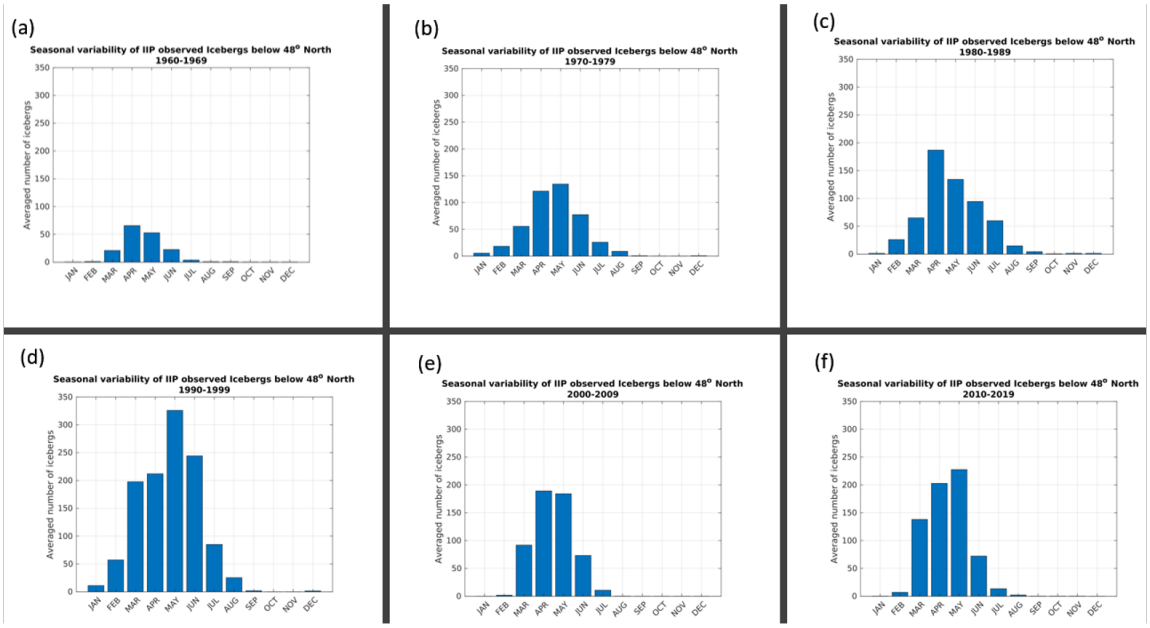

Figure 4.1: Iceberg seasons averaged over six decades: (a) 1960-1969, (b) 1970-1979, (c) 1980-1989, (d) 1990-1999, (e) 2000-2009, and (f) 2010-2019. Each blue bar represents the number of icebergs in the corresponding month, averaged over the decade. For example on an average 52 icebergs reached 48° N in the month of May, during the years 1960-1969.

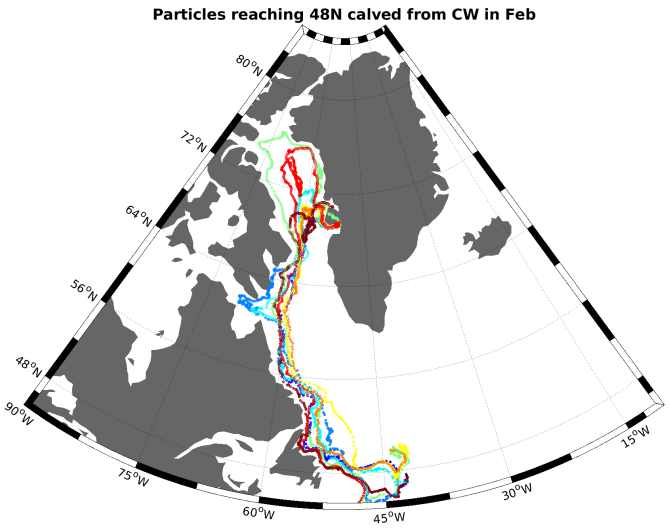

Figure 4.2: Trajectories of particles reaching 48° N, that calved from central West sector of Greenland in the month of February in the CFA simulation. Each color represents the path of a particular particle.

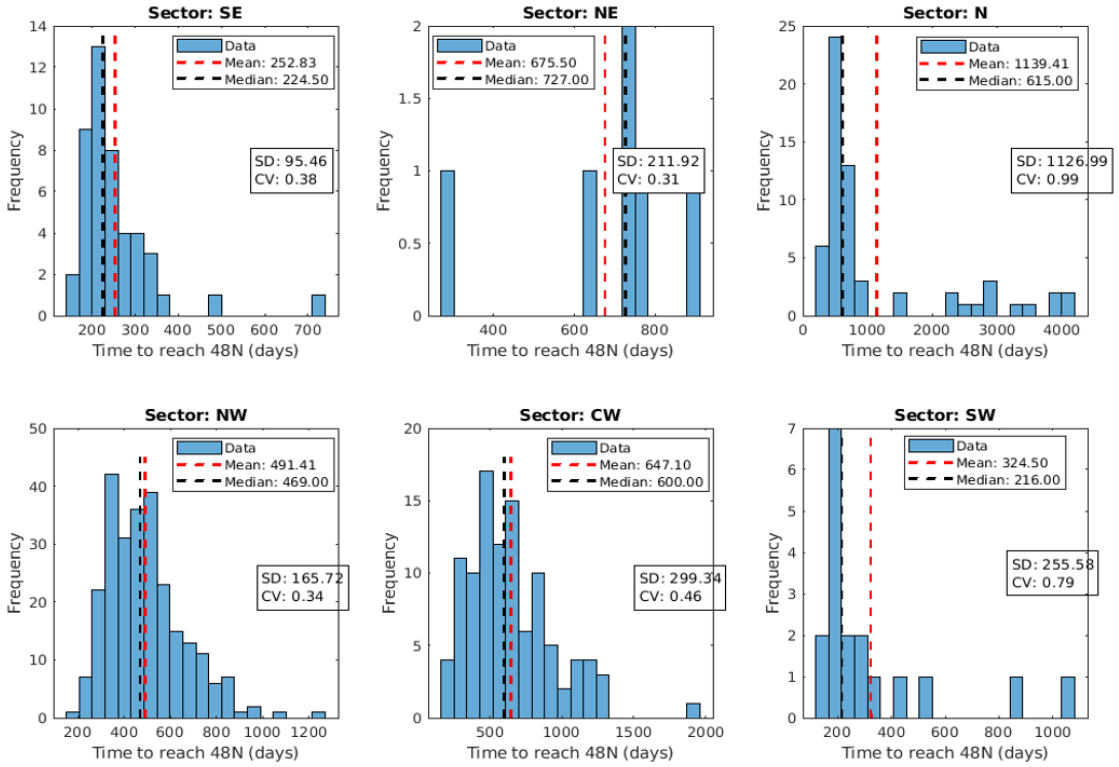

Figure 4.3: Distribution of times (in days) taken by particles in CFA from different Greenland calving sectors to reach 48° North latitude. SD = standard deviation, and CV = covariance of the corresponding data. SE = Southeast, NE = Northeast, N = North, NW = Northwest, CW = Central West, and SW = Southwest as shown in the figure 2.5.

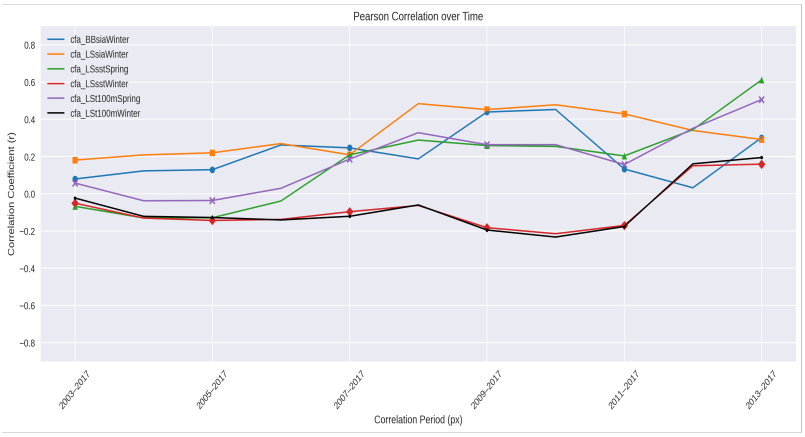

Figure 4.4: The modelled (CFA) time evolution of the correlations between the environmental factors and I48N for Labrador shelf winter SST (sstWinterTS), Labrador shelf spring SST (sstSpringTS), 100 m depth averaged spring ocean temperature over Labrador shelf (T100mSpringTS), 100 m depth averaged winter ocean temperature over Labrador shelf (T100mWinterTS), Winter sea ice area over Labrador shelf (LSsiaWinter), and Baffin Bay high concentration Winter sea ice area (siaWinterTS).

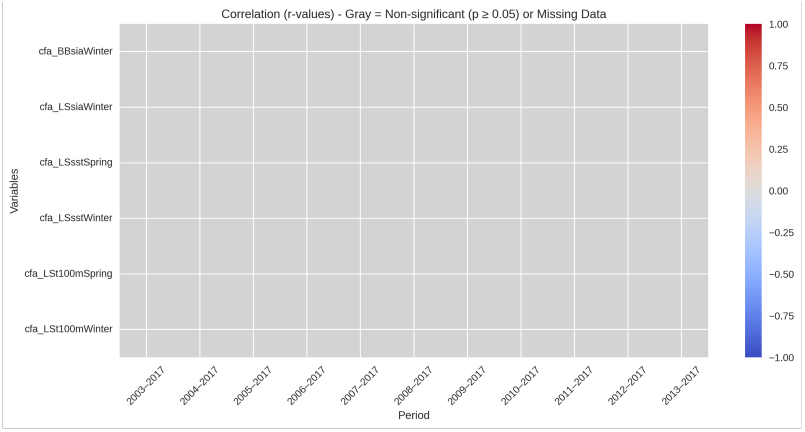

Figure 4.5: Heat map showing the modelled (JFA) Pearson correlation values (along with p-values) between the environmental factors and I48N for Labrador shelf winter SST (sstWinterTS), Labrador shelf spring SST (sstSpringTS), 100 m depth averaged spring ocean temperature over Labrador shelf (T100mSpringTS), 100 m depth averaged winter ocean temperature over Labrador shelf (T100mWinterTS), Winter sea ice area over Labrador shelf (LSsiaWinter), and Baffin Bay high concentration Winter sea ice area (siaWinterTS).

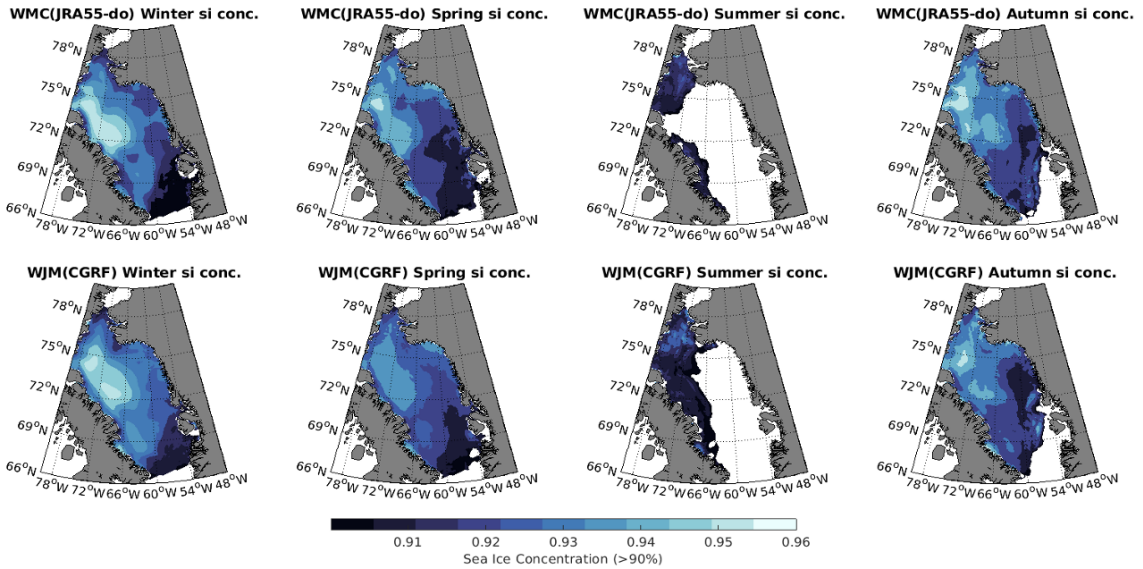

Figure 4.6: The spatial distribution of seasonal average of high concentration ($\geq$ 90%) sea ice in Baffin Bay in JFA (top row), and in CFA (bottom row), in Winter (first column), Spring (second column), Summer (third column), and Autumn (last column) months respectively.

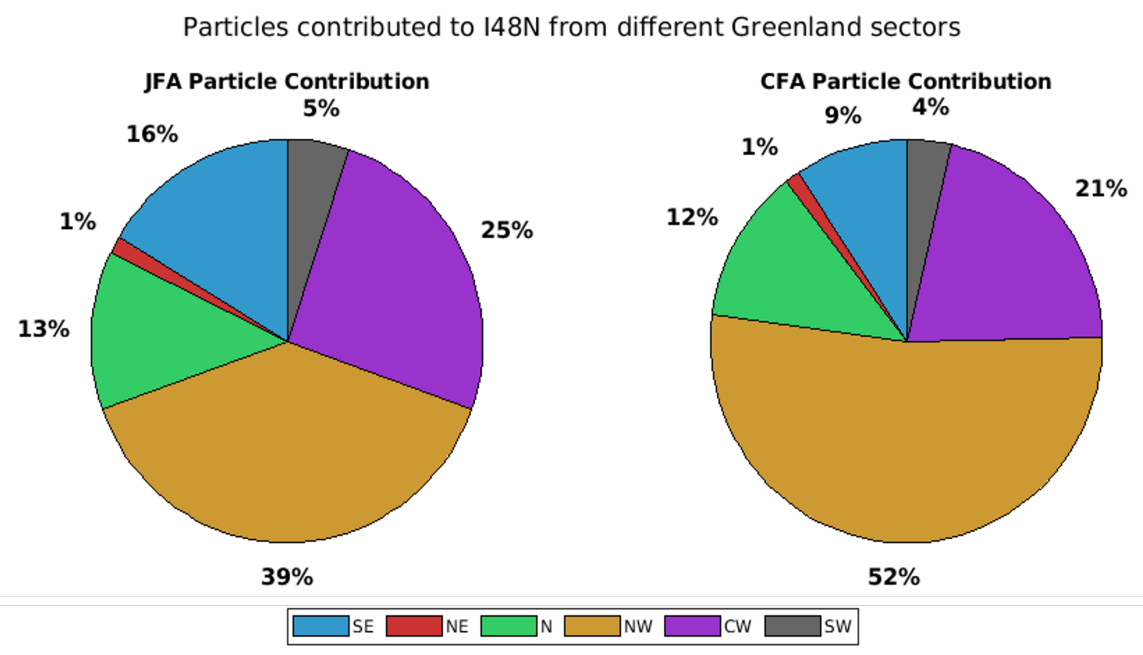

Figure 4.7: Percentage of particles counts in (a) JFA, and (b) CFA simulation calved from the sectors of Greenland. SE = Southeast, NE = Northeast, N = North, NW = Northwest, CW = Central West, and SW = Southwest as shown in the figure 2.5. 16%, 1%, 13%, 39%, 25%, and 5% of I48N in the simulation JFA were originated from SE, NE, N, NW, CW, and SW sectors of Greenland respectively. 9%, 1%, 12%, 52%, 21%, and 4% of I48N in the simulation CFA were originated from SE, NE, N, NW, CW, and SW sectors of Greenland respectively.

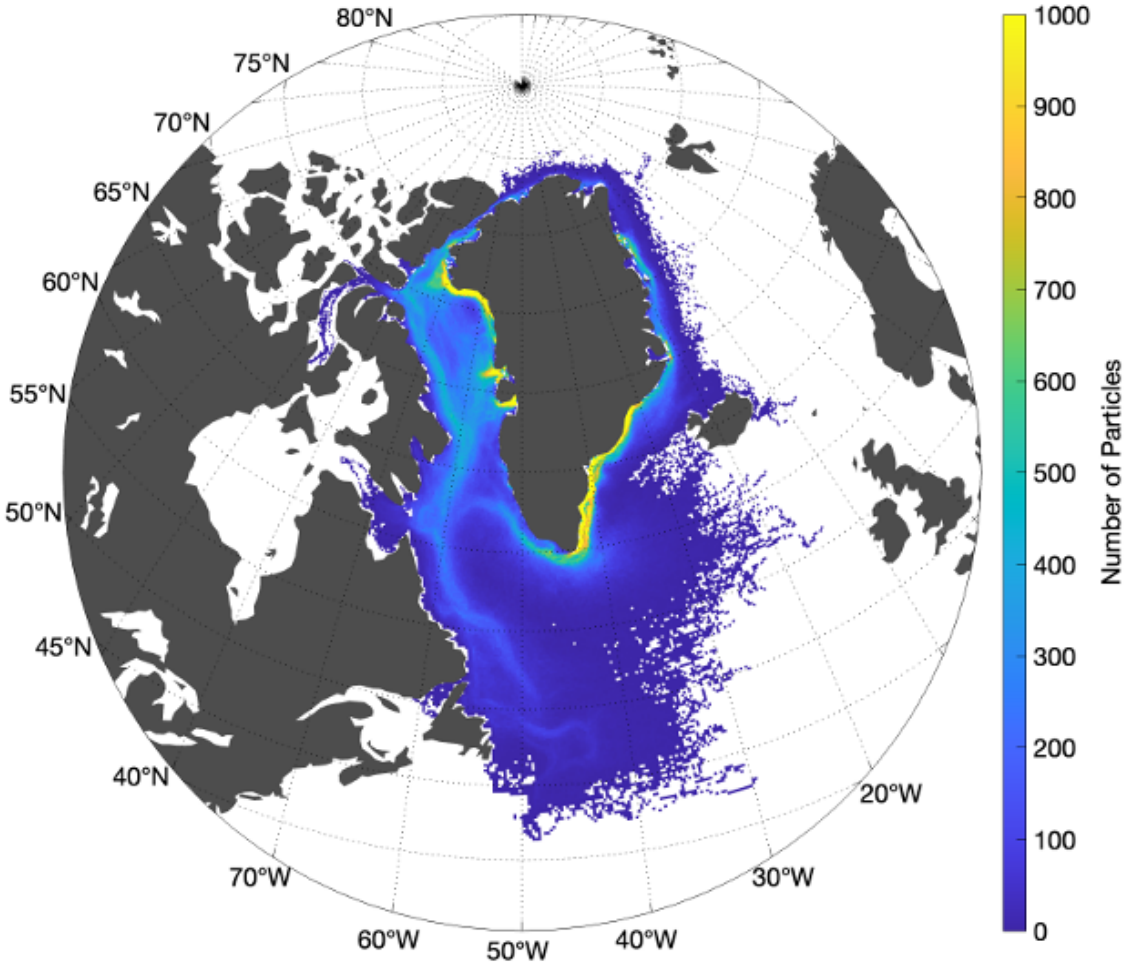

Figure 4.8: Number of particles crossing each grid cell in the CFA simulation over the period 2002 to 2017.

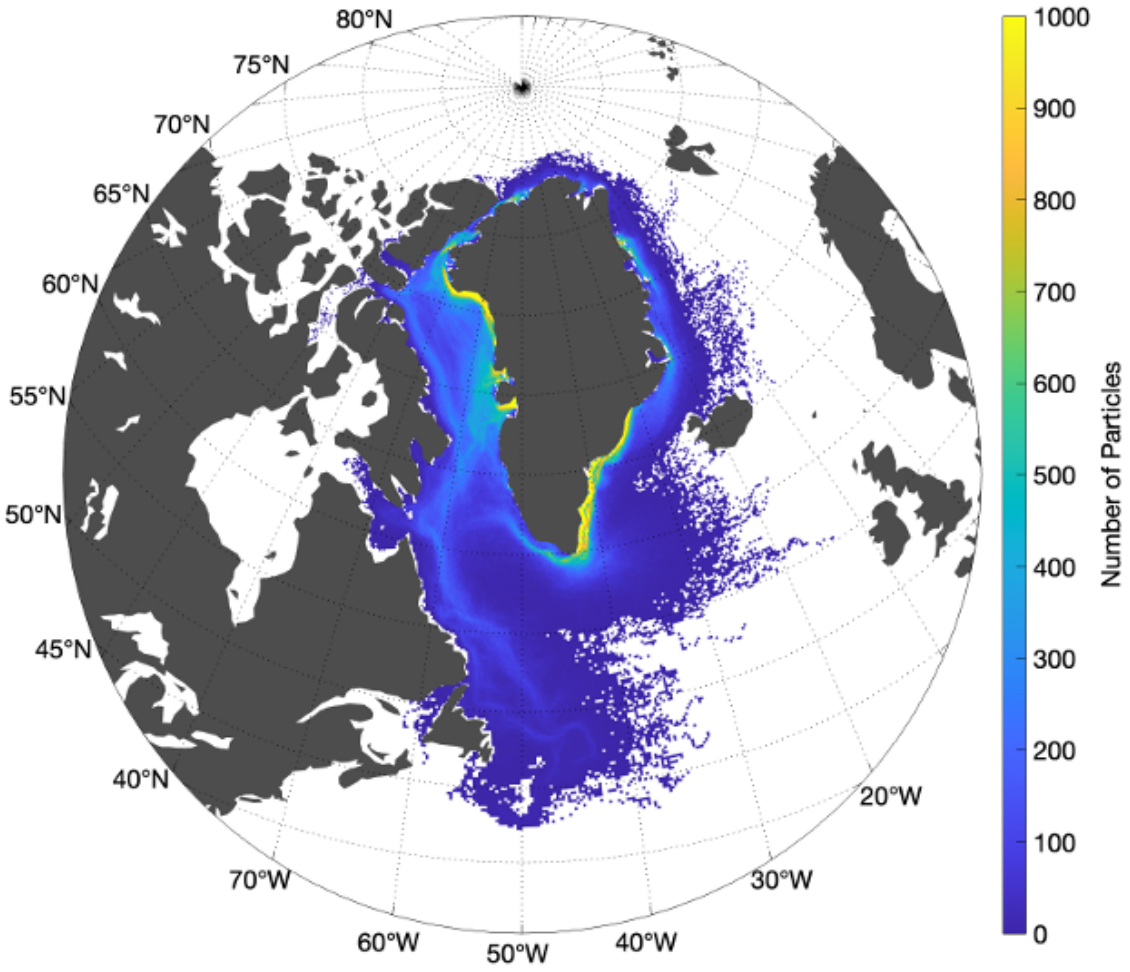

Figure 4.9: Number of particles crossing each grid cell in the JFA simulation over the period 2002 to 2017.

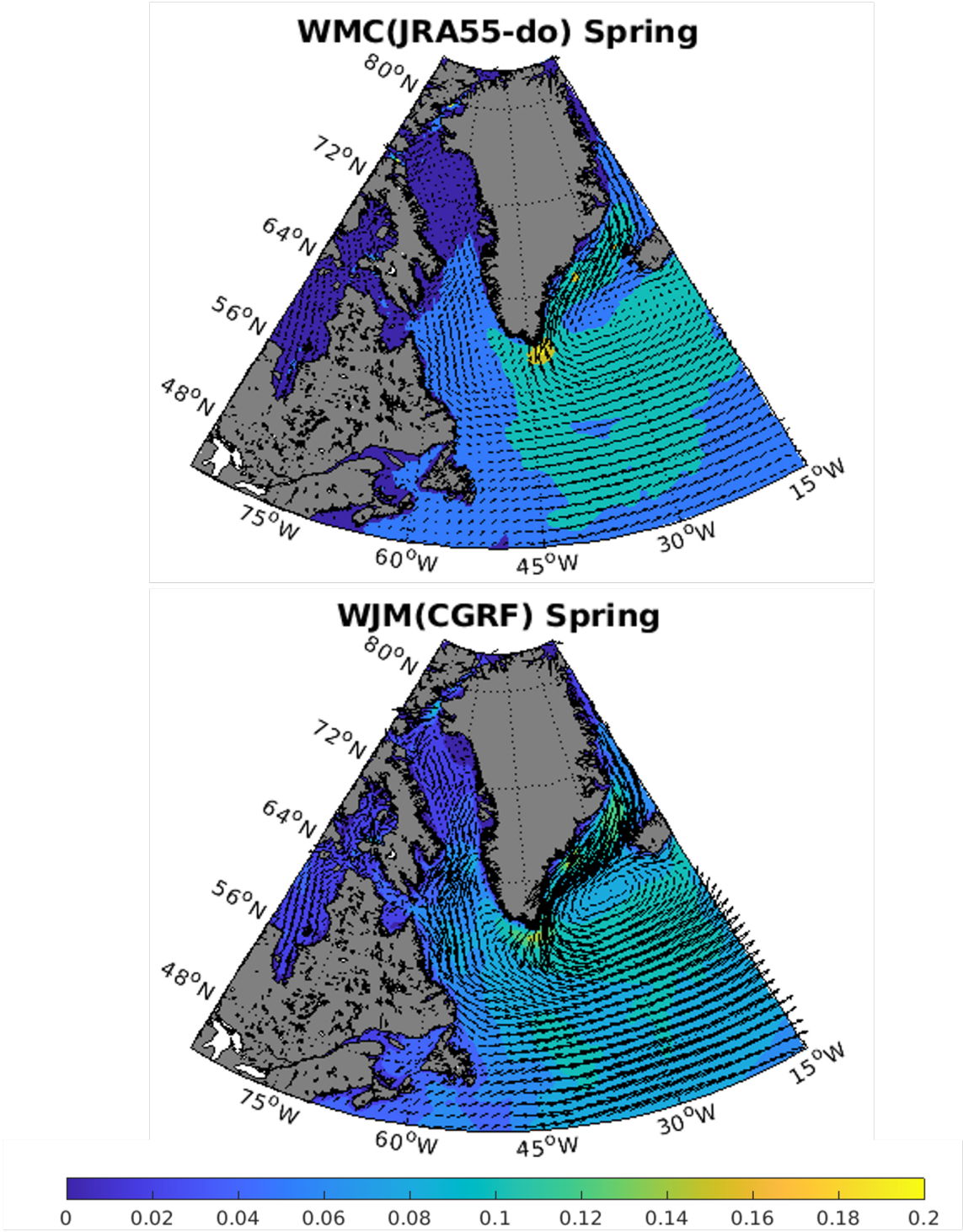

Figure 4.10: Direction (shown with arrows) and magnitude (in m/s) of wind stress vectors over the domain of study in (a) JFA, and (b) CFA simulation.

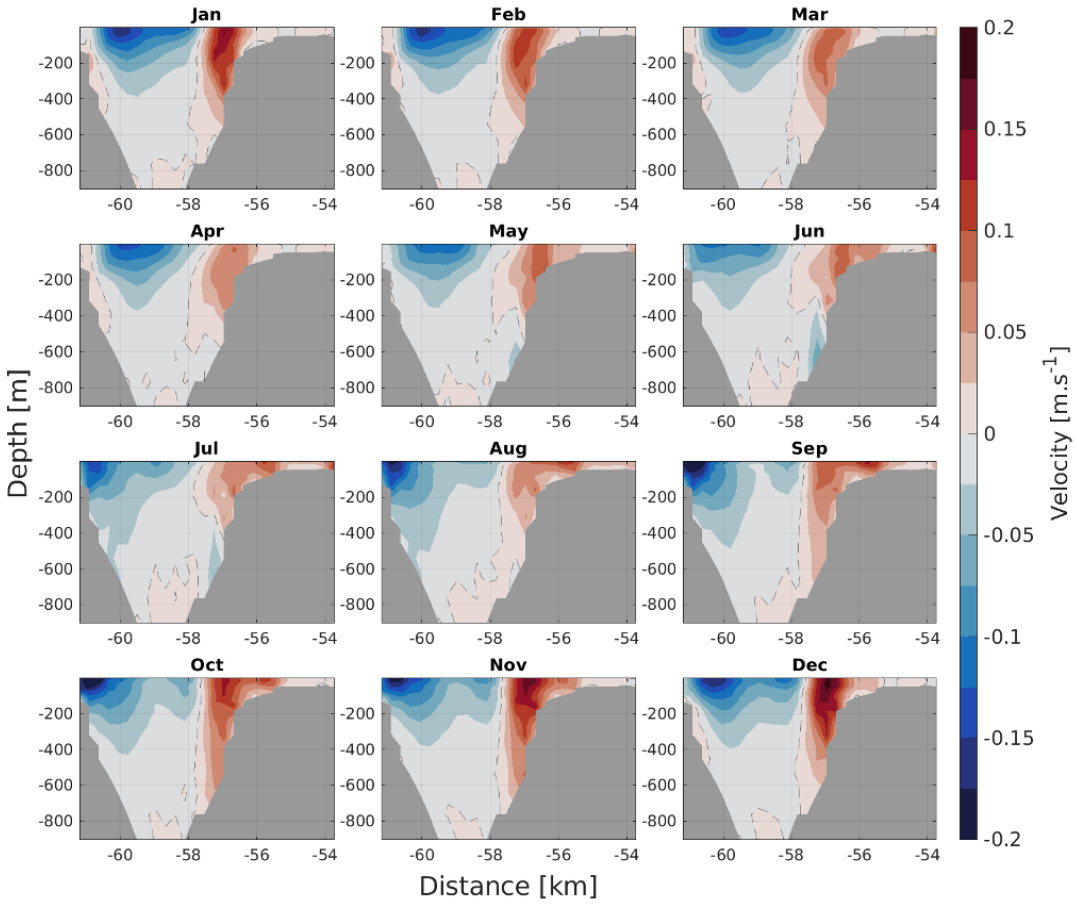

Figure 4.11: Ocean meridional velocity (in m/s) across Davis Strait in CFA. Northward direction is positive (red). Ocean depth shown in the Y-axis, and longitude in X-axis.

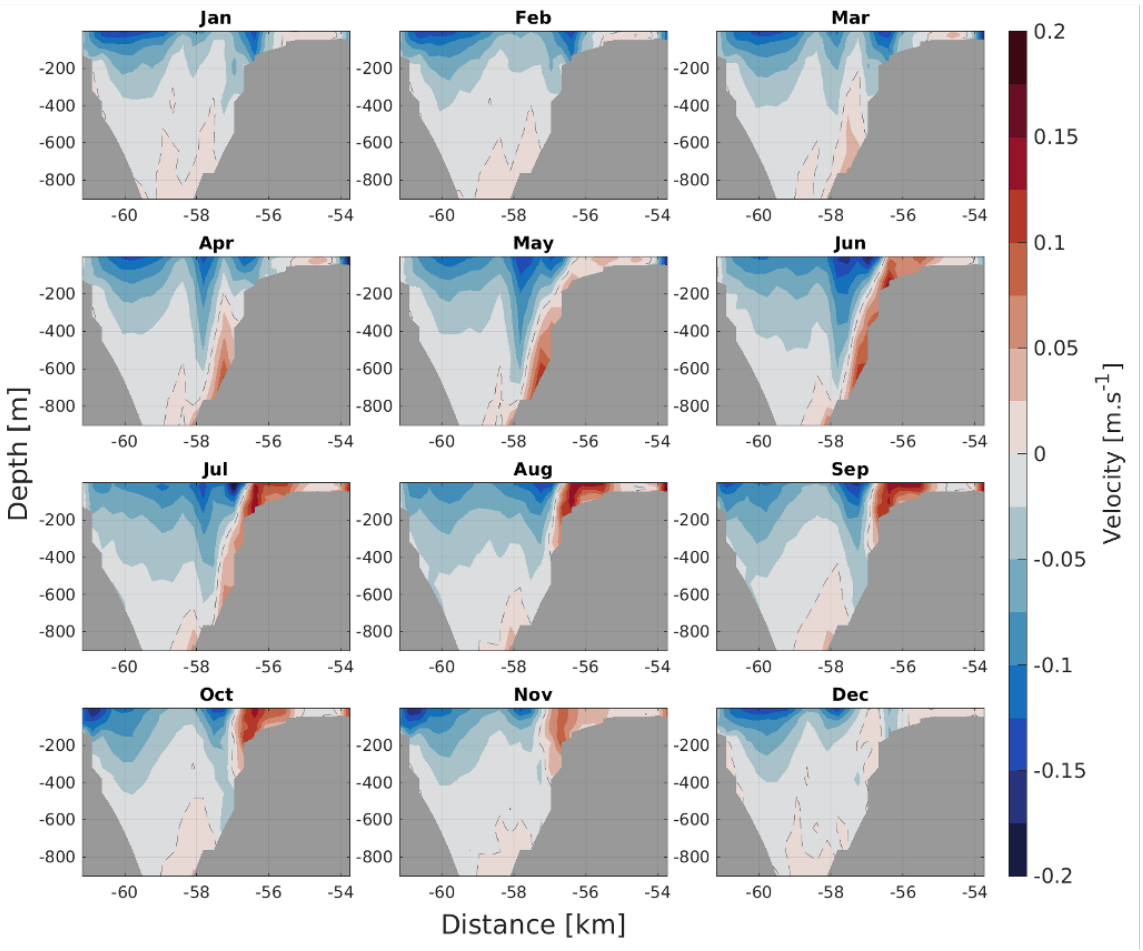

Figure 4.12: Ocean meridional velocity (in m/s) across Davis Strait in JFA. Northward direction is positive (red). Ocean depth shown in the Y-axis, and longitude in X-axis.

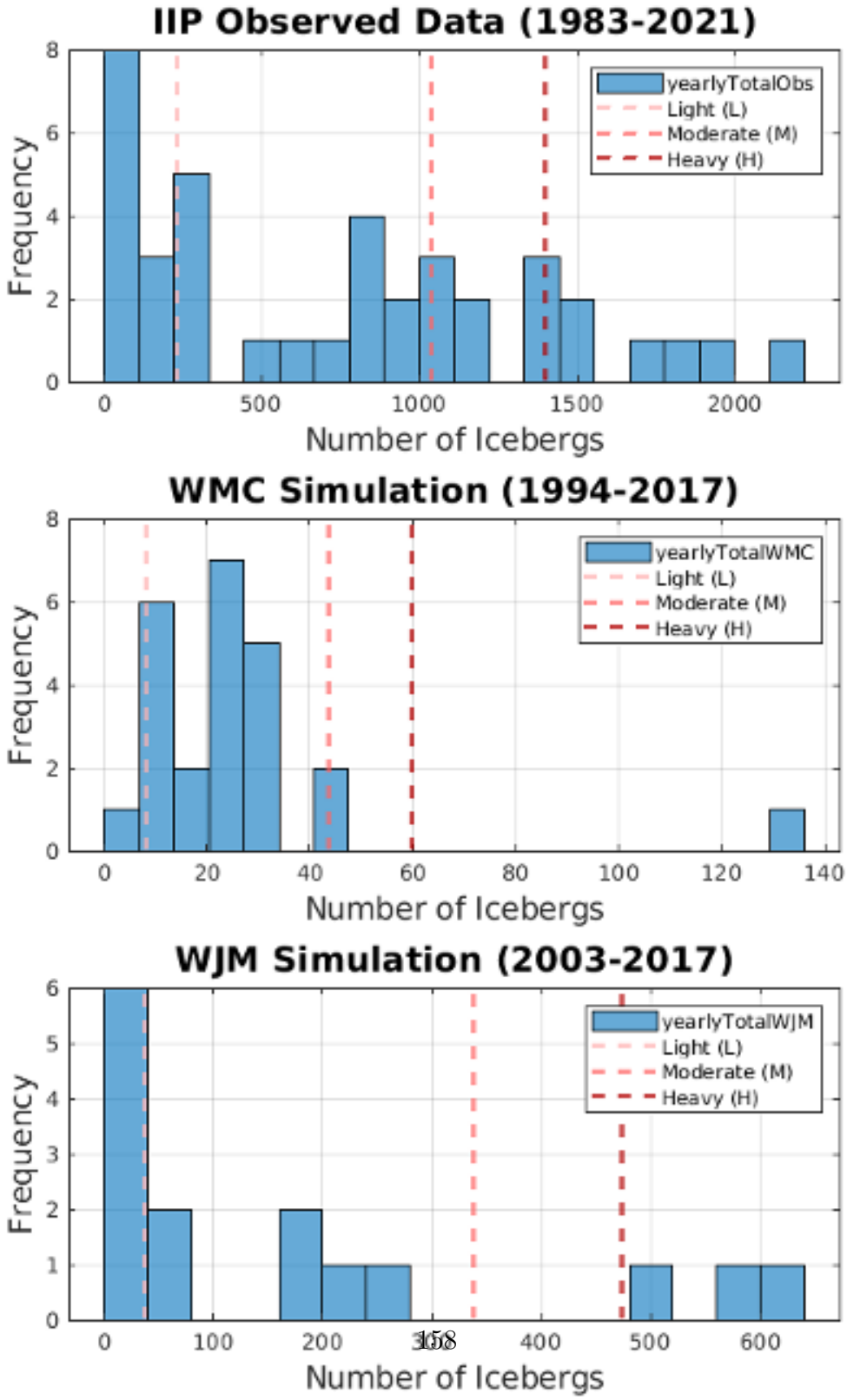

Figure 4.13: Frequency distribution of (a) I48N observed by IIP for the years 1983-2021, (b) I48N in the simulation JFA, (c) I48N in the simulation CFA.

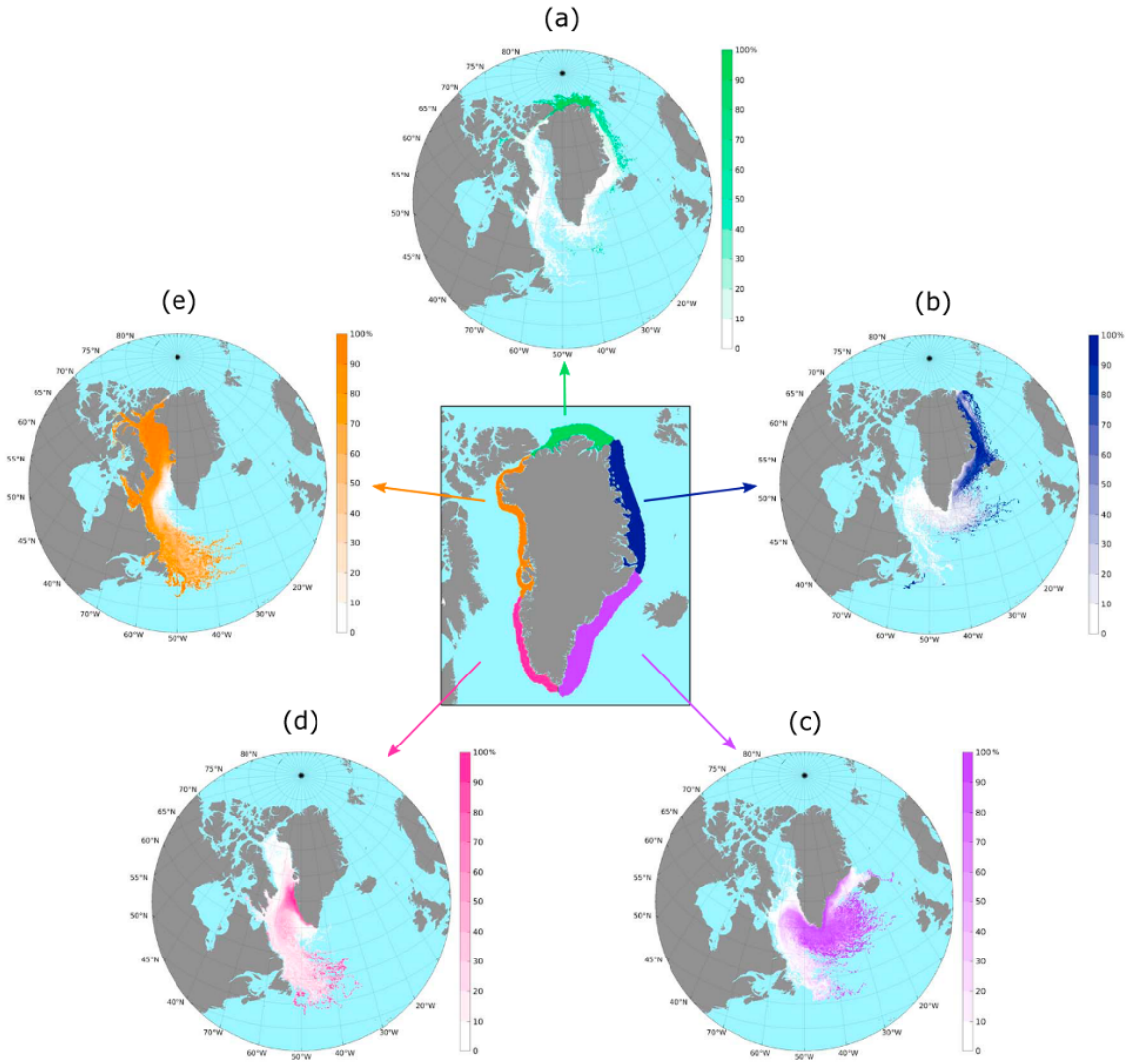

Figure 4.14: Origin of modelled icebergs in the years 2002 to 2015. The intensity of colors, at each grid point, indicates the percentage of particles that came from (a) north, (b) northeast, (c) southeast, (d) southwest, and (e) northwest. Figure source: [Marson et al., 2018]